

# A winter study case, comparing snowfall observations with the operational forecast model MEPS

Franziska Hellmuth



Thesis submitted for the degree of  
Master in Meteorology  
60 credits

Department of Geoscience  
Faculty of Mathematics and Natural Sciences

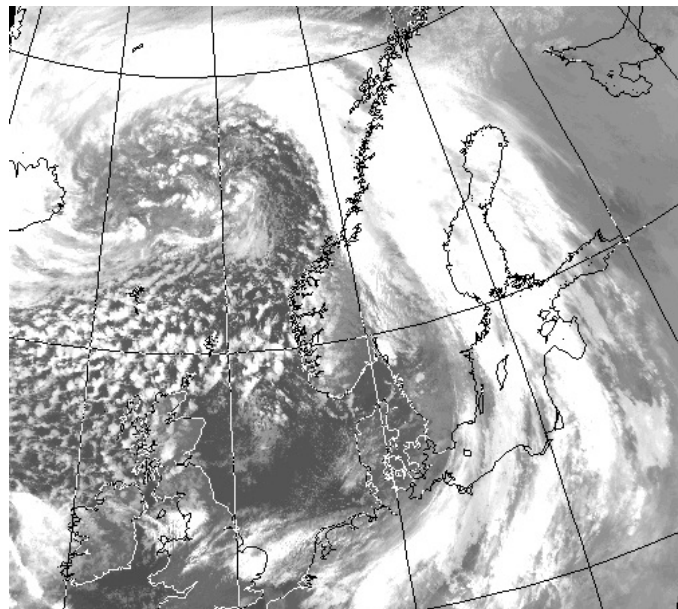
UNIVERSITY OF OSLO

Spring 2018



# **A winter study case, comparing snowfall observations with the operational forecast model MEPS**

Franziska Hellmuth



Satellite image of the extreme extratropical cyclone on 24 December 2016 at the coast of Norway. Image obtained from the Dundee Satellite Receiving Station <http://www.sat.dundee.ac.uk>.

© 2018 Franziska Hellmuth

A winter study case, comparing snowfall observations with the operational forecast model  
MEPS

<http://www.duo.uio.no/>

Printed: Reprocentralen, University of Oslo

## ABSTRACT

This abstract needs to be updated.



# TABLE OF CONTENTS

<b>LIST OF ABBREVIATIONS</b>	<b>III</b>
<b>CHAPTER 1: INTRODUCTION</b>	<b>1</b>
1.1 Background . . . . .	4
<b>CHAPTER 2: SITE, INSTRUMENTATION, DATA, AND METHODOLOGY</b>	<b>8</b>
2.1 Haukeliseter site . . . . .	8
2.2 Climate at Haukeliseter . . . . .	10
2.3 Instruments . . . . .	11
2.3.1 Double Fence Snow gauge . . . . .	13
2.3.2 MRR - Micro Rain Radar . . . . .	14
2.3.3 PIP - Precipitation Imaging Package . . . . .	17
2.3.4 MASC - Multi-Angular Snowfall Camera . . . . .	18
2.4 Optimal Estimation Retrieval Algorithm . . . . .	18
2.4.1 Snowfall retrieval scheme . . . . .	18
2.4.2 Environmental masks for the optimal estimation retrieval . . . . .	22
2.5 MetCoOp Ensemble Prediction System . . . . .	24
2.5.1 AROME - MetCoOP . . . . .	24
2.5.2 Meso-NH and the ICE3 scheme . . . . .	25
2.5.3 Adjustment of ICE3 inside MEPS . . . . .	28
2.6 Numerical data transformation . . . . .	29
2.6.1 Layer thickness in MEPS . . . . .	29
2.6.2 Snow water content . . . . .	30
2.6.3 Snow water path . . . . .	31
2.6.4 Ensemble mean and Coefficient of Variation . . . . .	31
2.6.5 Mean error and mean absolute error . . . . .	31
2.6.6 Percent difference and average difference . . . . .	32

<b>CHAPTER 3: ANALYSIS OF THE CHRISTMAS STORM 2016</b>	<b>33</b>
3.1 Extreme weather . . . . .	34
3.2 Dynamic Tropopause map . . . . .	34
3.3 Thickness, Sea Level Pressure, Total Precipitable Water, and wind at 250 hPa	37
3.4 Integrated Vapour Transport . . . . .	37
3.5 Observations at the weather mast . . . . .	40
3.6 Large scale circulation . . . . .	40
<b>CHAPTER 4: RESULTS AND DISCUSSION</b>	<b>50</b>
4.1 Sensitivity of the optimal estimation retrieval . . . . .	51
4.2 Comparison of surface observations . . . . .	53
4.3 Observation and predictions of large scale weather phenomena at the surface	57
4.4 Surface snowfall accumulation . . . . .	68
4.5 Observation of large scale weather phenomena in the vertical . . . . .	76
4.6 Orographic influence on precipitation . . . . .	87
4.7 Discussion all . . . . .	89
<b>CHAPTER 5: SUMMARY AND CONCLUSION</b>	<b>94</b>
<b>REFERENCES</b>	<b>95</b>
<b>APPENDIX A: FORWARD MODEL</b>	<b>106</b>
A.1 Scattering Model . . . . .	106
<b>APPENDIX B: RESULTS</b>	<b>109</b>
B.1 48 h surface observations and MEPS forecasts . . . . .	109
B.2 Mean error and mean absolute error . . . . .	111
B.3 Hourly averages ensemble member zero and one . . . . .	113
B.4 Vertical SWC - all ensemble member . . . . .	115

## LIST OF ABBREVIATIONS

<b>ACC</b>	Accretion
<b>AGG</b>	Aggregation
<b>AR</b>	Atmospheric River
<b>AROME</b>	Applications of Research to Operations at Mesoscale
<b>AUT</b>	Autoconversion
<b>BER</b>	Bergeron-Findeisen process
<b>C3VP</b>	Canadian CloudSat-CALIPSO Validation Project
<b>CFR</b>	Contact Freezing of Raindrops
<b>CPR</b>	Cloud Profiling Radar
<b>CV</b>	Coefficient of Variation
<b>CVM</b>	Conversion-melting
<b>DDA</b>	Discrete Dipole Approximation
<b>DEP</b>	Deposition
<b>DRY</b>	Dry processes
<b>DT</b>	Dynamic Tropopause
<b>ECMWF</b>	European Centre for Medium-Range Weather Forecasts

<b>EPS</b>	Ensemble Prediction System
<b>FMI</b>	Finnish Meteorological Institute
<b>HEN</b>	Heterogeneous Nucleation
<b>HON</b>	Homogeneous Nucleation
<b>IVT</b>	Integrated Vapour Transport
<b>LWC</b>	Liquid Water Content
<b>MASC</b>	Multi-Angular Snowfall Camera
<b>MEPS</b>	MetCoOp Ensemble Prediction System
<b>Meso-NH</b>	Mesoscale Non-Hydrostatic model
<b>Met-Norway</b>	Norwegian Meteorological Institute
<b>MetCoOp</b>	Meteorological Co-operation on Operational NWP
<b>MLT</b>	Melting
<b>MRR</b>	Micro Rain Radar
<b>MSLP</b>	Mean Sea Level Pressure
<b>NSF</b>	National Science Foundation
<b>NWP</b>	Numerical Weather Prediction
<b>PIP</b>	Precipitation Imaging Package
<b>PSD</b>	Particle Size distribution
<b>RIM</b>	Riming
<b>SMHI</b>	Swedish Meteorological and Hydrological Institute
<b>SWC</b>	Snow Water Content

<b>SWP</b>	Snow Water Path
<b>WCB</b>	Warm Conveyor Belt
<b>WET</b>	Wet processes
<b>WMO</b>	World Meteorological Organization



# CHAPTER 1: INTRODUCTION

An increased frequency of extreme weather events and heat waves, droughts, heavy rains or extremely high winds is one predicted consequence of global warming [[Hansen et al., 2014](#)]. Weather and climate extremes can have serious effects on human society and infrastructure, as well as on ecosystems and wildlife. Severe weather events are mostly in the focus of media reports on the topic of climate warming [[Meehl et al., 2000](#)]. Understanding and predicting the impact of extreme weather events is one of the major challenges of current climate research [[Field et al., 2014](#), [Stocker et al., 2013](#)].

This work focuses on the extreme event during Christmas 2016, and the snowfall measurements and model forecasts taken at the measurement site Haukeliseter in Southern Norway. The extreme storm was named 'Urd' by the Norwegian Meteorological Institute (Met-Norway), and had a large impact on Norway. Storms of this kind are expected to occur on average every five years. The financial costs associated with 2016 Christmas storm are estimated to about 180 million Norwegian kroner. 'Urd' led to major traffic problems for cars, trains, ferries and air planes. Most mountain crossings were kept closed during Christmas 2016 [[Olsen and Granerød, 2017](#)]. A change in temperature and therefore a change of frozen to liquid precipitation followed an increase in avalanche danger. In addition, 40 emergency power stations failed during the extreme event affecting around 70.000 households (Figure 1.0.1). Since people are affected by extreme weather it is important to accurately measure and forecast severe storms. The use of accurate observations will lead to better performing weather forecast models, which rely heavily on observations [[Joos and Wernli, 2012](#)].

Since winter 2010, Haukeliseter has been a WMO measuring station with single and double fence precipitation instruments. In the winter of 2016/2017, three additional state of the art radar and snowflake microphysical instruments were deployed, which could be used

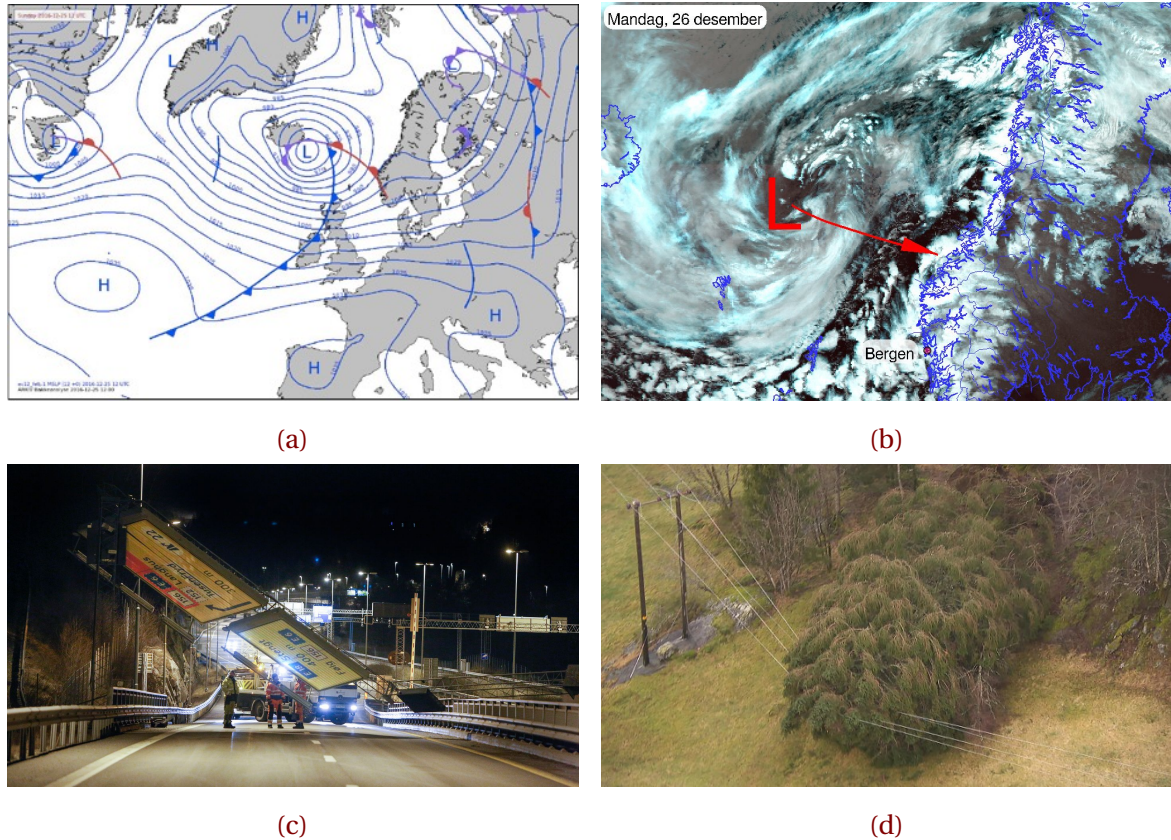


**Figure 1.0.1:** Weather situation during the extreme Christmas storm and impact on the infrastructure. In **a**: Weather situation Sunday 25 December 2016 at 12 UTC from the extreme weather report on Urd [Olsen and Granerød, 2017]. **b**: Tweet from Meteorologene [2016] on 26 December 2016 at 9:34 am: Here comes #Urd! The low pressure centre will hit Møre og Romsdal, but the strongest wind comes south of Stad. #SørNorge. **c** and **d** show the consequences related to the high wind speeds during Christmas 2016. **c**: This traffic sign, ten meter long and four meter high was blown down during the storm, [Ruud et al., 2016]. **d**: Trouble maker: The extreme weather during Christmas created problems for the local infrastructure. 80.000 households were without electricity during the storm, [Farestveit, 2016].

to estimate the vertical profile of snow water content in the atmosphere. Joos and Wernli [2012] showed on a sensitivity study of the microphysical scheme in a regional model for storm development, whether or not the placement of the precipitation is correct in the simulated storm. Looking at the vertical precipitation, which determines the vertical profile of latent heating, and hence leading to potential vorticity generation or destruction

which then in turn will lead to a storm amplification or decrease, respectively. Vertical pointing radar reflectivities are rare but can be an improvement to understand the microphysical structure in storms. Therefore, radar reflectivities were measured using the 24 GHz Micro Rain Radar (MRR) at Haukeliseter. Snowflake characteristics were estimated using a Multi-Angle Snowflake Camera [MASC; [Garrett et al., 2012](#)] and a Precipitation Imaging Package [PIP; [Newman et al., 2009](#)]. An optimal-estimation retrieval algorithm was developed that could estimate snowfall rates consistent with each MRR, MASC, and PIP measurement. This method of estimating snowfall is much like the study from [Cooper et al. \[2017\]](#). The main difference between the studies at Barrow, Alaska and this study is that a 24 GHz MRR is used instead of a 94 GHz Ka-band ARM zenith radar. The double fence measurements will provide a boundary condition to ensure that retrieved surface snowfall accumulations are close to the truth. Such agreement will in turn provide confidence that retrieved snow water contents in the vertical are also valid.

The Meteorological Cooperation on Operational Numerical Weather Prediction (MetCoOp) Ensemble Prediction forecast (MEPS) has been operational at Met-Norway, since 2016. The ensemble prediction system uses the previous deterministic AROME-MetCoOp, a version of the Météo-France Applications of Research to Operations at Mesoscale. In addition to the deterministic forecast, nine perturbed ensemble members are initialised in MEPS. The newly developed ensemble prediction systems (EPS) from Met-Norway is used to analyse the extreme winter storm during Christmas 2016. It will be shown in the thesis if the ensemble prediction system is able to forecast the variation of an extreme winter event such as 'Urd' and if the forecast model is able to predict large scale as well as local frozen precipitation. Furthermore, the use of an ensemble prediction system will give the possibility to compare the variation of snowfall precipitation at the surface and in the vertical. Observations will help to compare MEPS model forecast to examine the following research questions: How well will the model predict the surface snowfall at the measurement site? Will large scale phenomena be predicted by MEPS? Does the regional model cover local affects associated with the topography around the site?

The thesis is structured as following: The next section provides the background for the motivation of this thesis. Chapter 2 will give an overview of the measurement site Haukeliseter and its instrumentation, followed by the methodology on the optimal estimation retrieval as well as a description of the regional model MEPS. To compare the forecast system to the

observations the data had to be manipulated, this is presented in Section 2.6. The 2016 extreme Christmas event is analysed in Chapter 3. Chapter 4 will show the results and the discussion on large scale effects, surface snowfall accumulation and local wind influence at Haukeliseter. The final chapter summarises the results and findings and suggests future research questions.

## 1.1 BACKGROUND

It has long been known that measuring precipitation, especially in the form of snow, is difficult. Winter precipitation measurement show biases of more than 100 % between different gauge observation networks and different regions [Kochendorfer et al., 2017]. The local climate changes from station to station leading to different habit and size of frozen aggregates. Measurement uncertainties can be caused by the instrument itself, which varies with wind speed, gauge wind shielding, shape, size, phase, and fall velocity in hydrometeors [Kochendorfer et al., 2017, Wolff et al., 2015]. Uncertainties in precipitation measurements under windy conditions can affect water balance calculation and the calibration of remote sensing algorithms [Wolff et al., 2015].

Precipitation observations are important for hydrological, climate and weather research, as more than one-sixth of the world's population receives water from glaciers and seasonal snow packs [Barnett et al., 2005].

Since winds have an influence on frozen precipitation, a WMO (World Meteorological Organization) precipitation analysis between 1987 and 1993 recommended, that the double-fence inter-comparison reference should be used as a reference for snow measurements [Goodison et al., 1998]. An adjustment for unshielded and single-shielded precipitation gauges followed in 2010. The adjustment transfer function, for single fence gauges, represents a capture efficiency as a function of air temperature and wind speed to delimit the error of measured snowfall [Kochendorfer et al., 2017, Wolff et al., 2015].

The quantitative estimation of snowfall at the global scale from spaceborne measurements has occurred only recently. Initial retrieval approaches were based on passive microwave measurements [Noh et al., 2006, Skofronick-Jackson et al., 2004]. But since these passive measurements can only assess total integrated snow water path for a given column, such efforts were unable to provide much information on the vertical profiles of snow

water. The launch of the CloudSat 94 GHz Cloud Profiling Radar (CPR) in 2006, however, provided the first opportunity to examine such vertical structure at a global scale. Several studies, such as Matrosov [2007] and Kulie and Bennartz [2009], have shown that the CPR can be used to estimate snowfall rate but that estimated snowfall values depend heavily upon assumed snowflake microphysical properties. So, for a given radar reflectivity, we can get large differences in estimated snow rate depending upon retrieval assumptions such as snowflake habit and particle size distribution (PSD). For the operational CloudSat snowfall retrieval scheme (2C-SNOW-PROFILE), Wood et al. [2015] developed snowflake particle models based upon video snow disdrometer observations from the Canadian CloudSat-CALIPSO Validation Project [C3VP, Hudak et al., 2006]. Scattering properties for these snow particle models were based upon the Discrete Dipole Approximation (DDA) method. It was hoped that the use of realistic snow properties in the retrievals would lead to reasonable estimates of snowfall in the retrieval. In addition, they derived an a priori relationship between particle size distribution parameters and temperature that they could use as an additional constraint for the snowfall scheme. Use of the flexible optimal-estimation retrieval framework allowed a means to develop a best estimate of snow properties that are consistent with both the CPR reflectivities and the a priori constraint.

They have also been used to estimate snowfall in remote locations such as the Antarctic and Arctic [Kulie et al., 2016, Palerme et al., 2014], that in turn, have been used to evaluate the representation of snowfall in climate models [Christensen et al., 2016, Palerme et al., 2017]. Similarly, these estimates have been used to assess the performance of ground-based radar schemes such as those based upon the operational weather radar system in Sweden [Norin et al., 2015]. Despite such progress, however, the CloudSat scheme can still lead to uncertainties in the retrievals of up to 140 % to 200 % [Wood, 2011] for individual storms.

Again, these uncertainties arise from the large variance in snowflake microphysical properties as observed in nature. In response, Cooper et al. [2017] explored the use of in-situ, event specific observations of snowflake microphysical properties to improve radar-based retrievals of snowfall. This work was based upon observations from the Ka-band ARM Zenith Radar (KAZR) and Multi-Angle Snow Camera (MASC) deployed at the ARM Climate Facility Site at Barrow in Spring 2014. This ground-based 35 GHz retrieval scheme was modified from the space-borne 94 GHz CloudSat retrieval scheme developed by Wood

[2011]. But instead of using a temperature dependent a priori characterisation of PSD, Cooper et al. introduced the in-situ observations of particle size distribution through the a priori terms of the optimal-estimation framework.

Preliminary analyses suggest good performance for this retrieval scheme at Barrow. Estimates of snowfall from the Cooper et al. [2017] approach differed by 18 % relative to nearby National Weather Service snow gauge measurements for total accumulation over multiple snow events. However, given limited snowfall observed at Barrow during the MASC deployment, it was difficult to come to any definitive conclusions about retrieval performance. The NSF (National Science Foundation) funded field campaign with MRR, MASC, and PIP (Precipitation Imaging Package) deployment at Haukeliseter provides an ideal opportunity to further explore this retrieval approach. This study will continue to examine the sensitivity of retrieval surface snowfall rate to assumptions of habit, fall speed, and particle size distribution as in Cooper et al. [2017]. But the work presented here will be different in that we also will examine the vertical profiles of snowfall through the atmospheric column.

With the increasing expansion of computational power, developments of high-resolution numerical weather forecasting models with  $\leq 4$  km scales can be able to represent small-scale phenomena, such as convective dynamics [Gowan et al., 2018]. This enhancement provides weather services the ability to improve short-term weather forecasts for convective events, which can seriously impact infrastructure and society [Müller et al., 2017]. Information on magnitudes and location of maximum temperature is of significant importance when warnings are published by meteorological services for severe weather events and for further use in downstream impact model, e.g. NVE's (Norwegian Water Resources and Energy Directorate) hydrological model for flooding and avalanche risk. The ability to use high-resolution models is also followed by various challenges, such as physical parametrisation schemes, accurate representation of topography, and data assimilation of high-resolution data [Sun, 2005].

The weather forecast in Scandinavia covers a wide range of phenomena and includes continental, maritime and polar conditions. Norway has a complicate coastline, gradients in land use, as well as complex topography, which can complicate local weather forecasting of temperature, wind and precipitation [Müller et al., 2017]. Colle et al. [2005], Garvert et al. [2005], Schwartz [2014], for example, have shown, that simulations of orographic

precipitation can be improved in mountainous terrain for horizontal grid spacing below 4 km. Uncertainties on a convective scale can lead to a rapid error growth [[Lorenz, 1969](#)], hence high-resolution ensemble prediction makes it possible to estimate the forecast uncertainty by performing several model runs, each with different initial conditions.

The Christmas storm in 2016, might not have led to the same damages as some of the extreme weather events of recent years. As people and infrastructure are affected by extreme weather, it is necessary to further improve the accuracy of snow-ground observations to better verify numerical weather forecasts, hydrological and climate models [[Joos and Wernli, 2012](#)]. Changes in snow pack characteristics after extreme rain on snow events can lead to severe avalanches [[Stimberis and Rubin, 2011](#)] and to the formation of thick layers of ice in the snow pack or on ground [[Hansen et al., 2011](#), [Putkonen and Roe, 2003](#)].

# CHAPTER 2: SITE, INSTRUMENTATION, DATA, AND METHODOLOGY

This chapter describes the site, instruments, the optimal estimation retrieval and the regional forecast model used to determine the vertical profile of snow water content for observed snow events. The determination of required parameters from the measuring instruments in relation to the optimal estimation retrieval will be explained. The purpose of this study is to compare the vertical observations from the Haukeliseter measurement site and the output from the operational forecast model at the Norwegian Meteorological Institute for the extreme weather event during Christmas 2016. The last section will give an insight on how the data was analysed to compare the different systems.

## 2.1 HAUKELISETER SITE

Haukeliseter, shown in Figure 2.1.1 is a mountain plateau 991 m above sea level, located in the Norwegian county 'Telemark' (59.8° N, 7.2° E, Figure 2.1.1). The station measures precipitation, temperature, snow depth and wind. It has served as a measurement site for snow accumulation since the winter of 2010/2011 [Wolff et al., 2010, 2013, 2015] and serves as WMO (World Meteorological Organization) station.

The study site is surrounded by mountain tops being 100 m to 500 m higher than the flat area. As seen in Figure 2.1.1c is Haukeliseter more open to the south and the south-west and the closest mountain top (situated to the NE) has an altitude of 1162 masl, [Wolff et al., 2015]. The mountains west to north exceed elevations of 1600 m.

A detailed setting of the measurement site is shown in Figure 2.3.1. The precipitation sensors are perpendicular to the predominant wind. Additional measurements of other

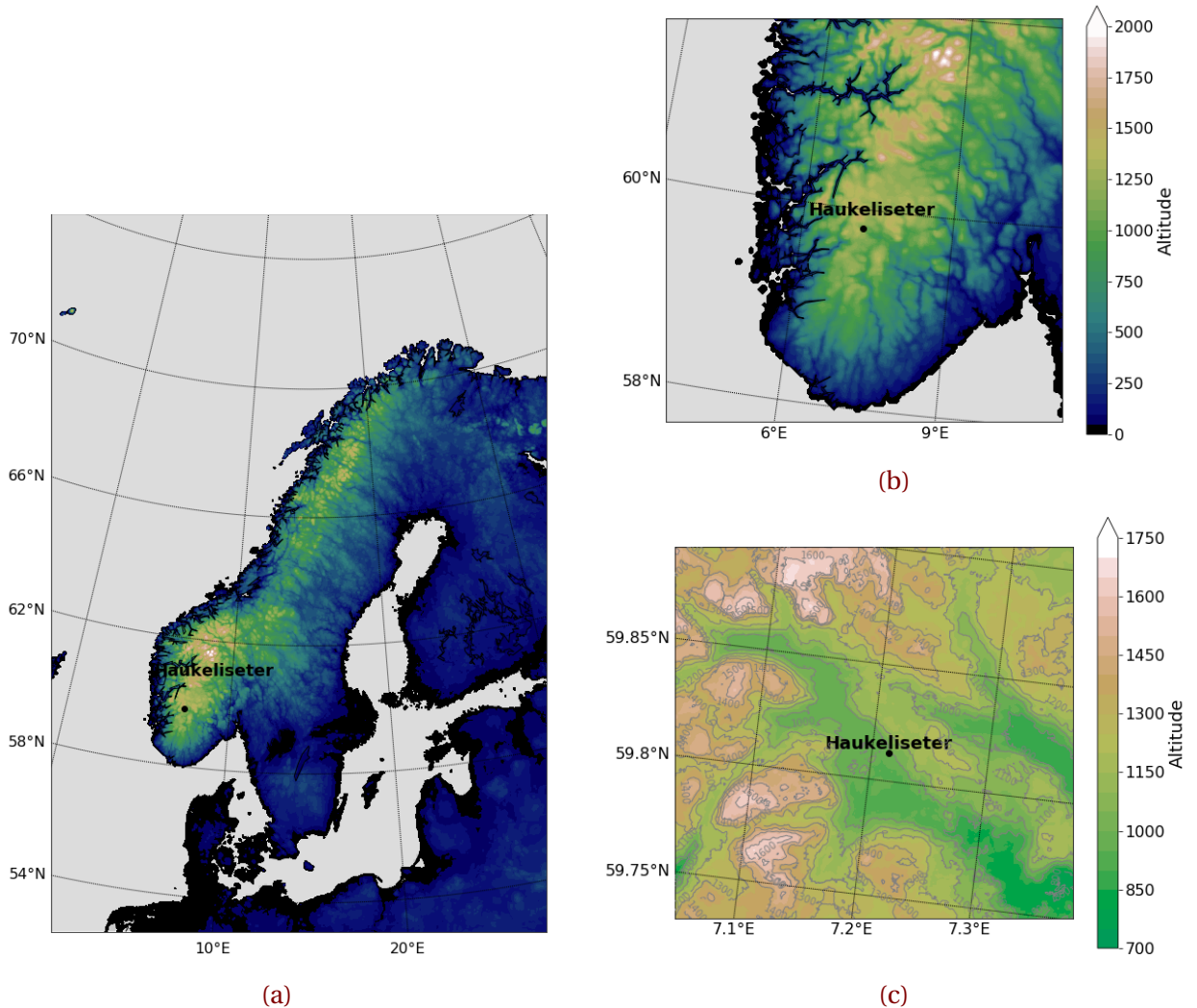


**Figure 2.1.1:** Model elevation map of Northern Europe (a) and Southern Norway (b), where the model domain of MEPS are presented in Lambert projection. The elevation corresponds to the legend of b. A topographic map of the measurement site is shown in c with DTM 10 Terrain Model (UTM33) from [Geonorge \[2018\]](#).

meteorological parameters such as temperature, wind, and pressure are used to connect the large-scale weather situation with the local measurements. The data is provided by [eklima \[2016\]](#), where the temperature is measured at double fence height. The hourly value of temperature is represented by the last minute value of the previous hour measurement. The 10 m wind is measured by an ultrasonic wind sensor from Gill, mounted at the tower

close to the double fence. Wind data is obtained from [eklima \[2016\]](#) and represents 10 min averages from the last 10 min of an hour.

## 2.2 CLIMATE AT HAUKELISETER

The general climate at Haukeliseter can be defined with the updated Köppen-Geiger climate types presented in [Peel et al. \[2007\]](#). Figure 8 in [Peel et al. \[2007\]](#) show, that Haukeliseter may lay in a transition zone and can be categorized as ET, a polar tundra climate type (hottest month temperature  $T_{hot} \geq 0^{\circ}\text{C}$ ) or as Dfc, a cold climate without dry season and cold summers. Haukeliseter presents a typical Norwegian climate condition. At the measurement site, frequent snow events combined with high wind speeds are observed during a six to seven month winter period. In addition, a snow amount of about two to three meter can be expected, where 50 % of the yearly precipitation is solid in the form of snow, graupel or mixed-phase precipitation [[Wolff et al., 2010, 2013, 2015](#)].

The mean wind direction (Figure 2.3.1) for solid precipitation is from the west/east with maximum wind speed above  $15 \text{ m s}^{-1}$ , observed during a 10-year winter period at a nearby station [[Wolff et al., 2010, 2015](#)]. In Figure 2.2.1, the green dashed line represents the average December temperature of  $-6^{\circ}\text{C}$  (30-yr period 1961 to 1990,[[eklima, 2016](#)]). December 2016 was warmer with an anomaly of +4.9 K above the climate mean. In 2016, the precipitation was 200 % more than the climate mean during December. This difference could be associated with the new installation of the double fence - Geonor gauge at Haukeliseter. In [Wolff et al. \[2015\]](#), Figure 5 shows that single fence precipitation gauges underestimate the amount of precipitation about 80 % during high wind speed events. Since the Double Fence construction was not in use before 2010/2011, which might have led to an observation of too little precipitation at Haukeliseter during winter and a followed incorrect climate statistic. The precipitation observed in the period of 21 to 27 December 2016 where 56.9 % of the total accumulated precipitation in December 2016. Furthermore, a maximum wind of  $22.3 \text{ m s}^{-1}$  was observed in this period, which can be associated with a slight storm (Section 3.5 and Table 3.5.1).

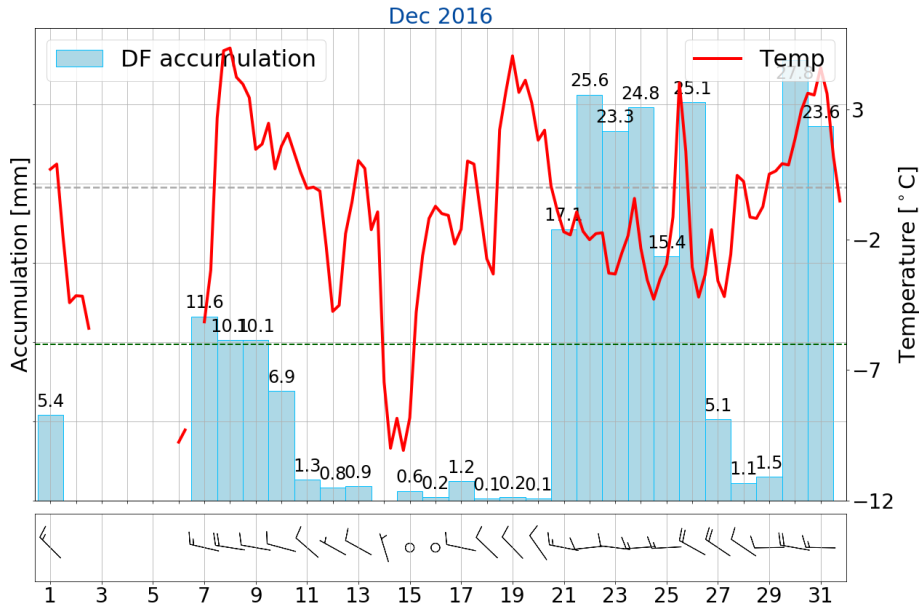


**Figure 2.2.1:** Observations at Haukeliseter weather mast during December 2016. The daily accumulation is presented in light blue [mm]; the six hour mean temperature in red, [ $^{\circ}\text{C}$ ], and daily maximum 10 m wind as barbs [ $\text{m s}^{-1}$ ]. Gray dashed line indicates the freezing temperature. The freezing temperature is indicated by the green dashed line and the monthly normal value ( $-6.0^{\circ}\text{C}$ ) by the green [eklima \[2016\]](#). Note, no data was available from 2 to 6 December 2016.

## 2.3 INSTRUMENTS

The WMO site Haukeliseter, operated by Met-Norway serve numerous meteorological measurements of temperature, wind speed and direction. 10 m wind and 4.5 m air temperature are measured at the tower close to the double fence (Section 2.3.1). The wind measurements are performed with an ultrasonic wind sensor from Gill (Wind observer II with extended heating). Air temperature is obtained with a pt100 element at gauge height and protected by standard Norwegian radiation screen [Wolff et al., 2015]. Pressure?

Further information about the WMO site and the instrument setting, can be found in Wolff et al. [2013, 2015].

A collaboration between the University of Utah, University of Wisconsin and Met-Norway made it possible to install three additional instruments at the measurement site during winter 2016/2017. A Micro Rain Radar (MRR) is used to obtain particle reflectivity and Doppler velocity aloft, thus providing the vertical structure of the storm. Additionally, a

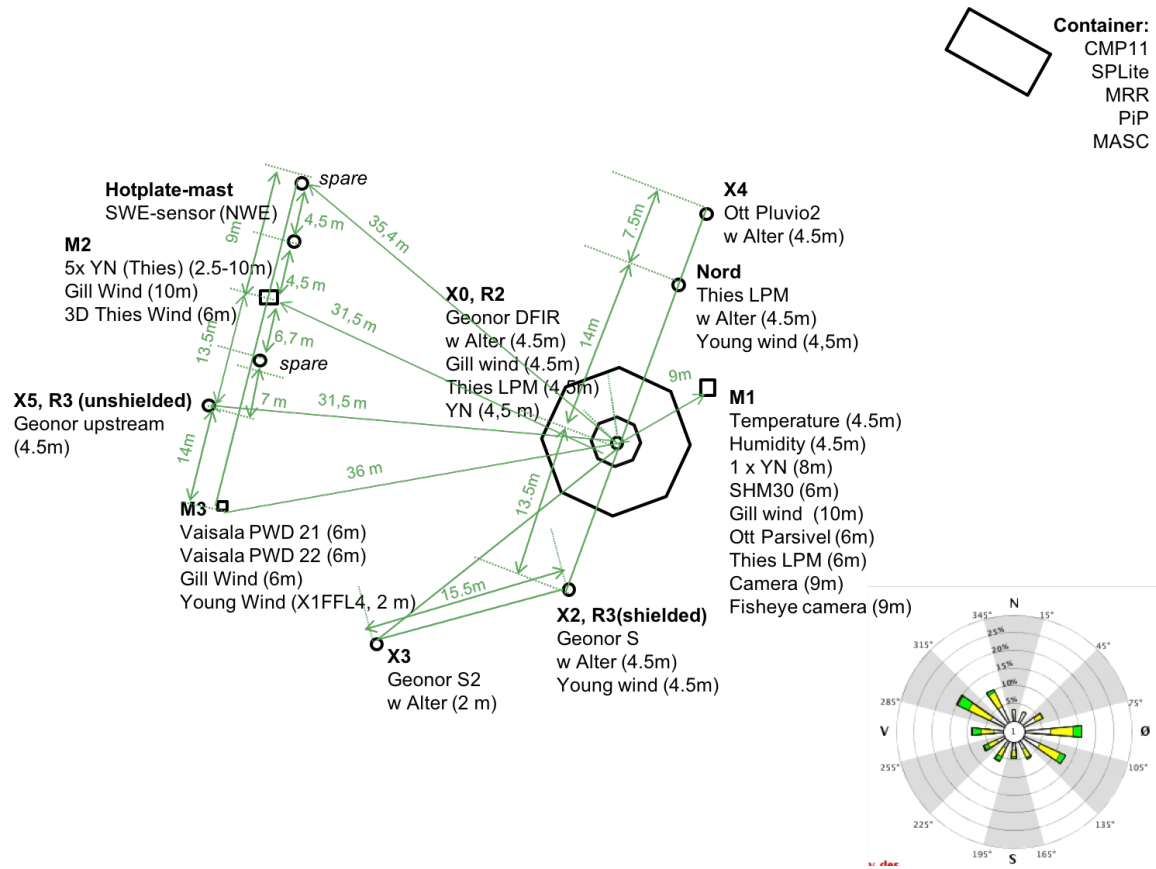


Figure 2.3.1: Instruments at the Haukeliseter measurement site during winter 2016/2017 [adapted from Wolff et al., 2015]. The windrose indicates the mean wind direction from either from west-north-west or east-south-east.

Multi-Angle Snowflake Camera (MASC) and a Precipitation Imaging Package (PIP) will be used to determine the snow habit, the snowfall particle size distribution, and the near-surface fall speed. Since many factors such as humidity and temperature contribute to snowflake geometry, the use of these instruments will provide knowledge of snowflake habits, particle size distributions, and fall speed crucial to reduce error in snowfall retrievals.

A sketch of the instrumentation setting is presented in Figure 2.3.1. The octagonal indicates the double fence. The container is north-east from the double fence having the MRR, MASC and PIP mounted at the top. **M1** in Figure 2.3.1 is the 10 m weather mast, providing

the hourly [eklima \[2016\]](#) temperature, pressure, and wind measurements. The mean wind direction from west-north west and east-south east are shown in the wind rose in Figure 2.3.1.

### 2.3.1 DOUBLE FENCE SNOW GAUGE

Since the winter 2010/2011 Haukeliseter is equipped with several precipitation gauges. The wind shielded gauges are placed perpendicular to the main wind direction (E/W wind).

The wind-induced under-catch of solid precipitation is determined by [Wolff et al. \[2015\]](#). The wind plays different roles in the amount of accumulation depending on the kind of precipitation. For temperatures below  $-2^{\circ}\text{C}$  the wind speed influences the falling snow. Where less precipitation can be observed at higher wind speeds or more precipitation can be measured if too much is blown into the gauge. The catch ratio between the standard Geonor precipitation gauge and the Double Fence - Geonor (Figure 2.3.2a) shows that only 80 % of solid precipitation is observed at wind speeds of  $2\text{ m s}^{-1}$  whereas only 40 % at  $5\text{ m s}^{-1}$ , Figure 5 in [Wolff et al. \[2015\]](#).

The precipitation gauge protected by an octagonal double fence (Figure 2.3.2a) is more accurate than the single fence and will be used as the reference to all surface accumulation measurements. The double fence creates an artificial calm wind and maximize the catch of precipitation, [\[Wolff et al., 2010, 2013, 2015\]](#). The wind inside the double fence is measured to be not much higher than  $5\text{ m s}^{-1}$  even if the winds out-

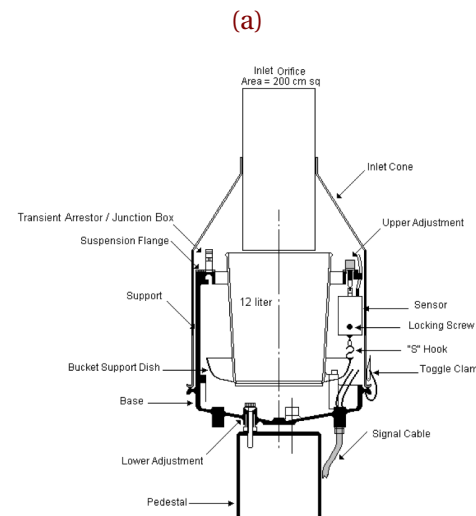


**Figure 2.3.2:** a: Double fence and unprotected precipitation gauges at Haukeliseter, from [Wolff et al. \[2015\]](#). The prevailing wind direction from east comes from the lower, left corner in the image and the west wind from the opposite site. b: Vertical cross section of T-200B precipitation gauge [[Geonor Inc., 2015](#)].

side exceed  $20 \text{ m s}^{-1}$  (occurred 26 December 2016).

This shows the need of a combination of ground-based observations together with an optimal estimation retrieval to verify the accuracy of MEPS. Wolff et al. [2015] introduced an adjustment function for the Geonor double fence, so that different precipitation under certain wind speeds are presented correctly and can be used as confidential data. For now, it is presumed that the average under catch inside a double fence is 20 % for wind speeds between  $10 \text{ m s}^{-1}$  and  $20 \text{ m s}^{-1}$  and 10 % for wind speeds below  $9 \text{ m s}^{-1}$  [Wolff, 2018].

Inside the double fence is a precipitation-weighing gauge Geonor T-200B3 [3-wire transducers, 1000 mm, Geonor Inc., 2015] with an Alter wind screen to reduce wind turbulence around the gauge. At Haukeliseter the orifice height of the Geonor is 4.5 m above the ground because of an expected snow depth of two to three meter during a winter season and the likelihood of measuring drifting snow [Wolff et al., 2013, 2015].

A vertical cross section of the T-200B gauge is shown in Figure 2.3.2b. The precipitation particles fall through the  $200 \text{ cm}^2$  orifice protected with a heated collar, into a cylindric bucket filled with frost protection. The bucket is placed on top of a Bucket Support Dish [Figure 2.3.2b, Geonor Inc., 2015]. This dish is connected with three wire sensors having an eigenfrequency changing with the weight inside the bucket. A formula provided by Geonor Inc. [2015] calculates the amount of precipitation with the frequency of each sensor. The three sensors provide a reduction of an error in connection with an unlevel installation. Met-Norway average the values of all three sensors and provide hourly data at **eklima**.

### 2.3.2 MRR - MICRO RAIN RADAR

Radar are very useful to observe the vertical profile of the atmosphere. The instrument detects mesoscale features and makes it possible to visualise the vertical structure of storms [Markowski and Richardson, 2011].

The principle of radar measurements is based on an electromagnetic wave, which is emitted from the radar transmitter and interacts with the hydrometeors along the beam. A fraction of the



Figure 2.3.3: Micro Rain Radar at the measurement site in Kiruna.

pulse energy is reflected back to the receiver of the radar. The quantity of scattering depends on the shape and structure of the reflected particle. Vertical profiles of reflectivity give information about the diameter of the target object.

The Micro Rain Radar (Figure 2.3.3) measures profiles of Doppler spectra [METEK, 2010]. The Doppler spectrum describes the movement of the particle. The vertical pointing Doppler radar measures the returning energy from each interval and enables the detection of the Doppler spectrum [L'Ecuyer, 2017]. The MRR has a frequency of 24 GHz and a temporal and spatial resolution of 60 s and 100 m, respectively. The radar height range from 100 m (because of ground clutter) to 3.000 m [METEK, 2010].

MRR radar reflectivity ( $Z$ ) is transformed from  $1 \text{ mm}^6/\text{m}^3$  to dBZ, by the following relationship;

$$Ze = 10 \log_{10} \left( \frac{Z}{1 \text{ mm}^6/\text{m}^3} \right) \quad [\text{dBZ}] \quad (2.3.1)$$

A transformation to rainfall rates can be performed by the  $Z$ - $R$  (reflectivity - rainfall) relationship. The rainfall rate in each layer can be estimated by the use of typical fall speeds and the Marshall-Palmer particle size distribution for liquid particles [Rinehart, 2010], Equation (2.3.2)

$$Z = 200R^{\frac{8}{5}} \quad [\text{mm}^6\text{m}^{-3}]$$

$$R = \left( \frac{10^{\frac{Ze}{10}}}{200} \right)^{\frac{5}{8}} \quad [\text{mmh}^{-1}] \quad (2.3.2)$$

The Z-R relationship with the Marshall-Palmer assumption (Equation (2.3.2)) applied is represented in Table 2.3.1. Z-snowfall relationships are developed but are difficult to apply due to the variation of size and density of the particles [L'Ecuyer, 2017].

After the transformation to dBZ the reflectivity is averaged for every 200 m thick layers, where only values above 300 m taken into account, e.g. a reflectivity at 400 m represents the mean value of reflectivity between 300 m and 500 m.

**Table 2.3.1:** Typical reflectivity values, according to Doviak and Zrnic [1993], obtained from measurements, models, and observations. The rainfall rate  $R$  is calculated with Equation (2.3.2).

	<b>Ze</b> [dBZ]	<b>R</b> [mm h <sup>-1</sup> ]
<b>Drizzle</b>	<25	1.3
<b>Rain</b>	25 to 60	1.3 to 205.0
<b>Snow</b>		
dry, low density	<35	5.6
Crystal; dry, high density	<25	1.3
wet, melting	<45	23.7
<b>Graupel</b>		
dry	40 to 50	11.5 to 48.6
wet	40 to 55	11.5 to 99.9
<b>Hail</b>		
small; <2 cm, wet	50 to 60	48.6 to 205.0
large; >2 cm, wet	55 to 70	99.9 to 864.7
<b>Rain &amp; Hail</b>	50 to 70	48.6 to 864.7

### 2.3.3 PIP - PRECIPITATION IMAGING PACKAGE

The Precipitation Imaging Package (PIP) is a video disdrometer that is a modification of the Snowflake Video Imager presented by [Newman et al. \[2009\]](#). It consists of a halogen flood lamp and a video system that samples at 60 Hz (Figure 2.3.4). Both lamp and lens have a distance of approximately 3 m that follows a field of view: 32 mm by 24 mm.

In front of the halogen lamp there is a frosted window, so that the background light is uniform over all time. A falling particle appears as a 2-D shadow in the video image. Particle size distribution (PSD) and fall speed of precipitation can be determined from the black and white images provided by the system. The instrument also can give first order estimates of snowflake particle habit when in focus in the images. [Newman et al. \[2009\]](#) describes the details of the algorithm applied to the system to get information about the snow-particle habit. The winds have almost no effect on the result of the video distrometer [[Newman et al., 2009](#)]. To reduce eventual wind effects, the distrometer was oriented perpendicular to the mean wind.



Figure 2.3.4: Precipitation Imaging Package.

### 2.3.4 MASC - MULTI-ANGULAR SNOWFALL CAMERA

The Multi-Angular Snowfall Camera (MASC) takes high-resolution images of hydrometeors in free fall and measures the fall-speed simultaneously.

The MASC consists of three cameras, three flashes, and two near-infrared sensors, pointing at a ring centre (Figure 2.3.5). A hydrometeor has to pass through the ring in a certain way to trigger the near-infrared sensors. At the same time the three cameras take a picture of the falling particle. Since the cameras take pictures from three different angles, the particles size, shape, and orientation can be specified from an algorithm applied to the image, described in [Garrett et al. \[2012\]](#). Furthermore, the form and heritage of the hydrometeor, such as collision-coalescence, riming, capture nucleation, or aggregation, can be estimated.

The near-infrared sensor, that is used to trigger the cameras and the lights quantifies the fall-speed of the hydrometeors, by measuring the time the particle needs to pass the distance between the upper and lower trigger.

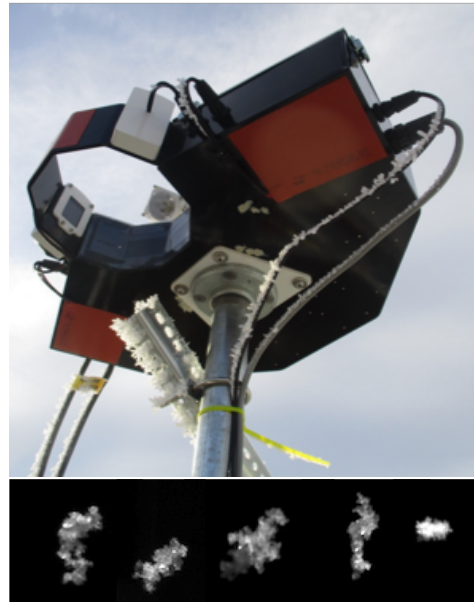


**Figure 2.3.5:** MASC and images taken by instrument during the Christmas storm 2016.

## 2.4 OPTIMAL ESTIMATION RETRIEVAL ALGORITHM

The purpose of this study is to apply an optimal-estimation snowfall retrieval on ground based measurements to estimate the surface accumulation and vertical snow water content for an extreme event during Christmas 2016. These will later be used to compare to 48 h MEPS model forecasts to see if the model was able to predict synoptical features and precipitation related to the extreme event 'Urd' in 2016.

### 2.4.1 SNOWFALL RETRIEVAL SCHEME

The optimal-estimation snowfall retrieval scheme was modified for the Barrow instrumentation described in [Cooper et al. \[2017\]](#) to the 24 GHz MRR, MASC, and PIP located at Haukeliseter. This scheme was then used to derive surface snowfall rates and vertical profiles of snow water content using different combinations of retrieval assumptions based upon in-situ observations. Here a discussion of the optimal-estimation framework is presented so that the reader can understand exactly how the different measurements in the retrieval scheme were incorporated. The differences in the forward and inverse problem are reviewed in the beginning. Both, forward and inverse problem underlie the basic methodologies of remote sensing.

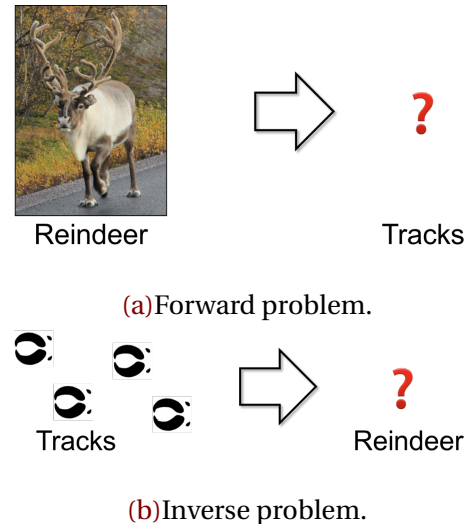


**Figure 2.4.1:** **a:** Relationship between parameter of interest (reindeer) and the unknown parameter of measurements (tracks). **b:** Inverse problem when the parameter of measurements is known but the parameter of interest is not [[Stephens, 1994](#)].

The general concepts of forward and inverse problems are illustrated in Figure 2.4.1. The forward problem describes the relationship between the physical parameters of interest and the measurements (Figure 2.4.1a). In Figure 2.4.1b, the physical parameter is the reindeer and the measurements are its tracks. In the here presented thesis snowfall scheme, the physical parameters are the vertical profiles of snow water content (SWC) and the measurements are the MRR reflectivities. The inverse problem represents the opposite goal. The physical entity (reindeer and SWC) must be inferred from the measurements (reindeer tracks or MRR reflectivities).

The optimal-estimation framework is used to solve the inverse problem for the thesis work. But it is more complex than the direct inversion as represented in Figure 2.4.1b. Instead of inverting directly for the parameter of interest (SWC) from the measurements [dBze], the scheme includes additional information based upon an 'a priori' understanding of the physics of the retrieval problem. Thus, it represents a weighted balance between what

the data can tell about the state and what is already known about it. For the CloudSat retrieval scheme, this a priori information came from a parametrisation relating particle size distribution (PSD) to temperature. For the Barrow and Haukeliseter schemes, the a priori information could also come from the in-situ observations of snowflake microphysics. These constraints also add numerical stability to the inversion process when there are either calibration errors in the measurements or uncertainties in the forward model that relates the physical parameter to measurement space. Details of the radar forward model are discussed at the end of this section.

The optimal estimation method is based on Gaussian statistics. It solves for snowfall properties of interest or retrieval vector,  $\mathbf{x}$ , by minimizing the scalar cost function,  $\Phi$ , as in Equation (2.4.1).

$$\begin{aligned}\Phi(\mathbf{x}, \mathbf{y}, \mathbf{a}) = & (\mathbf{y} - F(\mathbf{x}))^T \mathbf{S}_y^{-1} (\mathbf{y} - F(\mathbf{x})) \\ & + (\mathbf{x} - \mathbf{a})^T \mathbf{S}_a^{-1} (\mathbf{x} - \mathbf{a})\end{aligned}\quad (2.4.1)$$

Specifically, or this thesis retrieval scheme,  $\mathbf{x}$  represents the PSD parameters of slope and number intercept of an assumed exponential size distribution for each radar range bin as in Equation (2.4.2).  $\mathbf{y}$  is the vector of MRR reflectivities. The vector  $\mathbf{a}$  is the a priori guess for slope parameter and number in each range bin.  $F(\mathbf{x})$  represents the forward model that translates snow properties into reflectivity space. Minimizing the cost function therefore seeks to reduce the difference between the observations,  $\mathbf{y}$ , and simulated observations,  $F(\mathbf{x})$  and between the a priori guess ( $\mathbf{a}$ ) and the retrieval vector ( $\mathbf{x}$ ).

$$n(r) = N_0 \exp(-\lambda r) \quad [\text{m}^{-3} \text{ mm}^{-1}] \quad (2.4.2)$$

The  $\mathbf{S}_y$  and  $\mathbf{S}_a$  terms, in Equation (2.4.1), represent the forward model and measurement error covariance matrix and the a priori error covariance matrix, respectively. The relative differences between  $\mathbf{S}_a$  and  $\mathbf{S}_y$  weight the importance of the observations and the a priori considerations in determining our best estimate of PSD properties.

Newtonian iteration is used until the value of the cost function converges and our best estimate of snowfall properties are found. The optimal-estimation scheme also provides error diagnostics through the retrieval error covariance matrix,  $\mathbf{S}_x$ , as in Equation (2.4.3).

$$\mathbf{S}_x = \left( \mathbf{S}_a^{-1} + \mathbf{K}^T \mathbf{S}_y^{-1} \mathbf{K} \right)^{-1} \quad (2.4.3)$$

The Jacobian matrix,  $\mathbf{K}$ , represents the sensitivity matrix of the perturbed result of the forward model. The true state  $\mathbf{x}$  is perturbed by 0.2 % and thus  $\mathbf{K}$  represents the relation between simulated values to the true state and how sensitive the simulated values are to small changes when starting a new retrieval cycle. The closer  $\mathbf{K}$  is diagonal, the more is  $\mathbf{x}$  determined by the real observed and a priori values. If the limit of the partial derivative is close to unity, the retrieved value  $\mathbf{x}$  is its true state [Wood, 2011].

In practical application for this multiple layer retrieval scheme, log-transformed particle size distribution parameters of slope and number intercept were used due to the large expected range of these variables. The state vector,  $\mathbf{x}$ , is defined in Equation (2.4.4).

$$\mathbf{x} = \begin{bmatrix} \log(\lambda)_0 \\ \vdots \\ \log(\lambda)_{\text{nlayer}} \\ \log(N_0)_0 \\ \vdots \\ \log(N_0)_{\text{nlayer}} \end{bmatrix} \quad \text{nlayer} = 14 \quad (2.4.4)$$

The usage of a priori terms were explored both from in-situ microphysical observations and from the PSD-temperature relationship developed for the CloudSat scheme as in Equations (2.4.5) and (2.4.6). Temperatures in °C at Haukeliseter were taken from site measurements with an assumption of a moist adiabatic lapse rate for the observed snow events. The log transformed slope and number intercept values were taken from Wood [2011].

$$\log(\lambda) = -0.03053 \cdot T_{ap} - 0.08258 \quad [\log(\text{mm}^{-1})] \quad (2.4.5)$$

$$\log(N_0) = -0.07193 \cdot T_{ap} + 2.665 \quad [\log(\text{m}^{-3} \text{mm}^{-1})] \quad (2.4.6)$$

The log-transformed equations are useful, since the results from C3VP were similar to other observations. The study showed, that  $N_0$  ranges over several order of magnitude as well as  $\lambda$  was non-Gaussian for the snow events Wood [2011]. The diagonal matrix elements in  $\mathbf{S}_a$  (Equations (2.4.1) and (2.4.3)) are equal to 0.133 and 0.95 for the particle slope parameter and the number intercept, respectively, as from Eq. 7.35 and 7.36 in Wood [2011]. The diagonal matrix elements for  $\mathbf{S}_y$  are 2.5<sup>2</sup> in Equations (2.4.1) and (2.4.3).

After the best estimate of PSD parameters are found, the snow water content in each layer is calculated using the snow particle mass-dimension relationships as in Appendix A.1.

$$\text{SWC} = \int_{r_{min}}^{r_{max}} m(r)n(r)dr \quad [\text{gm}^{-3}] \quad (2.4.7)$$

$r$  is the particle maximum dimension and  $m(r)$  the related mass.

This thesis work considered the database of particle models developed for the CloudSat mission, e.g. different types of aggregates, sector plates, and columns. Scattering properties for these snowflakes were calculated for the 24 GHz frequency using discrete dipole approximation (DDA). Observations from the MASC of snowflake habit were used to guide particle selection. Snow water content, in turn, was translated into a snowfall rate using fallspeed observations (MASC, PIP, or MRR Doppler velocity) or climatological analyses. Surface snowfall rate is estimated using the SWC from the lowest non-noise reflectivity and radar bin.

The forward model that calculates simulated 24 GHz MRR reflectivities from PSD parameters was modified from that used in the CloudSat 94 GHz operational snowfall product (2C-SNOW-PROFILE). Backscatter from frozen hydrometeors in each radar bin is summed up as in Equation (2.4.8) form which reflectivity factor, Z, can be found (Equation (2.4.9)).

$$\eta_{bk} = \int_{r_{min}}^{r_{max}} n(r)\sigma_{bk}dr \quad [\text{m}^{-1}] \quad (2.4.8)$$

$$Ze^{ss,na} = \frac{\Lambda^4}{\|K_w\|^2 \pi^5} \eta_{bk} \quad [\text{mm}^6 \text{m}^{-3}] \quad (2.4.9)$$

where,  $\Lambda$  is the wavelength of the radar;  $\|K_w\|^2$  is the complex refractive index of water. Radar backscatter values were estimated using discrete dipole approximation for the CloudSat particle models at 24 GHz. Unlike the 94 GHz spaceborne CloudSat mission, multiple scattering and attenuation can be neglected for 24 GHz MRR and the short path length retrievals as viewed from the ground perspective.

## 2.4.2 ENVIRONMENTAL MASKS FOR THE OPTIMAL ESTIMATION RETRIEVAL

Different steps and assumptions are done in the here presented snowfall retrieval, to achieve vertical profiles of snowfall from MRR. The snowfall rate at the surface can be

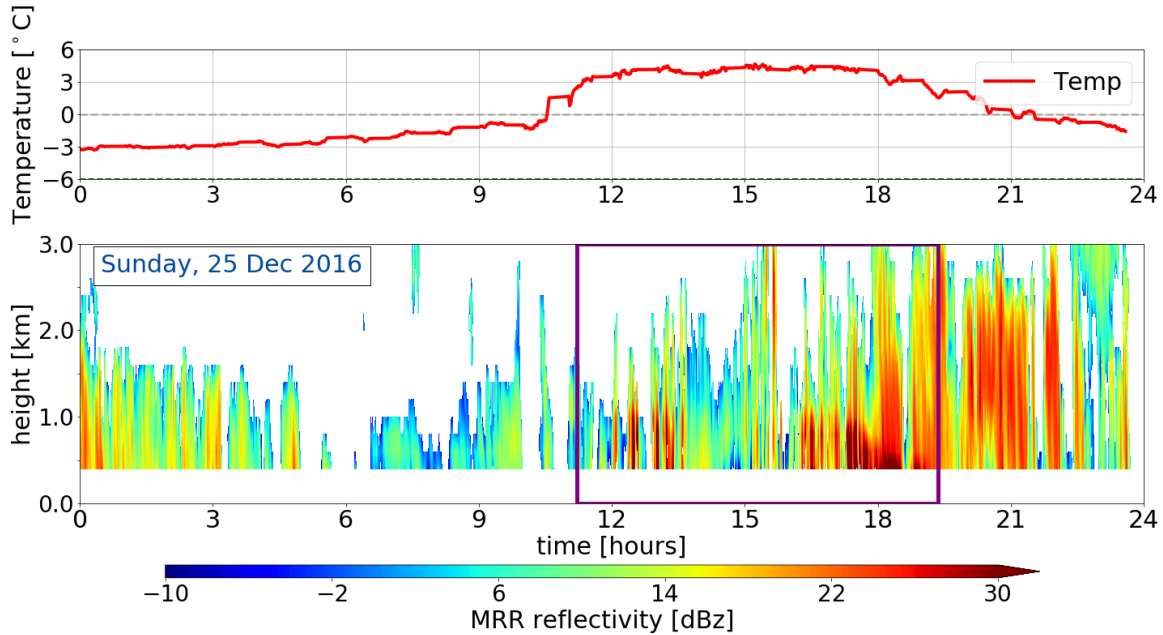


**Figure 2.4.2:** A priori temperature dependence within the optimal estimation retrieval for an all day precipitation event on 25 December 2016. The upper panel shows the surface a priori guess,  $T_{ap}$ , measured at the Haukeliseter site. The lower panel presents the reflectivity measure by the MRR. Additionally, indicates the purple frame the time, where the MRR reflectivity was larger than  $-10 \text{ dBZ}$  and surface temperatures less than  $2^\circ\text{C}$

estimated from one of the lower levels. The optimal estimation retrieval is only performed for profiles, which are likely to have observed snow.

This value was chosen as sensitivity studies [e.g. Wood et al., 2013] that a days worth of such reflectivities would produce only a trace of snow. Such a value therefore guarantees that a significant snow event is not missed and that any storms with lower dBZ values would not produce meaningful precipitation.

The Haukeliseter measurement site is equipped with a weather mast, measuring the air temperature every minute at two-meter height (compare Figure 2.4.2, upper panel). Since the MRR measures above 300 m and temperature measurements exists only at the surface, a priori temperature ( $T_{ap}$ ) at the surface is assumed to be similar to the observed near-surface air temperature. The use of a moist adiabatic lapse rate of  $dT/dz = 5 \text{ K km}^{-1}$  gives  $T_{ap}$  in each layer. Snow existence at temperature measurements up to a threshold of  $+2^\circ\text{C}$  are assumed. Liu G. [2008] validated this threshold, by analysing present weather reports

to find the distinction between liquid and solid precipitation.

The purple line in the lower panel of Figure 2.4.2 represents the time frame during 25 December 2016, where the MRR reflectivity is less than  $-15$  dBZ, and a priori temperature passes the  $2$  °C limit at the surface.

## 2.5 METCOOP ENSEMBLE PREDICTION SYSTEM

MEPS (MetCoOp Ensemble Prediction System) was newly operational at Met-Norway when the extreme weather occurred in Norway. Comparing model data with actual observations helps to verify the agreement between model prediction and ground-based measurements.

AROME-MetCoOp was operational from March 2014 until November 2016, when it was replaced with an ensemble prediction system (EPS) based on AROME-MetCoOp. MEPS is used as weather forecast at the Norwegian Meteorological Institute, the Swedish Meteorological and Hydrological Institute (SMHI) and the Finnish Meteorological Institute (FMI), [Køltzow, 2017, Müller et al., 2017].

### 2.5.1 AROME - METCOOP

In principle, MEPS is a short-term weather forecast consisting of a ten ensemble member forecast system with 66 h prediction time and a horizontal resolution of 2.5 km and 65 vertical levels. One of the members is the deterministic forecast where the other nine present the perturbed state of the deterministic forecast. The initialisation of each member is performed at 0 UTC, 6 UTC, 12 UTC and 18 UTC [MetCoOp Wiki, 2017].

Forecast data saved for the deterministic and first ensemble member have a time resolution of one hour for 66 h. The other eight members have values every three hours for up to 48 h forecast time.

Figure 2.1.1a shows the MEPS model domain and its elevation as it was operational for December 2016. It covers the Nordic Countries including open water such as the Atlantic Ocean, the North and the Baltic Sea. A repres-

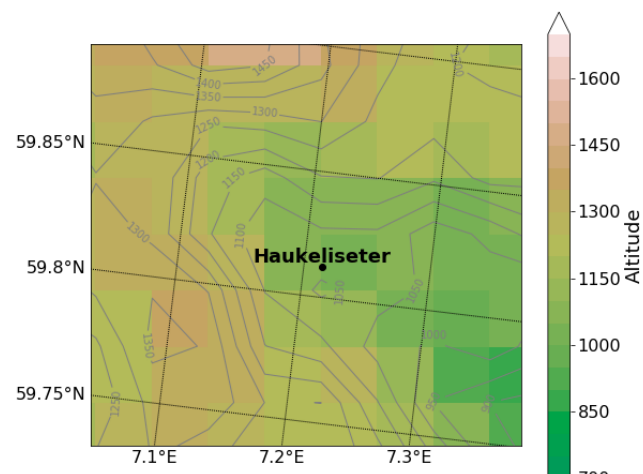


**Figure 2.5.1:** Representation of the topography around measurement site Haukeliseter in MEPS. Contours

entation of the horizontal resolution zoomed on the Haukeliseter site is shown in Figure 2.5.1. Haukeliseter is surrounded by a complex terrain with mountains up to 1500 m no the west and the north and the more open terrain to the south-east.

The centre of the model is approximately at 63.5° N, 15° E. The horizontal grid points are projected on a Lambert projection to receive the same area size of each grid cell. The outer, parent grid is the ECMWF-IFS model (European Centre for Medium-Range Weather Forecasts Integrated Forecasting System) with a horizontal resolution of 9 km [[Homleid and Tveter, 2016](#)]. The ECMWF-IFS forecasts are used 6 h prior to the actual cycle in MEPS.

Vertical hybrid coordinates are terrain-following and are mass-based, [[Müller et al., 2017](#)]. How the vertical hybrid coordinates are transformed into layer thickness or height is described in Section 2.6.1. Furthermore, MEPS underlies non-hydrostatic dynamics, [Met-CoOp Wiki \[2017\]](#).

The representation of snow is covered by a modification of the three-class ice parametrization (ICE3) scheme. Where liquid-phase processes are separated from slow ice-phase processes and described in Section 2.5.2. To model the snow cover an one-layer atmosphere model scheme is implemented. This includes three variables such as: snow water equivalent (SWE), snow density, and snow albedo [[Müller et al., 2017](#)].

As synoptic observations are included in the model the snow-depth predictions underlay a special performance. Observations of snow-depth are only available at 6 UTC and 18 UTC, therefore is the snow analysis only performed twice daily [[Homleid and Tveter, 2016](#), [Müller et al., 2017](#)].

## 2.5.2 MESO-NH AND THE ICE3 SCHEME

The physical parametrization within AROME is based on the French research communities' mesoscale non-hydrostatic atmosphere model (Meso-NH). The microphysical scheme in the Meso-NH atmospheric simulation system is based on the ICE3 scheme. The purpose of the scheme is to model as correctly as possible the ice phase in the atmosphere [[Pinty and](#)

Jabouille, 1998]. McCumber et al. [1991] concluded from their case study, that at least three different ice categories are necessary to cover most precipitation but that applications might be case specific. According to the Meteo France [2009] documentation, the ice phase microphysical scheme must include:

$\mathbf{r}_i$ : pristine ice phase

$\mathbf{r}_s$ : snowflake type from lightly rimed large ice crystals or dry clusters, and

$\mathbf{r}_g$ : heavily rimed crystals, such as graupel, frozen drops or hail

Within the ICE3 scheme no distinction between hail and graupel exists and therefore is the physical discrimination in the growth mode of graupel and hail is neglected.

To achieve snow water content within MEPS the total number concentration, slope parameter, mass diameter and the particle size distribution have to be determined. According to Caniaux et al. [1994] follows the particle size distribution the Marshall-Palmer distribution similar to Equation (2.4.2). The goal is to use a varying number concentration  $N_0$  dependent on the ice category. The study has shown that  $N_0$  can be assumed with

$$N_0 = C\lambda^x \quad (2.5.1)$$

$$\log_{10} C = -3.55x + 3.89$$

where  $C$  and  $x$  depend on the ice category and represent the relation between each other in Equation (2.5.1).

The ice water content for primary ice, snowflakes and rimed crystals is then be assumed to be similar to Equation (2.4.7), but the integration limits range from zero to infinity and mass, and particle size distribution are dependent on the diameter of the particle. The mass diameter and particle size distribution (Equations (2.5.2) and (2.5.3)) are represented depending on the ice category shown in Table 2.5.1

$$m(D) = aD^b \quad (2.5.2)$$

$$n(D) = N_0 g(D) \quad (2.5.3)$$

and  $g(D)$  to be the generalised Gamma function

$$g(D) = \frac{\alpha}{\Gamma(\nu)} \lambda^{\alpha\nu} D^{\alpha\nu-1} \exp(-(\lambda D)^\alpha) \quad (2.5.4)$$

with  $\alpha$ ,  $\nu$  the shape and tail dispersion parameters and  $\Gamma(\nu)$  the gamma function.

After following the above equations including Equation (2.4.7) the slope parameter  $\lambda$  can be generated with  $G(B)$  the gamma function.

$$\lambda = \left( \frac{\text{SWC}}{aCG(b)} \right)^{\frac{1}{x-b}} \quad (2.5.5)$$

**Table 2.5.1:** Characterization parameters from primary ice ( $r_i$ ), snowflakes ( $r_s$ ) and rimed crystals ( $r_g$ ). Values are based on the references in [Meteo France \[2009\]](#) and in [Pinty and Jabouille \[1998\]](#).

	$r_i$	$r_s$	$r_g$
$\alpha, \nu$	3.3	1.1	1.1
$a$	0.82	0.02	196
$b$	2.5	1.9	2.8
$c$	800	5.1	124
$d$	1.0	0.27	0.66
$C$		5	$5 \times 10^5$
$x$		1	-0.5

[Meteo France \[2009\]](#) documentation suggests starting the microphysics in the ICE3 scheme with 'slow' processes such as homogeneous and heterogeneous nucleation (HON, HEN), vapour deposition of snow and graupel particles (DEP), aggregation (AGG) and auto conversion (AUT), for ice processes right side in Figure 2.5.2. The second step is to initiate the warm processes left side in Figure 2.5.2. Then include the aggregation and conversion-melting (CVM) for snowflakes and contact freezing of raindrops (CFR). Add AGG and melting for graupel (MLT), and then the melting from pristine ice and the Wegener-Bergeron-Findeisen (BER) effect and lastly the sedimentation terms.

Figure 2.5.2 shows the summary of the microphysical processes for mixed phase clouds. The study focuses mostly on solid precipitation particles and therefore only the initiation and growth of pristine ice crystals  $r_i$ , snowflakes  $r_s$ , and rimed crystals  $r_g$  is presented.

Following [Pinty and Jabouille \[1998\]](#) and Figure 2.5.2 it can be seen how AROME performs the ice production. Orange lines in Figure 2.5.2 show the initiation of pristine ice

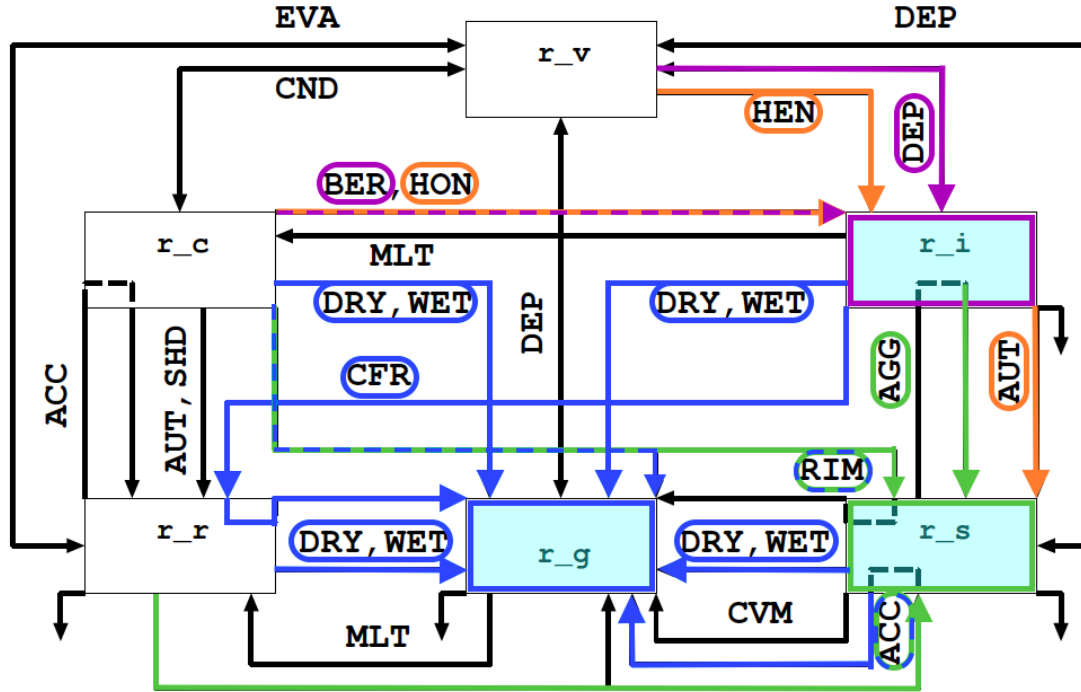


**Figure 2.5.2:** Microphysical processes for mixed phase clouds in the ICE3 scheme adapted from Meteo France [2009]. In orange the initiation processes for primary ice  $r_i$  and snowflakes  $r_s$ . The growing processes of  $r_i$  is shown in purple and for  $r_s$  in green. Graupel particles,  $r_g$ , grow from existent particles and the processes are shown in blue.

crystals and snowflakes. In purple the growth mechanisms of  $r_i$  (BER,DEP). Green lines demonstrate the expansion of the snowflakes (RIM, AGG, ACC). Graupel ( $r_g$ ) forms as an effect of heavy riming (RIM), by collision of larger raindrops with snowflakes (ACC), by WET/DRY growth or by contact freezing of raindrops (CFR). All graupel growth processes are indicated by blue lines in Figure 2.5.2, were hail formation is included.

### 2.5.3 ADJUSTMENT OF ICE3 INSIDE MEPS

Since the ICE3 scheme showed some weaknesses for the winter month, Müller et al. [2017] introduced some modifications. During cold conditions the ICE3-scheme showed too low temperature at two meter, too much ice fog and all year long was the occurrence of cirrus overestimated. After implementing the modifications described in Müller et al.

[2017] the two meter temperature bias was reduced as well as an improvement of low-level clouds was shown. A negative aspect of these adjustments was that the occurrence of fog increased.

## 2.6 NUMERICAL DATA TRANSFORMATION

The following section will describe how the different variables were processed to achieve a comparison between the retrieved values and the forecast model output.

### 2.6.1 LAYER THICKNESS IN MEPS

To compare the measurements from the surface with the MEPS data, the closest grid point to Haukeliseter, is used.

MEPS has a vertical resolution in hybrid sigma pressure coordinates, where one is at the surface and decreases with height. To calculate the actual vertical pressure in Pa, a formula is provided in the OPeNDAP Dataset of `meps_full_2_5km_*.nc` by the [Norwegian Meteorological Institute \[2016\]](#).

$$p(n, k, j, i) = a_p(k) + b(k) \cdot p_s(n, j, i) \quad [\text{Pa}]. \quad (2.6.1)$$

$p_s$  is the surface air pressure in Pa, and information about the variables  $a_p$ ,  $b$  are not given from the access form. [Find reference for sigma-hybrid coordinate transformation equation.](#)

The next step was to convert pressure-levels into actual heights by the use of the hypsometric equation. Here, the air temperature in model levels is used to calculate the mean temperature of each layer.

$$\bar{T} = \frac{\int_{p1}^{p2} T \partial \ln p}{\int_{p1}^{p2} \partial \ln p} \quad [\text{K}] \quad (2.6.2)$$

For the numerical integration, the Simpson rule was used, which is a build-in function in Python.

[Martin \[2006\]](#) presents steps of differentiating the hypsometric equation by using the

virtual air temperature. But when the atmospheric mixing ratio is large, will the virtual temperature only be 1 % larger than the actual air temperature. Since the error is little calculations are done with the provided air temperature in model levels.

The thickness,  $\Delta z$ , of each layer is then be found by using the hypsometric equation from Martin [2006] and the previously calculated mean temperature (Equation (2.6.2)):

$$\Delta z = z_2 - z_1 = \frac{R_d \bar{T}}{g} \ln \left( \frac{p_1}{p_2} \right) \quad [\text{m}] \quad (2.6.3)$$

where  $R_d$  is gas constant for dry air with a value of  $287 \text{ J kg}^{-1} \text{ K}^{-1}$ , standard gravity  $g = 9.81 \text{ m s}^{-2}$ .  $p_1$  and  $p_2$  are the pressure levels at lower and higher levels, respectively ( $p_2 < p_1$ ). To gain the respective height of each pressure layer,  $\Delta z$  is summed.

## 2.6.2 SNOW WATER CONTENT

To get a valid comparison between the SWC from the optimal estimation retrieval and the results from MEPS, the SWC is averaged over each hour. Taking the model initialisation of MEPS at 0 UTC the model produces forecast values at 0, 1, 2, ..., 22, 23, ..., 66 UTC. To approach hourly mean values from the retrieval SWC an average over 30 min prior and 29 min after each full hour is performed. This leads to a match of the average value at the same time as from MEPS.

Since MEPS has a higher vertical resolution than the optimal estimation snowfall retrieval each vertical profile of SWC is averaged every 200 m. To accomplish the same vertical resolution only values above 100 m are used to start at the same range height as given from the MRR (Section 2.3.2).

Within the output from MEPS snow water content does not exist for each model layer. Hence the calculation of the SWC is performed by using the three solid precipitation categories given in MEPS. Namely the instantaneous mixing ratio of snowfall ( $r_s$ ), graupel fall ( $r_g$ ) and the atmosphere cloud ice content ( $r_i$ ). The mixing ratios are represented in  $\text{kg kg}^{-1}$  and a transformation to  $\text{gm}^{-3}$  is performed. Densities in each model level ( $\rho_{ml}$ ) are calculated and then multiplied with the sum of the solid precipitation mixing ratio.

$$\rho_{ml} = \frac{p_{ml}}{R_d T} \quad [\text{kg m}^{-3}] \quad (2.6.4)$$

$$SWC_{ml} = \rho_{ml} \cdot (r_s + r_g + r_i)_{ml} \cdot 10^6 \quad [\text{gm}^{-3}] \quad (2.6.5)$$

### 2.6.3 SNOW WATER PATH

The snow water path (SWP) is the vertically integrated value of the averaged SWC (Equations (2.4.7) and (2.6.5)), where the numerical Simpson's integration is applied.

$$\int_{h_0}^{h_1=3000\text{m}} \text{SWC}(h) dh \approx \frac{h_1 - h_0}{6} \left[ \text{SWC}(h_0) + \text{SWC}(h_1) + 4\text{SWC}\left(\frac{h_0 + h_1}{2}\right) \right] \quad [g\text{m}^{-2}] \quad (2.6.6)$$

The snow water path is a measure of the weight of ice particles per unit area. It indicates the total amount of ice in the atmosphere.

### 2.6.4 ENSEMBLE MEAN AND COEFFICIENT OF VARIATION

#### Check literature of meaning

The ensemble mean is the average of all ten ensemble members of MEPS.

$$\bar{x} = \frac{\sum_{i=1}^n x_i}{N} \quad (2.6.7)$$

The coefficient of variation is known as the standard deviation with respect to their mean of the model output. That means it shows the variation around the center or control run. The standard deviation is defined as:

$$\sigma = \sqrt{\frac{\sum_{i=1}^n (x_i - \bar{x})^2}{N-1}} \quad (2.6.8)$$

which follows for the coefficient of variation:

$$CV = \frac{\sigma}{\bar{x}} \quad (2.6.9)$$

### 2.6.5 MEAN ERROR AND MEAN ABSOLUTE ERROR

The mean error for each ensemble member is calculated with:

$$ME = \frac{\sum_{i=1}^n MEPS_{ens} - DoFe_{obs}}{N} \quad (2.6.10)$$

where  $MEPS_{ens}$  represents the value of each ensemble member and  $DoFe_{obs}$  defines the observation from the double fence. For the mean absolute error follows then:

$$MAE = \frac{\sum_{i=1}^n |MEPS_{ens} - DoFe_{obs}|}{N} \quad (2.6.11)$$

### 2.6.6 PERCENT DIFFERENCE AND AVERAGE DIFFERENCE

The percentage difference presented in the results (Table 4.2.1 and add for MEPS) are calculated by:

$$\% \text{Difference} = \frac{SF - DoFe_{obs}}{DoFe_{obs}} \times 100 \quad (2.6.12)$$

*SF* presents the snowfall from the retrieval or the MEPS ensemble forecast. The average is then taken from all % Difference values to see the difference of the Christmas storm 2016.

# CHAPTER 3: ANALYSIS OF THE CHRISTMAS STORM 2016

Extreme storm Urd was chosen for an in depth examination for a number of intriguing reasons: i) the MEPS forecasting system had recently become the operational model platform for Met-Norway, ii) the Haukerlister site is a WMO sanctioned weather station with single and double fence rain gauge measurements, iii) additional instruments were placed at the site for the winter 2016/2017 season allowing for the vertical profiling of snow properties and snowfall accumulation, and iv) the unique temporal evolution of the precipitation properties during the event.

A preliminary analysis identified periods of both good agreement of snow accumulation measurements by MEPS in comparison to the ground observations, as well as periods of overestimation by MEPS. The above factors make for an interesting study to assess and better understand the usefulness of the measurements in question.

The next sections will provide a definition of an extreme weather event, a description of the weather maps that were utilized, and a presentation of the synoptic scale evolution of the storm.

Prior to the analysis, each weather maps' purpose will be presented to understand the connections between them. All the weather maps are generated using data from ECMWF operational model Cycle 43r1. The analysis consists of 137 model levels and to reduce computational costs is it reduced to the *octahedral reduced Gaussian grid* and then interpolated to a N640 Gaussian grid.

Between the pole and the equator are 640 lines of latitude equally symmetric spaced. This follows 1280 latitude lines for each hemisphere. The resolution along the longitude is  $90^\circ/640$  lines with points getting closer with increasing latitude. This follows a total

number of grid points of  $8 \cdot 640^2$  [Dando, 2016].

### 3.1 EXTREME WEATHER

'Extreme weather' is a meteorological term, associated with the extent of a weather type. The Norwegian Meteorological Institute declares an extreme event, if strong winds, large amounts of precipitation and large temperature changes are expected before the event occurs. As well as a large avalanche risk is present and coastal areas are influenced by extremely high-water levels. Generally, an event is divided into four phases that it can be called extreme [Pedersen and Rommetveit, 2013].

**Phase A:** *Increased monitoring before the possible extreme weather.* The meteorologists give special attention to the weather situation. At this point it is not certain, that there will be an extreme weather event.

**Phase B:** *Short-term forecasts.* It is decided, that there will be an extreme event. The forecasts are more detailed, and updates will be published at least every six hours. The event will get a name.

**Phase C:** *The extreme weather is in progress.* The meteorologists send out weather announcements at least every six hours.

**Phase D:** *The extreme weather event is over. Clean-up and repairs are in progress.* When the extreme weather is over the public is notified and information about the upcoming weather and clearing work is given.

The Christmas storm was deemed an extrme event by the Met-Norway, named Urd [Olsen and Granerød, 2017]. The average wind along the coast of Western Norway reached hurricane strength (observed:  $40 \text{ ms}^{-1}$  to  $55 \text{ ms}^{-1}$ ). In South and Eastern Norway, west to north-west winds between  $25 \text{ ms}^{-1}$  to  $40 \text{ ms}^{-1}$  were measured. At Haukeliseter, 136.4 mm of precipitation were measured from 21 to 27 December 2016. The event was just above the limit of been called an extreme weather event.

### 3.2 DYNAMIC TROPOPAUSE MAP

The dynamic tropopause maps (DT), presented herein are comprised of the potential temperature (shading) and wind barbs [ $\text{ms}^{-1}$ ] on the two PVU surface (one PV unit =

$10^{-6} \text{ m}^2 \text{ s}^{-1} \text{ K kg}^{-1}$ ), and the 925–850 hPa averaged relative vorticity (black contours - every  $0.5 \times 10^{-4} \text{ s}^{-1}$  only positive values are plotted). An example is presented in ??.

High (low) values of potential temperature represent and elevated (suppressed) tropopause. Regions with a large horizontal gradient of potential temperature indicate a steeply-sloping tropopause that is associated with an enhanced pressure gradient force and winds. The low-level averaged relative vorticity is plotted to provide a 3-dimensional (in the vertical) picture of the atmosphere. It is useful for identifying cyclone centres and attendant frontal boundaries.

The 925 –850 hPa layer-averaged surface relative vorticity is shown in black contours, every  $0.5 \times 10^{-4} \text{ s}^{-1}$ . It represents the rotation of a fluid. **Does the relative vorticity need more explanation?**

Along the Rossby-Wave-Guide **Define what I mean by Rossby-Wave-Guide**, troughs and ridges are seen which can be combined with the surface relative vorticity to understand the vertical dynamic interaction in the atmosphere. In case of a westward tilt between the surface cyclone and an upper level through an intensification of the surface cyclone is more likely to occur.

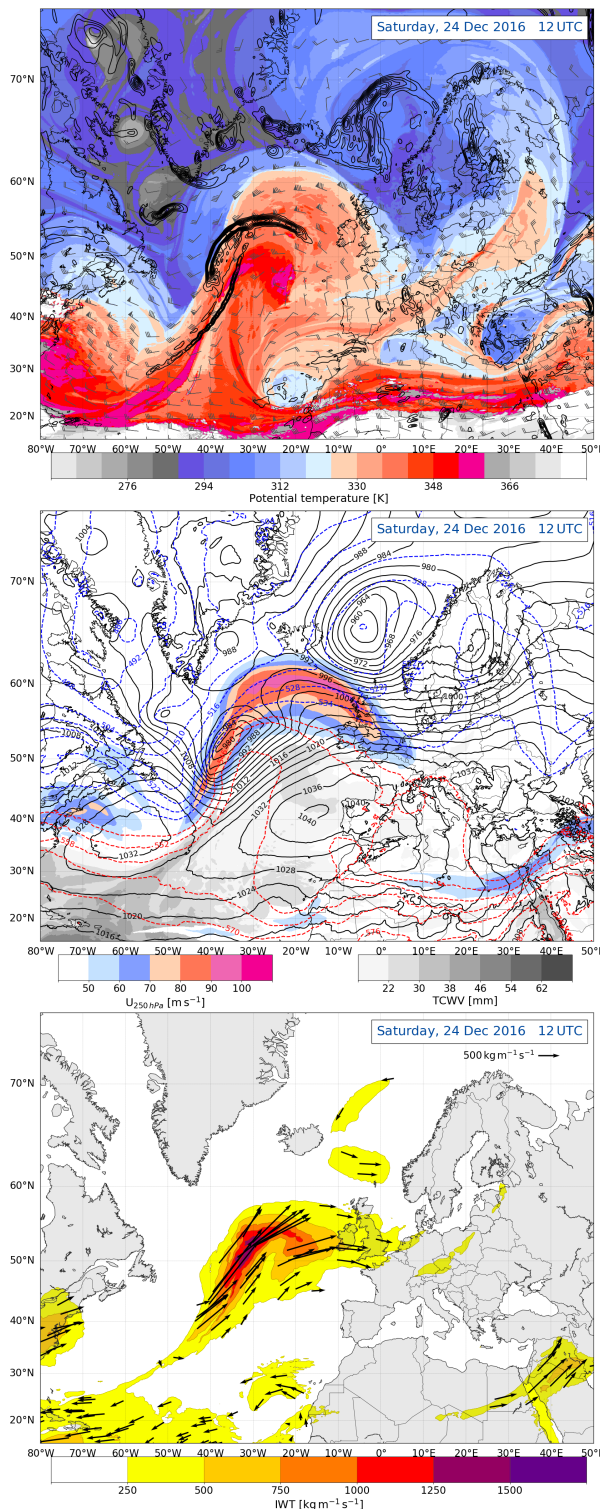


Figure 3.2.1: ECMWF analysis on 24 December 2016 at 12 UTC.

**a:** Dynamic tropopause analysis map at 2 PVU. Potential temperature [K] at the 2 PVU surface, shaded according to the colour bar. Total wind, barbs [ $\text{ms}^{-1}$ ], and 925 -- 850 hPa layer-averaged surface relative vorticity (black contours, every  $0.5 \times 10^{-4} \text{ s}^{-1}$ ).

**b:** Jet, thickness, mean sea level pressure, and moisture synoptic analysis. 250 hPa wind speed, shaded according to the colour bar, [ $\text{m s}^{-1}$ ]. 1000 – 500 hPa thickness, dashed contours every 6 dam, MSLP, black contours every 4 hPa, total column water vapour [mm], shaded according the grey scale.

**c:** Atmospheric river analysis map. IVT, shaded according to the colour bar [ $\text{kg m}^{-1} \text{s}^{-1}$ ]. Vectors, indicating the direction and magnitude of the IVT.

### 3.3 THICKNESS, SEA LEVEL PRESSURE, TOTAL PRECIPITABLE WATER, AND WIND AT 250 hPa

A complementary view of the 3-dimensional structure of the atmosphere is also presented: 250 hPa wind speed (color shading,  $\text{m s}^{-1}$ ), mean sea level pressure (black contours, hPa), 1000–500 hPa thickness (dashed contours) and the total precipitable water (black-white shading, mm). See Figure 3.2.0b for an example.

The dashed, coloured contours show the vertical thickness between the 1000 hPa and 500 hPa surface, every 6 dam. The thickness between two pressure levels can be interpreted via the hypsometric equation (Equation (2.6.3)), which equates the thickness to the mean temperature of the layer in question. In a relative sense, a larger thickness indicates a warmer air mass. In addition, strong horizontal gradients in the thickness field can be related to frontal boundaries. Specific to the discussion herein, the thickness field is also provides useful information regarding the form of precipitation (rain, snow).

Analysis of the mean sea level pressure can be used to identify cyclones and anticyclones at the surface as well as provide supplementary information regarding frontal boundaries. The total precipitable water is a measure of the column integrated moisture. The 250 hPa wind speeds are used to identify strong upper-level flow (i.e. the jet stream) and can be directly compared to the DT map. It represents an instantaneous measure of moisture in time and space, which can be useful when assessing the amount of moisture that may fall as precipitation in future time steps.

### 3.4 INTEGRATED VAPOUR TRANSPORT

Figure 3.2.0c shows coloured contours of the integrated vapour transport (IVT) in  $\text{kg m}^{-1} \text{s}^{-1}$ , where warmer colours indicate higher IVT. Stream vectors indicate the direction and intensity of the IVT flow. An atmospheric river is characterised if the integrated vapour transport shows values higher than  $250 \text{ kg m}^{-1} \text{s}^{-1}$  and a continuous region larger than 2000 km [Rutz et al., 2014].

An atmospheric river (AR) is a filament structure of intense moisture transport from the tropics to higher latitudes. Heavy precipitation can be associated with it, because the air is warm and moist. This can often be observed at mountain ranges at west coasts such as in

Norway [include reference here](#). Due to orographic lifting will the moisture be released and follow high amounts of precipitation.

The integrated vapour transport (IVT) was calculated from the ECMWF data as followed:

$$IVT = \frac{1}{g} \int_{p_{sfc}}^{100 \text{ hPa}} q \mathbf{V} dp \quad [\text{kg m}^{-1} \text{s}^{-1}] \quad (3.4.1)$$

where  $g$  is the standard gravity,  $q$  the specific humidity, and  $\mathbf{V}$  the total wind vector at each pressure level  $p$ . The numerical, trapezoidal integration is performed by using data from the surface pressure  $p_{sfc}$  to 850 hPa in 50 hPa intervals and from 700 hPa to 100 hPa in 100 hPa intervals.

[Add here something like this: The Christmas storm was an atmospheric event, but not in the classical way, hence the atmospheric river case is not discussed in depth.](#)

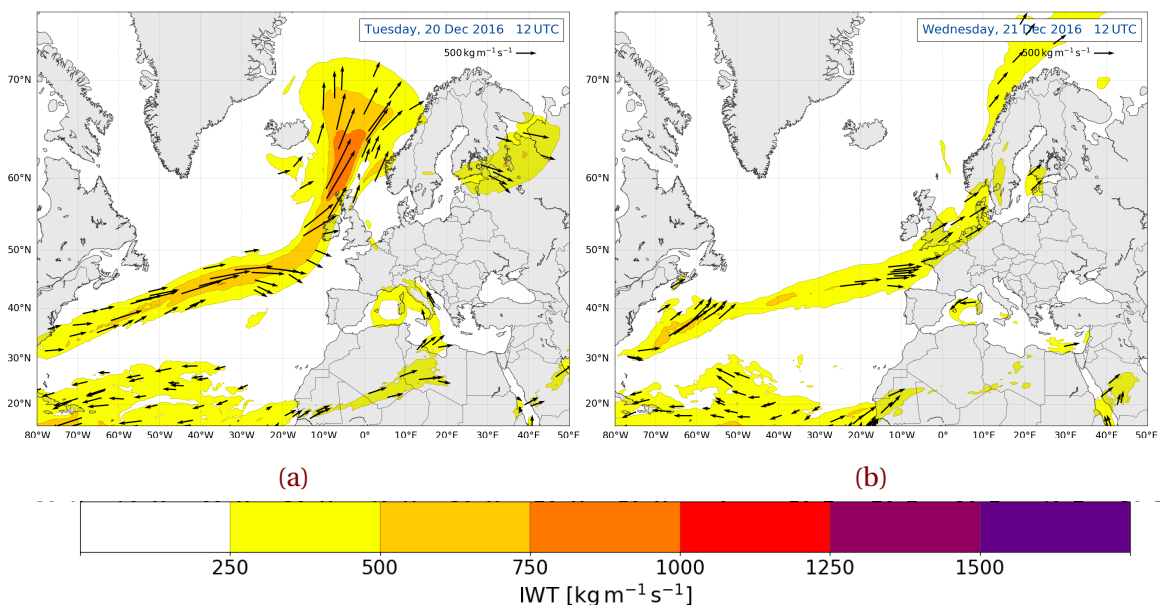


**Figure 3.4.1:** Atmospheric river analysis map, data from ECMWF. During 20 December 2016 to 27 December 2016. IVT, shaded according to the colour bar  $[\text{kg m}^{-1} \text{s}^{-1}]$ . Vectors, indicating the direction and magnitude of the IVT.

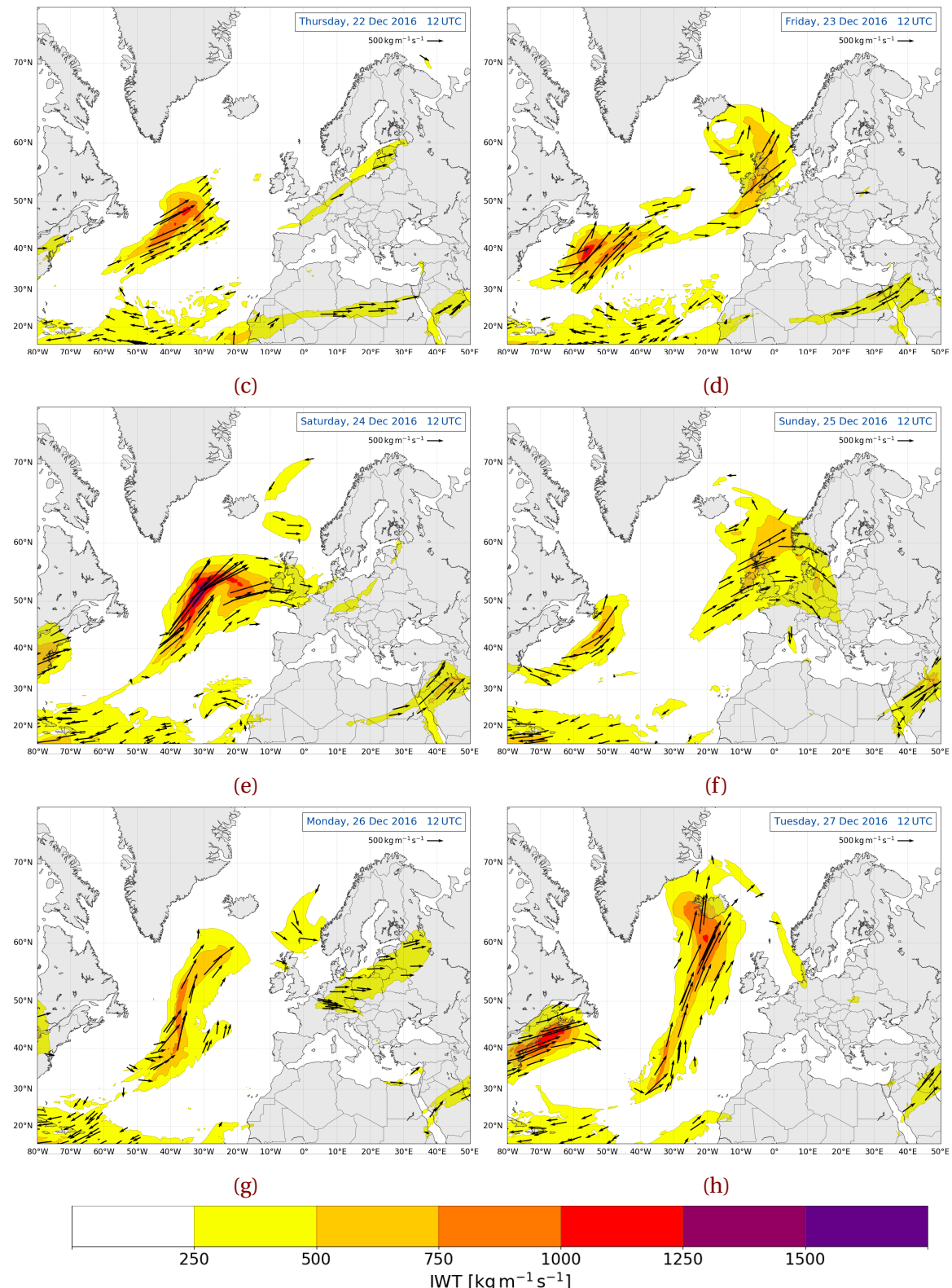
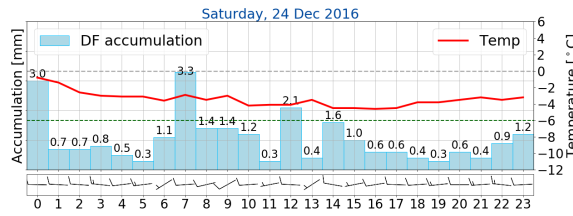


Figure 3.4.1: (Continued from previous page.)



**Figure 3.5.1:** Observation from the weather mast at Haukeliseter during 24 December 2016. 60 min total accumulation [mm] in light blue as bar, temperature (red, [ $^{\circ}\text{C}$ ]), and wind as barbs [ $\text{m s}^{-1}$ ]. Gray dashed line indicates the freezing temperature and the green dashed line the 30-year climate mean temperature at  $-6\text{ }^{\circ}\text{C}$ . Hourly processed data taken from [eklima \[2016\]](#).

## 3.5 OBSERVATIONS AT THE WEATHER MAST

It is a primary goal of this work to relate the local weather observations from the WMO site at Haukeliseter to the synoptic scale structure and the additional measurements taken at Haukeliseter during the winter of 2016/2017.

Examples of the 60 min precipitation accumulation from the double fence rain gauge are presented in Figure 3.5.1 to document the continuous precipitation at Haukeliseter during the extreme event. The temperature evolution will be used to investigate possible changes in the type of precipitation.

Snowfall is likely for temperatures up to  $2\text{ }^{\circ}\text{C}$ . The intensity of the storm can be classified by the hourly averaged wind speed and direction as wind barbs in  $\text{m s}^{-1}$ . To understand which damage a storm can have, [Færaas et al. \[2016\]](#) released a table to associate wind strength with damage (see Table 3.5.1).

## 3.6 LARGE SCALE CIRCULATION

Some text to get a flow.

21 December 2016

The dynamic tropopause map in Figure 3.6.1b shows that Norway is influenced by a change of elevated tropopause to a suppressed tropopause during 20 December 2016 to 21 December 2016. Hence the potential vorticity changed from positive to negative at

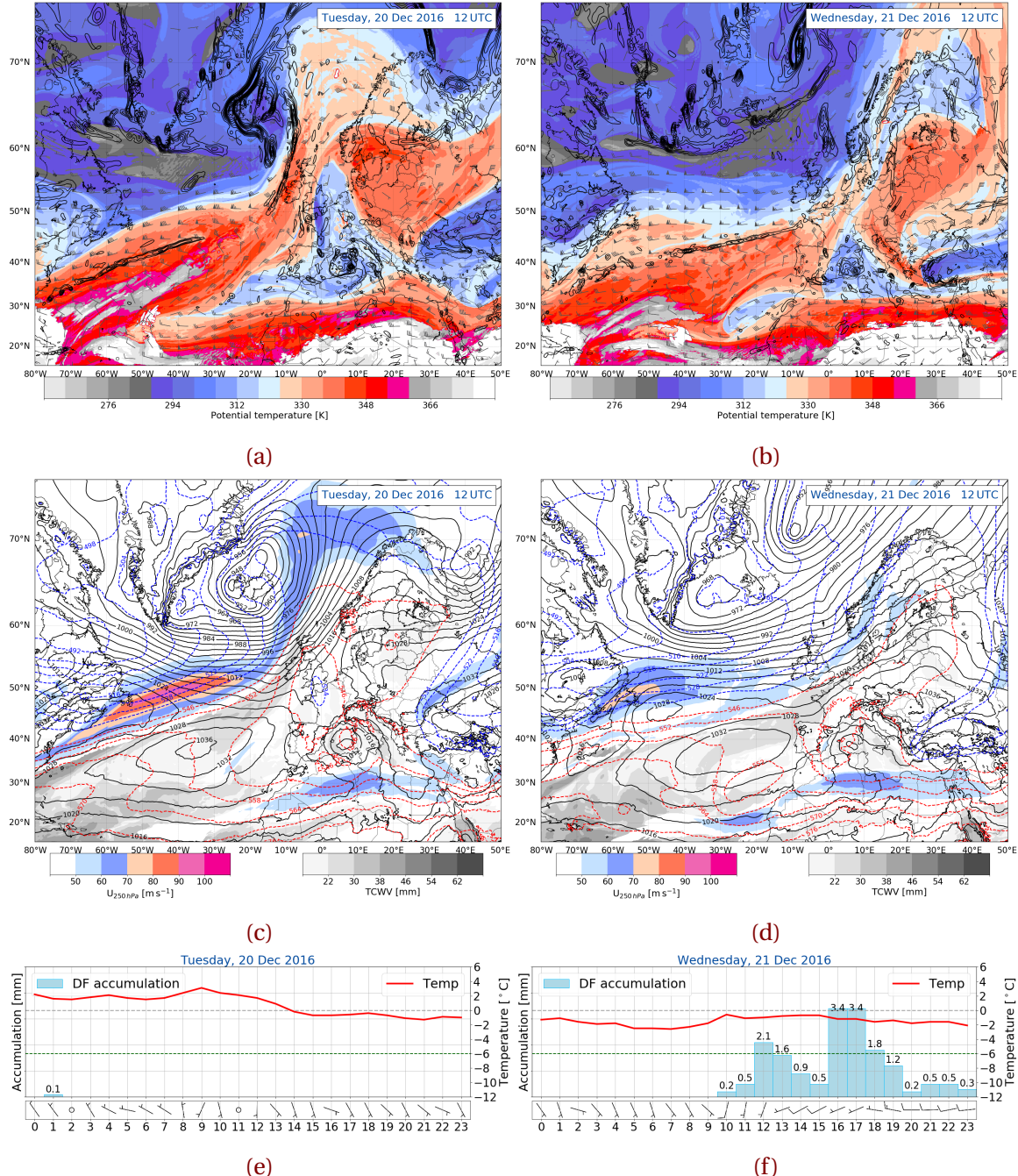


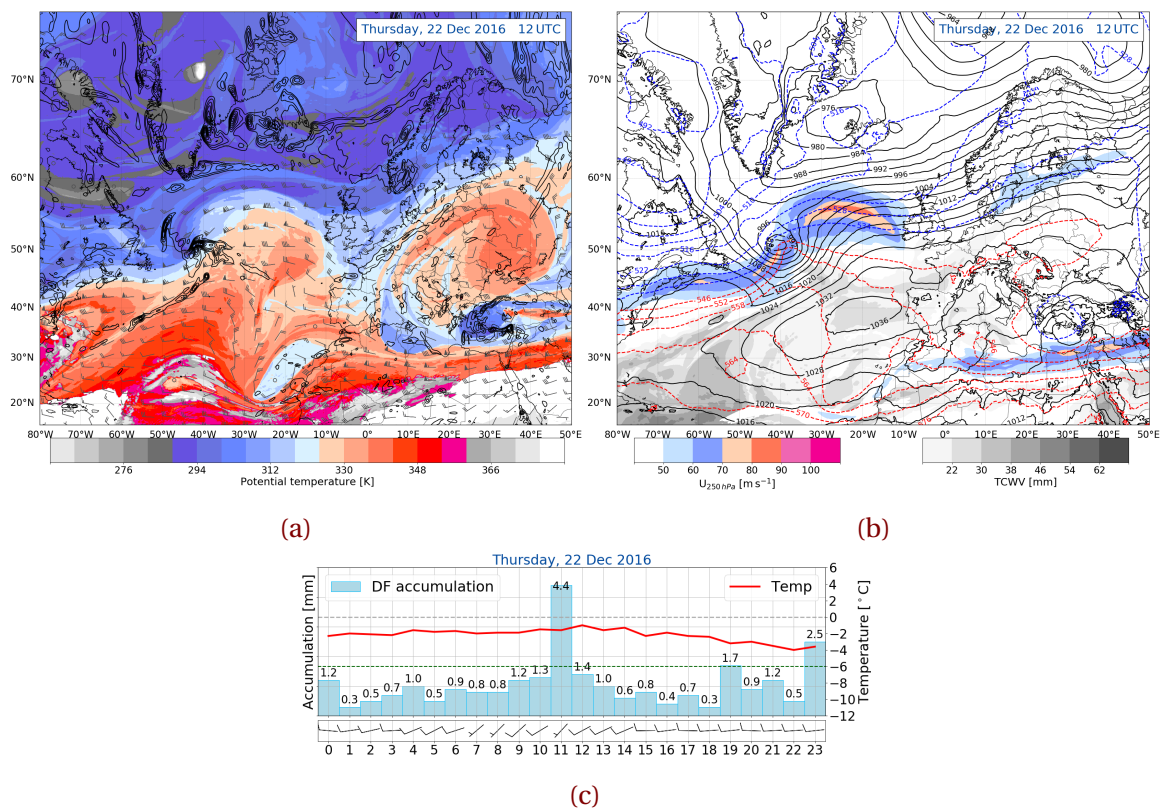
**Table 3.5.1:** Damage related to wind speed, from Færaas et al. [2016].

slight storm	$20.8 \text{ ms}^{-1} - 24.4 \text{ ms}^{-1}$	Large trees sway and hiver. Roofs can blow down.
full storm	$24.5 \text{ ms}^{-1} - 28.4 \text{ ms}^{-1}$	Trees are pulled up with clutter. Big damages to houses.
strong storm	$28.5 \text{ ms}^{-1} - 32.6 \text{ ms}^{-1}$	Extensive damage.
hurricane	$>32.6 \text{ ms}^{-1}$	Unusually large destruction.

the tropopause and cold air stretches right over Norway. A good amount of moisture is transported from the low latitudes to high latitudes, influencing Norway's west coast. This can be seen in the surface maps (Figure 3.6.1d) as well as in the atmospheric river maps (Figure 3.4.1b). The westerly flow in Figure 3.6.1d is conducive to orographic lifting. The precipitation was probably snow when having a look at the moisture content and the cold air. The change from warm air to cold air can also be observed in the time series of temperature in Figure 3.6.1f. And the westerly flow, combined with a good amount of vapour transport from the tropics led to orographic lifting and precipitation at the Haukeliseter site. At around  $60^\circ \text{W}$  a formation of a cyclone at the baroclinic zone can be implied.

22 December 2016

Twenty-four hours later the analysis shows from 22 December 2016 phasing between the surface relative vorticity and the baroclinic zone at  $50^\circ \text{N}$  in the DT. The centre of the surface low is directly located below the temperature gradient at the 2 PVU surface, hence this is good for synoptic lifting. Furthermore, the strongest baroclinicity is observed on the south west side of the surface low. The synoptic map of the geopotential thickness and the surface pressure show the beginning of the frontal boundaries in Figure 3.6.2b. At the same time shows the AR map, Figure 3.4.1c, large values just at the baroclinic zone, where the low pressure is beginning to form. **Help?! Does that lead to even more lifting in this area? Or does it just mean that the cyclone gets a good amount of moisture?!** Norway is



located in a cold area. The continues precipitation observed at Haukeliseter (Figure 3.6.2c) is associated with the westerly flow which is conducive to orographic lifting, and therefore moisture release.

### 23 December 2016

**Use the 12UTC and 18UTC analysis** The begin of the ridging on the 22 December 2016 is more pronounced 24 h later. The warmer air pushes away the cold air, which covered Norway. The low-pressure system moved north-east and lies south of Iceland. The occluded front of this system passes through Haukeliseter, which is why a temperature 'jump' observed at 14 UTC. After this, Southern Norway is influenced by the warm sector, monitored as a temperature increase. The AR, as well as the total column water vapour amount in Figure 3.4.1d and Figure 3.6.3c, respectively show the amount of moisture, transported from low latitudes.

At the same time forms a second cyclone at the baroclinic zone at 40° N. The atmospheric river map (Figure 3.4.1d) indicates a large amount of moisture at this latitude. Again, moist, warm air is conducive to intensify the surface cyclone. In addition, shows the DT map a phasing between the low-level vorticity and the upper level baroclinic zone.

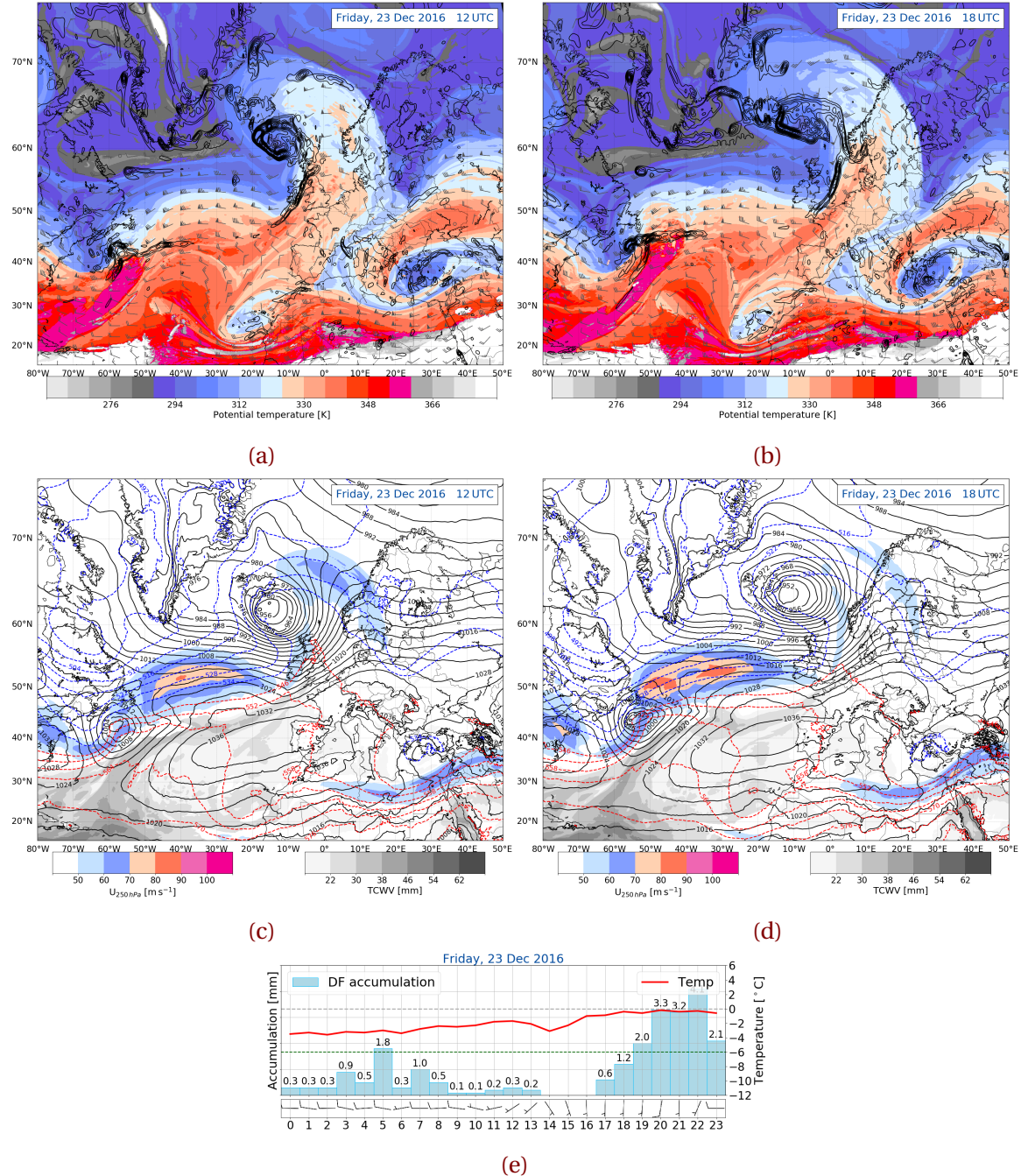
### 24 December 2016

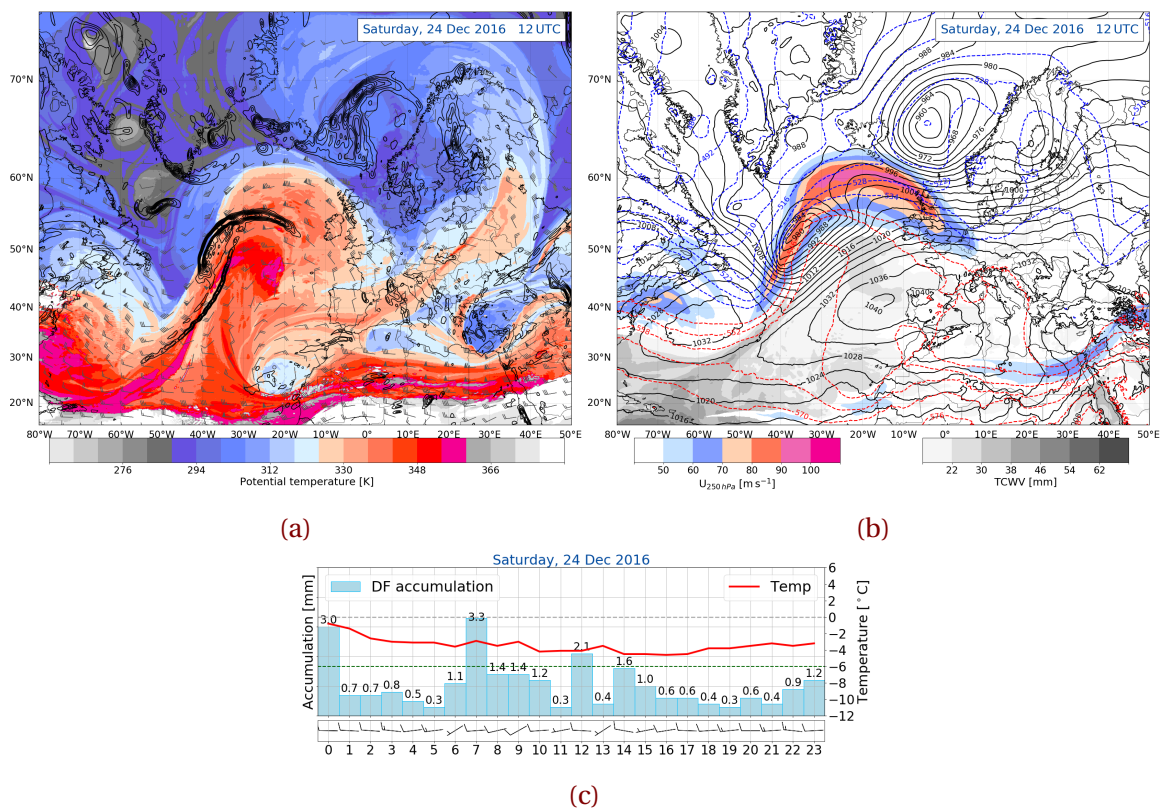
After the passage of the cold front over Norway, Scandinavia is within colder air (compare Figure 3.6.4a and Figure 3.6.4b for 24 December 2016). Over the Atlantic warmer air starts to push the colder air northward. **something something with the low-level vorticity and lifting; lifting at the right entrance region of the jet streak, and very high IVT.**

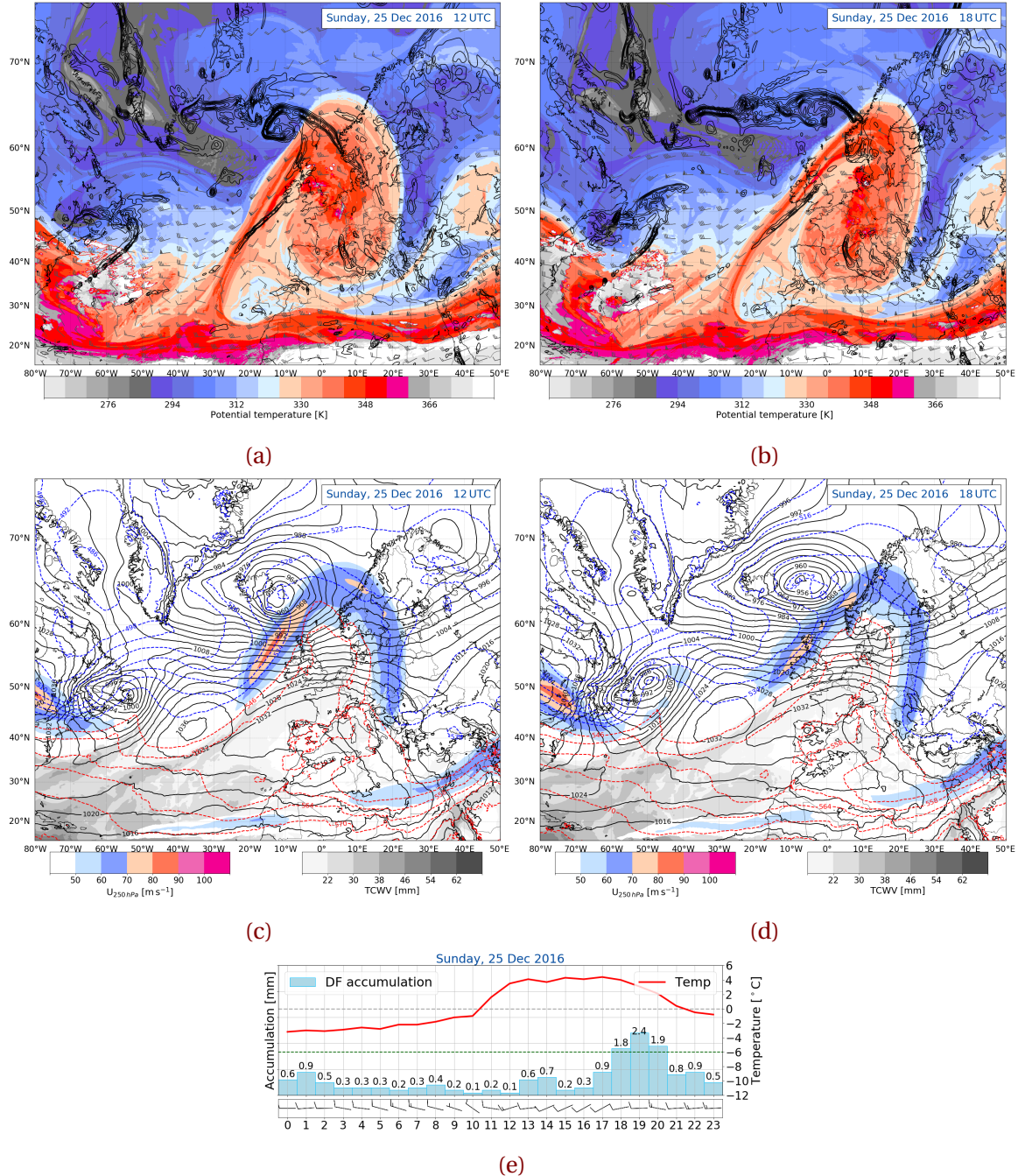
At Haukeliseter negative temperature up to  $-4^{\circ}\text{C}$  is observed, compare Figure 3.6.4c. The westerly flow is again conducive for orographic lifting and associated precipitation.

### 25 December 2016

**Use the 00UTC and 12UTC analysis** Twenty-four hours later the ridge is more pronounced and covers large parts of Norway. The surface low south-east of Iceland has built its frontal boundaries, which can be seen in the low-level vorticity of Figure 3.6.5a. The warm front lies west of Haukeliseter and starts to be observed at the measurement site







(compare Figure 3.6.5e for 25 December 2016). Figure 3.4.1f indicating the integrated vapour transport shows that a lot of moisture is transported from the Atlantic, towards Great Britain and south-western Norway. Together with the lifting at the surface boundary a sufficient amount of precipitation is observed.

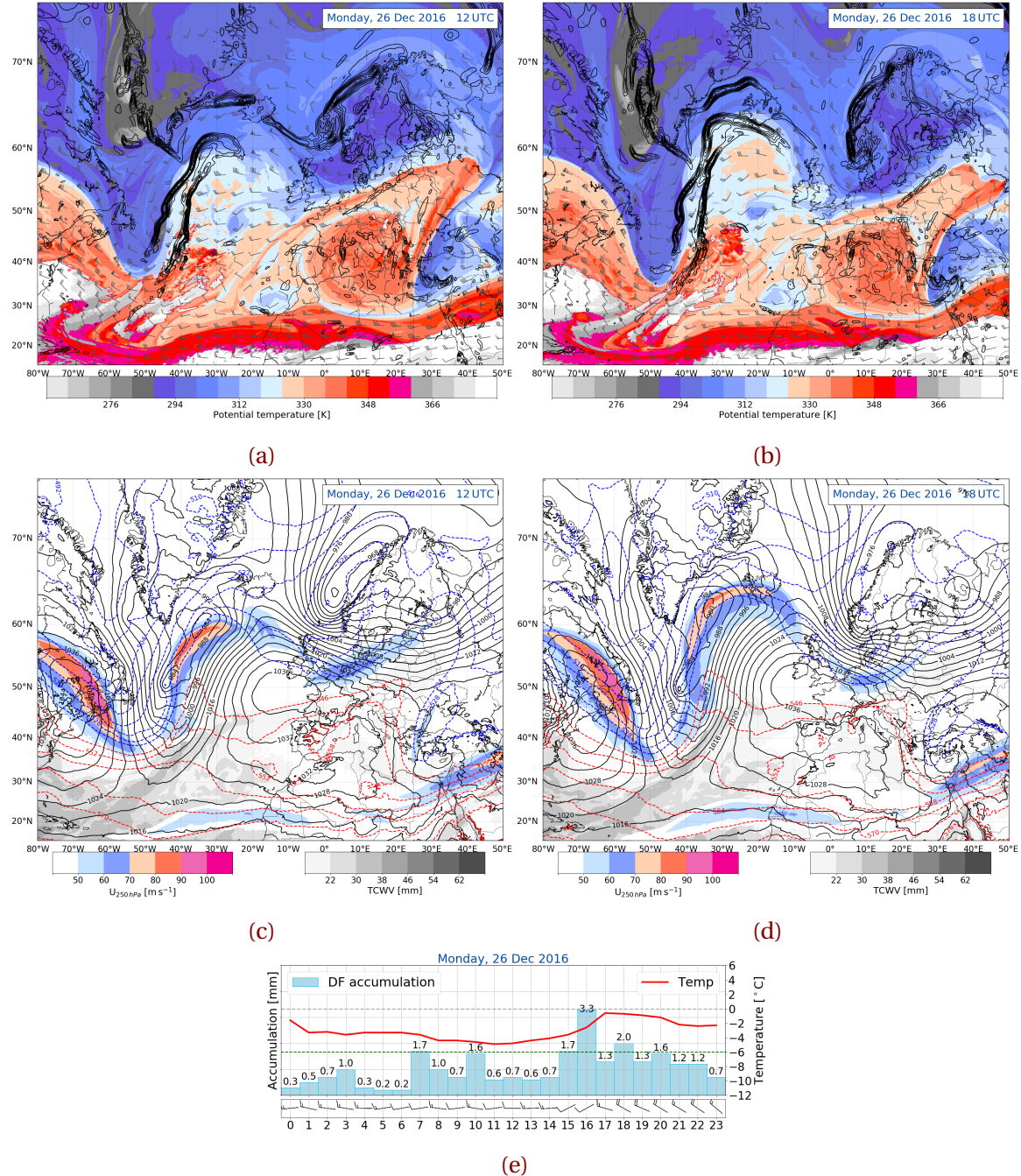
Since the ridging brings moister (Figure 3.4.1f), warm air (Figure 3.6.5a) and Norway lies in a warm sector (Figure 3.6.5c) the assumption will be made, that the precipitation changed from solid to liquid.

### 26 December 2016

**Use the 12UTC and 18UTC analysis** Within the next twenty-four hours the cold front passed through (temperature change in Figure 3.6.6e for 25 December 2016 to 26 December 2016). Norway is covered in cold air (Figure 3.6.6a). The surface low-level indicates the occlusion of the cyclone and therefore a weakening. The wind is still from the west which is helpful for orographic lifting. The moisture content is still present but much weaker and smaller in extend. Since Norway is covered in cold air, the temperature is below zero and the precipitation had to be solid.

### 27 December 2016

The images of 27 December 2016 show that the storm passed and disappeared. Southern Norway lies in cold air (??), but on the right exit region of the jet (→ sinking motion of cold air), compare ?? . A small amount of moisture is present (Figure 3.4.1h). Because of the wind change from west to north-west follows that orographic lifting is not present and the precipitation amount decreases at the end of the storm.



## CHAPTER 4: RESULTS AND DISCUSSION

In this chapter the results of the surface observation, the optimal estimation retrieval and the regional mesoscale forecast model are presented. On the basis of the methodology described in Chapter 2 it should be evaluated if a regional mesoscale forecast model predicts the same synoptic patterns as observed at the measurement site. Also, vertical SWC forecasted by MEPS is being compared with the retrieved vertical SWC at Haukeliseter. Attention should be paid to the fact, that this study is unique. The motivation to compare regional model forecasts with vertical snowfall measurements resulted from a study by Joos and Wernli [2012]. They did sensitivity studies on the microphysical scheme of COSMO (COncsortium for Small-scale MOdelling) and found that the storm development depends on the correct vertical placement of the precipitation inside a modeled storm. Vertical precipitation determines the vertical profile of latent heating, and hence the generation of potential vorticity which in return shows if a storm strengthens or weakens. Correct vertical precipitation observations can then help to correctly assess model vertical precipitation patterns.

## 4.1 SENSITIVITY OF THE OPTIMAL ESTIMATION RETRIEVAL

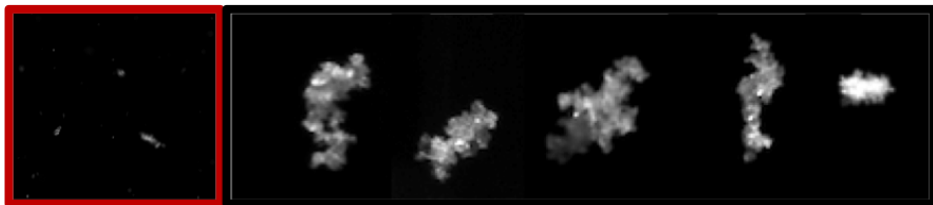


**Figure 4.1.1:** MASC observations during the Christmas storm 2016. Left (red frame), small ground up blowing snow particles. Five images on the right, rimed particles.

The optimal estimation retrieval scheme was applied to the six-day Christmas 2016 storm event. MASC images of snowfall during the event were used to guide the selection of the appropriate particle model and PSD input for the retrieval scheme. In this section, the sensitivity of retrieval results to these inputs is explored. Such an exercise should also allow an identification of those properties that yield the best match with Met Norway snow gauge measurements at Haukeliseter.

The majority of the MASC images from Haukeliseter contained snow particles that looked like the left image Figure 4.1.1. Such images suggest small ground-up blowing snow particles that are consistent with the high winds observed during the event. However, a careful examination of the MASC images also finds the presence of rimed aggregates such as those in the right five images Figure 4.1.1. Pristine crystals such as plates and columns were not observed during this event. As such, we explored the use of two different aggregate particle models developed for the CloudSat mission.

Figure 4.1.2 presents hourly measured snowfall accumulations on 22 December 2016 plotted against retrieved values for the two different aggregate assumptions. The 'B8' aggregate is a low reflectivity per unit mass aggregate that worked well for the cold, dry conditions observed at Barrow as described in [Cooper et al. \[2017\]](#). The 'B6' aggregate is a high reflectivity per unit mass particle. As such, the 'B6' aggregate would seem more physically consistent with the observed rimed particles and high water environment found in the coastal mountains at Haukeliseter. The presence of a water or rimed coating on the aggregates aloft would greatly enhance their effective reflectivity. Indeed, Figure 4.1.2 suggests that the reflective 'B6' aggregate agreed much better than the less reflective 'B8' aggregate with the snow gauge.

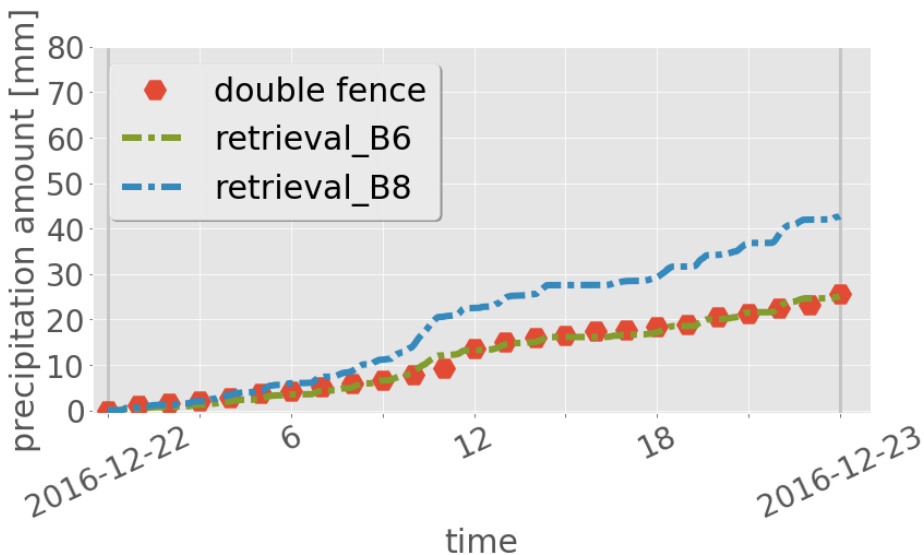


**Figure 4.1.2:** Hourly double fence snowfall accumulations [mm] plotted against retrieved values for the 22 December 2016 for different retrieval assumptions permutations. Double fence snowfall accumulation, red hexagons, retrieved precipitation amount for the here used study (B6), green, dash-dotted, and for small aggregates (B8), blue dashed.

Table 4.1.1 presents the percentage differences between snow gauge and retrieved estimates found when using these particle model assumptions for 22 December 2016. Use of the 'B6' aggregate agreed within 5 % of the double fence observations (Table 4.1.1) for both 12 h and 24 h surface accumulations. Admittedly, use of the 'B6' aggregate produced slightly too little snowfall relative to the gauges for the remaining days of the event as discussed in Section 4.2. The use of the 'B8' aggregate, however, overestimated snowfall by at least 65 % for both the 12 h and 24 h surface accumulations (Table 4.1.1). Since this aggregate had low reflectivity per unit mass, it required significantly more SWC in the forward model calculations to match MRR reflectivities. The retrieval therefore overestimates snowfall rate for these meteorological conditions.

The discussion here has focused on MASC estimates of habit instead of PSD or fall speed. The reason is that the MASC and PIP saw primarily blowing snow particles at the surface that likely were much smaller than the particles that the MRR remotely sensed aloft.

**Table 4.1.1:** Observations (obs.) and retrieved (ret.) snowfall amounts for 22 December 2016 for different particle model assumptions. B6 indicating the here uses particle model (Appendix A.1) and B8 indicating the retrieved snowfall amounts for small particles.

Particle model	12 h accumulation				24 h accumulation			
	Snowfall		Difference	Snowfall		Difference		
	obs.	ret.		obs.	ret.			
	[mm]		[%]	[mm]		[%]		
B6	13.6	13.2	-3.0	23.1	25.1	-2.1		
B8	13.6	22.5	+65.5	23.1	42.7	+66.9		

The use of the PSD measured by the MASC or PIP in the retrieval therefore produced snowfall totals much greater than those measured by the double fence snow gauges. Essentially, it takes a much greater mass of small particles than large particles to match a given reflectivity. These results contrast with those found for low wind speed events at Haukeliseter where the use of MASC habit, PSD, and fall speed observations resulted in retrieved snowfall accumulations very close to Met Norway snow gauge observations. Regardless, for this high wind event, the [Wood \[2011\]](#) a priori temperature PSD relationship and a climatological average fallspeed of  $0.85 \text{ m s}^{-1}$  [private communication, ?] were employed.

## 4.2 COMPARISON OF SURFACE OBSERVATIONS

To be able to compare the vertical predicted snow water content with the retrieved snow water content a verification of the surface accumulation is made. If the retrieved surface accumulation is confident in comparison to the double fence measurement, then the vertical measurements can be trusted.

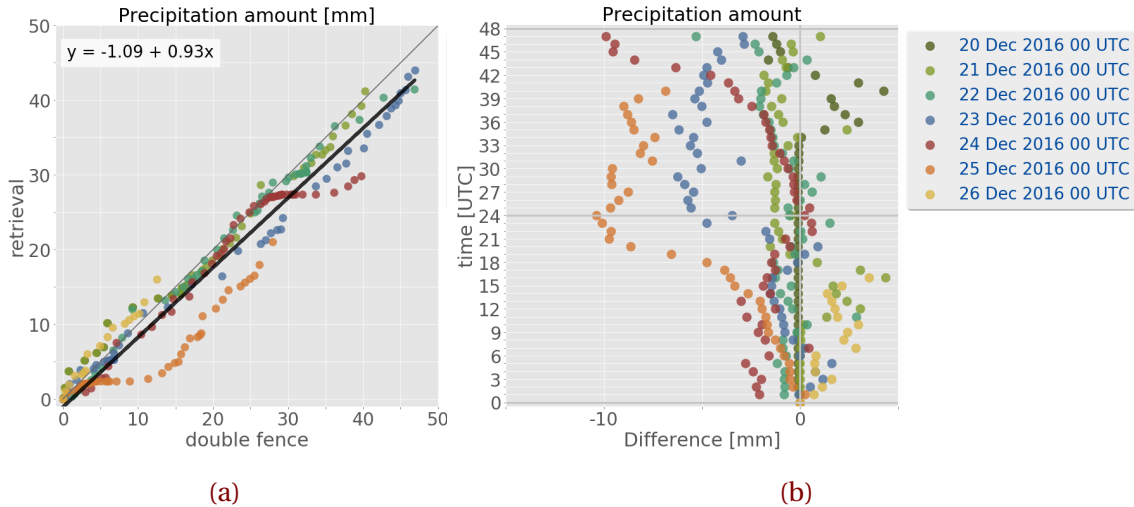
The correlation in Figure 4.2.1a demonstrates a good agreement between the 48 h accumulation measured by the double fence and the retrieved surface accumulation. The black line in Figure 4.2.1a presents a linear correlation with a regression coefficient of  $R = 0.97$ . In general, the retrieved surface snowfall accumulation is underestimated when compared to the double fence measurements, but not to a large degree.

Figure 4.2.1b shows the difference between retrieved accumulation and observed accumulation by the double fence. For the time period 20 to 24 December 2016, Figure 4.2.1b indicates an underestimation of retrieved snow accumulation of less than  $-5\text{ mm}$  for the first 24 h. Snow accumulation calculated on 23 December 2016 at 0 UTC show after 24 h an underestimation by the retrieval of up to  $-6.5\text{ mm}$ . Larger underestimation after 43 h is related to the observation of liquid precipitation on 25 December 2016 between 12 UTC to 21 UTC for accumulations on 24 December 2016. On 25 December 2016 no fair comparison to the double fence measurement can be performed after 12 UTC because of the neglection of liquid precipitation when temperatures exceed  $2\text{ }^{\circ}\text{C}$ .

For a 12 h accumulation follows for the Christmas storm (20 to 26 December 2016) an average error of 85.5 % (Table 4.2.1). For longer, 24 h accumulation decreases the average error to be  $-4.7\%$  (excluding values on 25 December 2016 after 12 UTC and on 26 December 2016 after 17 UTC because of attenuation at the MRR). The daily surface snowfall accumulation difference between retrieval and observation in Table 4.2.1 show almost always a well agreement to the boundary condition of the double fence. The only well pronounced mismatch is seen non 21 December 2016, where it measures much more than the double fence gauge (+435.8 %).

Similar to this study, Cooper et al. [2017] used a CloudSat snow particle model, PSD and fall speed from MASC observations for five snow events at Barrow, Alaska. The comparison to the weather station revealed an difference between National Weather Service observations and retrieved accumulations of  $-18\%$  for all five snow events.

Table 4.2.1 shows the difference for each individual day and the average difference for six and 4 days, depending on the accumulation of 12 h or 24 h. The choice of the correct PSD model, slope parameters and fall speed in the optimal estimation snowfall retrieval, shows a good agreement with the observations at Haukeliseter for the 2016 Christmas storm in contrast to the 200 % difference when only using the CloudSat snowfall algorithm Section 2.4. It indicates also that the non-uniqueness of snow accumulation is reduced, when using a combination of ground-based observations instead of only Ze-S relationships. During the 2016 Christmas storm the average error for 24 h accumulation is almost similar to the best estimate at Barrow, Alaska. It turns out that there is no relation between high and low precipitation events since the differences vary. Cooper et al. [2017] also showed different combinations of PSD assumptions and snow fall speed. For Barrow, best agreements between observations and retrieved snowfall were found by using the



**Figure 4.2.1:** **a:** Surface precipitation amount comparison between the double fence observations and the retrieved surface accumulation of precipitation for 48 h. In black the linear correlation between the double fence observations and retrieved surface snow. **b:** Difference between the retrieved and the observed accumulation by the double fence. The colours represent the different starting days at 0 UTC for the 48 h accumulation.

CloudSat particle model, slope parameters and snowfall speeds from the MASC. In the here presented study, the best assumption for surface snowfall accumulation was found by using a particle model for rimed aggregates (Section 2.4 and 4.1) such as in Figure 4.1.1.

On 20 and 21 December 2016, the difference error is large ( $-97.8\%$  and  $435.8\%$ , respectively). This is probably related to an observation of precipitation at the double fence, even though no precipitation was observed. The double fence observation might be related to some particles stirred up by wind into the orifice of the gauge. Since no manual observations are done at the Haukeliseter site, is it difficult to say if blowing snow occurred and might introduce additional errors. But from the vertical MRR reflectivity it can be seen, that precipitation was not observed on before 21 December 2016 9 UTC. Even though it is assumed that the double fence is the absolute correct measurement it still underlies some uncertainties. A better way to asses the accuracy of the retrieved surface snowfall accumulation could be to compare the results to measurements inside a bush gage. A bush gauge is a precipitation gauge surrounded by a large bush to create artificial calm winds to increase the catch ratio of frozen precipitation and is considered

**Table 4.2.1:** Comparison of observed (obs.) and retrieved (ret.) snowfall amounts for the Christmas storm 2016. Difference refers to the difference of the retrieved and observed snow accumulation after 12 h and 24 h. The average difference is the value over all six/four days. Excluding values after 12 UTC on 25 December 2016 and after 17 UTC on 26 December 2016.

Day in 2016	12 h accumulation				24 h accumulation			
	Snowfall		Difference	Average difference	Snowfall		Difference	Average difference
	obs.	ret.			obs.	ret.		
	[mm]		[%]	[%]	[mm]		[%]	[%]
20 Dec	0.1	0.0	-97.8		0.1	0.0	-97.8	
21 Dec	0.7	3.8	+435.8	+85.5	17.1	16.6	-2.7	-4.7
22 Dec	13.6	13.2	-3.0		25.6	25.1	-2.1	
23 Dec	6.3	5.2	-16.8		23.3	19.8	-14.9	
24 Dec	14.7	13.4	-8.6		24.8	25.0	+0.8	
25 Dec	4.3	-	-		+15.4	-	-	
26 Dec	8.8	10.6	+20.1		25.1	-	-	

as the best available measurement for solid precipitation [Wolff, 2018]. Unfortunately there are only two bush gauges in the world, and because of local limitations a double fence construction is developed as reference for the Solid Precipitation Measurement intercomparison study during 1986 to 1993 [Goodison et al., 1998]. Comparisons between bush gauge and double fence precipitation measurements have shown, that for wind speeds up to  $9 \text{ m s}^{-1}$  outside the fence, the double fence will measure up to 10 % less precipitation. While wind speeds outside the double fence might reach  $20 \text{ m s}^{-1}$  show measurements inside a decrease to  $5 \text{ m s}^{-1}$ . Wolff [2018] believes the underestimation of the double fence will not be more than 20 % during frozen precipitation events with high wind speeds.

The low average difference value for 24 h accumulation, in Table 4.2.1 during the Christmas 2016 event (-4.7 %) follows a much lower average difference between retrieved and observed surface accumulation than at Barrow (36 %) and therefore a very good agreement between observed and retrieved snow accumulation during 21 to 24 December 2016.

In ??, the vertical SWC will be compared to the forecasted MEPS values for the 2016 Christmas storm. Despite the condition that the double fence measurement is influenced by wind will the small average difference for 21 to 24 December 2016 give confidence in the retrieved profiles of snow water content when comparing to the forecast, but it should be kept in mind that retrieved snow accumulation is underestimated and therefore may the vertical SWC be too low.

### 4.3 OBSERVATION AND PREDICTIONS OF LARGE SCALE WEATHER PHENOMENA AT THE SURFACE

**What is the goal of this section?** One of the main factors, that made the Christmas 2016 storm so interesting is the fact that fronts passed over Norway during the six-day period. One aim of this thesis is to identify if large scale phenomena were observed at the measurement site and if MEPS predicted the same measured pressure, temperature, wind, and precipitation patterns during the extreme event.

A comparison between the surface observations at Haukeliseter and the ECMWF analysis of the dynamic tropopause and geopotential thickness maps show that frontal transitions occurred on three days during the 2016 Christmas storm, 23, 25, and 26 December 2016 (Section 3.6). These show in the measurements and MEPS ensemble forecasts on 23, 25, and 26 December 2016 (Figure 4.3.1).

Figure 4.3.1 shows the different parameters forecasts initialised at 0 UTC for 23, 25, and 26 December 2016, as well as the observations at the Haukeliseter measurement site. Pressure decreases and increases, as well as temperature increases, and wind changes are present on 23 and 26 December 2016, since these changes show in the surface observations in Figure 4.3.1, it is assumed that frontal boundaries passed. The 25 December 2016 shows an increase of temperature between 15 UTC and 17 UTC leading to the assumption of a warm air evolution in Figure 4.3.1d. The overall weather situation, described in Section 3.6, showed that a warm front as well as cold front influenced Norway, on 25 December 2016. But since the pressure and wind does not indicate a change related to frontal conversion, it is assumed that only the warm air section between the frontal boundaries showed in the surface measurements at Haukeliseter.

As described in Section 3.6 the ECMWF dynamic tropopause analysis (Figure 3.6.3a) shows

more ridging at the DT level on 23 December 2016, than on the previous days. Warm air is advected closer over to Southern Norway Figure 3.6.3a. The low-pressure system approaches in the course of the day south-east of Iceland and hence stronger west to south west wind are associated with the cyclone (Figure 3.6.3c). The MEPS forecast, initialised on 23 December 2016 at 0 UTC in Figure 4.3.1a follows the observations and shows the decrease in pressure after 12 UTC due to the transition of the occluded front with a constant pressure after the transition. Since warmer air is more advected to the north and the DT in Figure 3.6.3a shows a warm low-pressure core, an increase in temperature is observed and predicted at the measurement site (Figure 4.3.1c). **Include L, H in the surface pressure images**

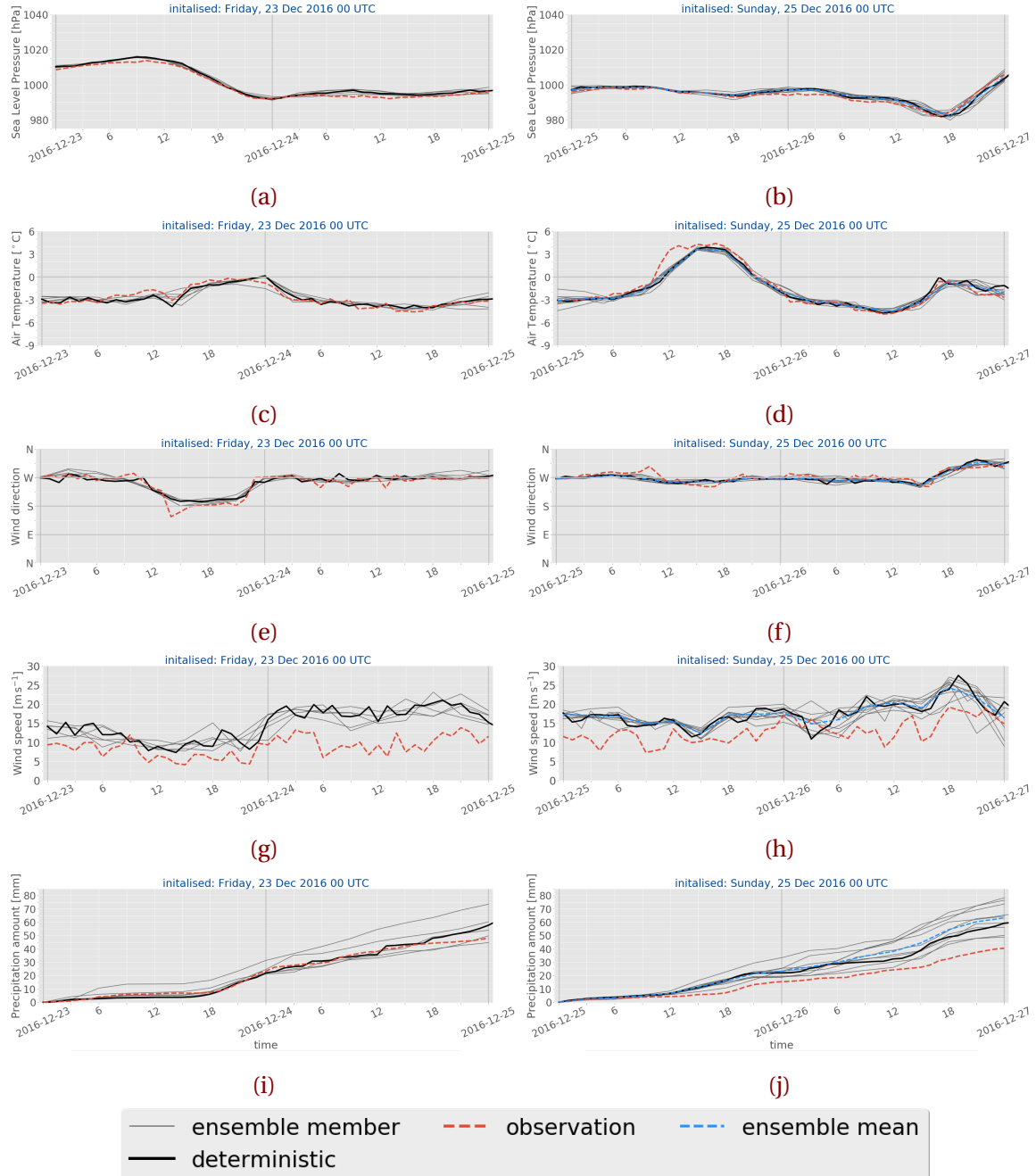


**Figure 4.3.1:** 48h surface observations and MEPS ensemble forecasts initialised on the 23 December 2016 at 0 UTC (left column, a, c, e, g, i), and on 25 December 2016 at 0 UTC (right column, b, d, f, h, j) as well as 26 December 2016 (k, l, m, n, o). Line representation according to the label. Upper to low panel: sea level pressure, 2 m air temperature, 10 m wind direction and speed, and precipitation amount.

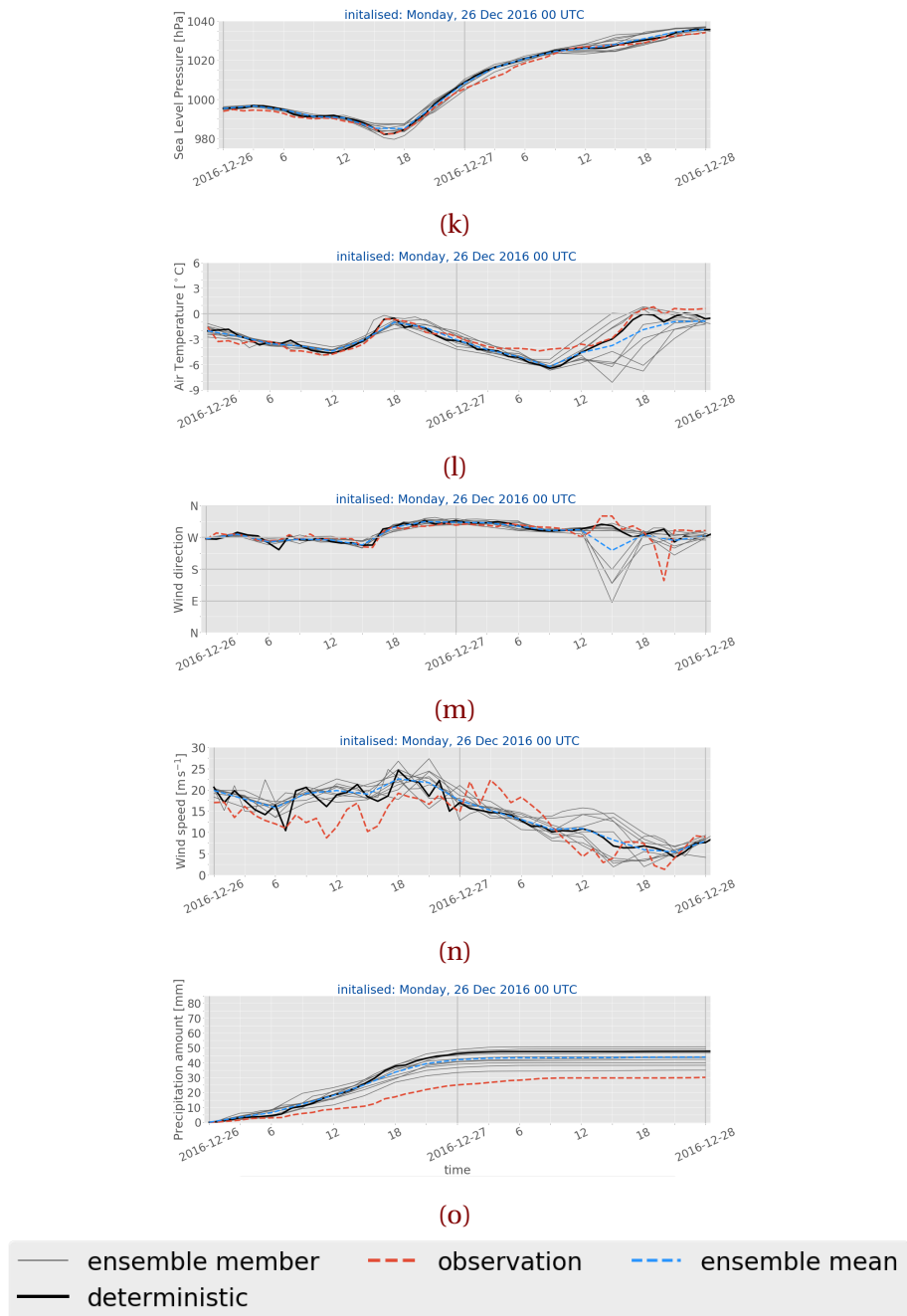


Figure 4.3.1: (Continued from previous page.)

As the cyclone is advected to the north-east, closer into the Norwegian Sea, a wind change can be seen in the analysis map from ECMWF (Figure 3.6.3c). First west wind and later

south-west wind was associated with the low-pressure system. The MEPS forecast and observations in Figure 4.3.1e and g indicate a wind change from west to south with a slight decrease in wind speed.

On 23 December 2016, the evolution of the occlusion is also observed by an increase in precipitation. Before 18 UTC the surface accumulation shows light precipitation (Figure 4.3.1i). During the transition of the occluded front, the observed surface accumulation increases which is associated to continuous, heavy precipitation, shown in Figure 4.3.1i.

Similar patterns as on 23 December 2016 were seen for the transition of the occluded front on 26 December 2016 in the ECMWF analysis Figure 3.6.6a and 3.6.6c. In this case the low-pressure system was located north of Morø and Romsdal in the Norwegian Sea. In the morning the cyclone is located east of Iceland and in the course of the day it moves closer to the coast of Norway. Before landfall at 16 UTC, a pressure decrease occurs (Figure 4.3.1k). During the development of the occluded front, the sea level pressure reaches its lowest point of 985 hPa and increases afterwards during the dissipation of the Christmas storm. Pressure, temperature, and wind changes for the occlusion transition were already forecasted for initialisations on 25 December 2016 (Figure 4.3.1b, d, f, h), only wind speed and precipitation seem not to agree with the observations at Haukeliseter.

**Kicki: see Discussion point?**

Since the cyclone was surrounded by colder air (south of the low-pressure system in Figure 3.6.6a), first a drop and then an increase of temperature were observed and forecasted by MEPS (Figure 4.3.1l). An indication of the occlusion evolution is also visible in the 10 m wind observations and forecasts. On 26 December 2016 at 0 UTC, the low pressure system is east of Iceland (not shown **Double check**), moving closer into the Norwegian Sea by 12 UTC (Figure 3.6.6a and 3.6.6c). Surface west winds are associated to the cyclone in the Norwegian Sea, and impinging on the West coast of Norway Figure 3.6.6c. The wind measurement and MEPS forecast in Figure 4.3.1m and 4.3.1n, show a gentle west breeze of up to  $17 \text{ ms}^{-1}$  at Haukeliseter before 12 UTC. The centre of the occluded front is located over Norway at 18 UTC, and the pronounced surface pressure gradient, in Figure 3.6.6d, indicate an increase in surface wind with a north-west wind direction. During this transition of the occlusion, the wind direction changes to north-west with higher observed wind speed up to  $20 \text{ ms}^{-1}$  (Figure 4.3.1m and

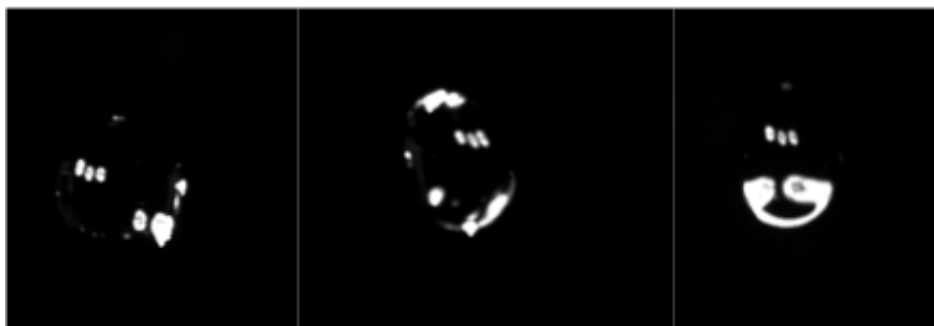


**Figure 4.3.2:** MASC images of falling water drops observed on 25 December 2016 at 17 UTC from three different angles. Not all parts of the liquid sphere are equally illuminated.

#### 4.3.1n).

Precipitation is continuing throughout the day, with light to moderate precipitation before the occlusion transition seen in Figure 4.3.1o. Heavy precipitation around 16 UTC is followed by moderate to light precipitation on 26 December 2016.

While on 23 and 26 December 2016 the precipitation was associated with a transition/landfall of an occluded front, the 25 December 2016 was marked by the transition of a warm sector. The ECMWF analysis shows a ridging at the dynamic tropopause (Figure 3.6.5a). The surface cyclone core is south east of Iceland in Figure 3.6.5a with two associated frontal boundaries. While the warm front is approaching the west coast, the cold front is north-west of Great Britain. In Figure 3.6.5c, the cold fronts tail moved into lower latitudes, following the slowdown of the cold front, leading to a stationary frontal boundary. Furthermore, the mid-latitude jet is aligned along the surface frontal boundaries (??), while the Haukeliseter site is located below the the midlatitudal jet (??). Neither pressure nor wind observations and forecasts indicate the evolution of any frontal boundary. The only indication of a transition could be seen in the increase of temperature at 11 UTC until 21 UTC (Figure 4.3.1d). In Figure 4.3.1f, a small wind change from west to north-west is observed by the wind mast at 10 UTC, which is not forecasted by MEPS, it rather estimated strong west winds.

In Figure 4.3.2, particle images taken by the MASC are available, during the transition of the warm sector. Without the images taken around 17 UTC it would only be possible to verify that liquid precipitation occurred with the optical precipitation detectors at the

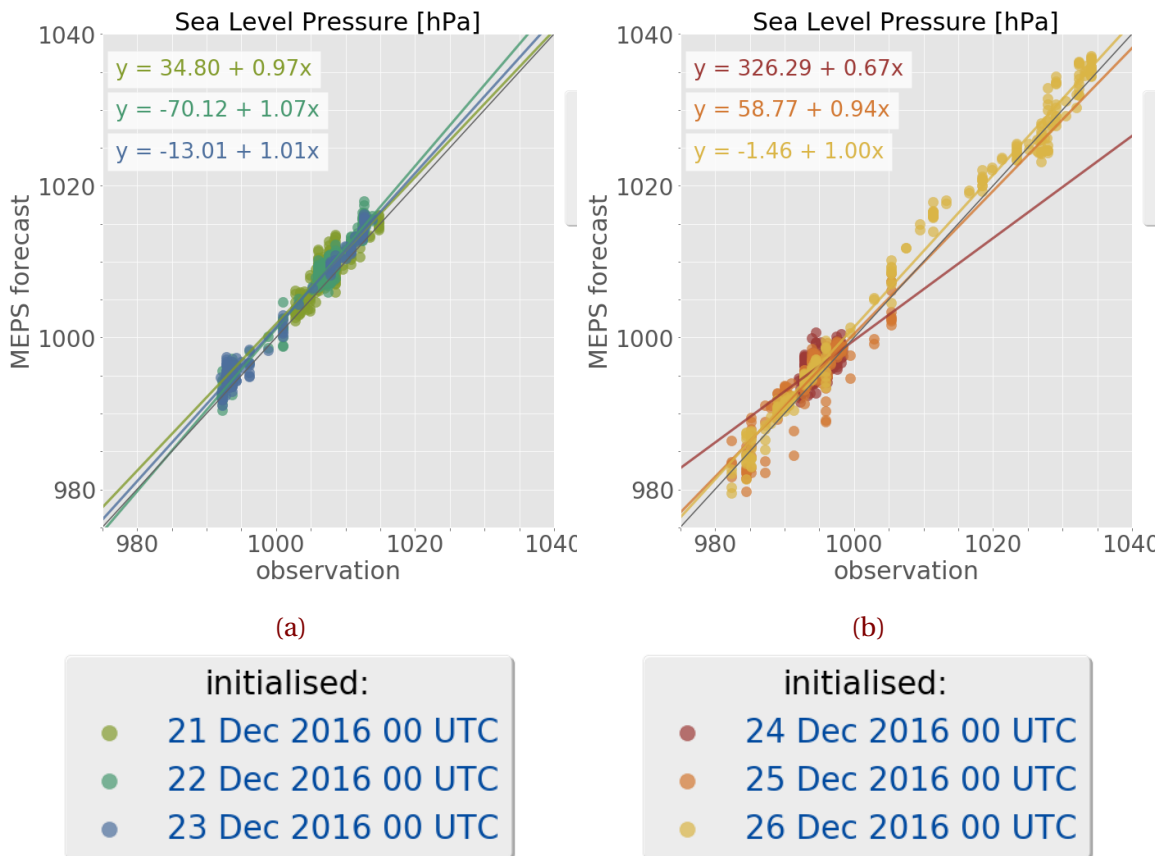


**Figure 4.3.3:** Sea level pressure [hPa] for 48 h for surface observations and ensemble forecasts initialised for 21 December 2016 to 23 December 2016 (left column, a, c, e, g, i) and for 24 ton 26 December 2016 (right column, b, d, f, h, j). The 48 h scatter values indicate each day, according to the colours.

Haukeliseter site. Together with the increase in surface temperature (Figure 4.3.1d) it can be concluded the warm sector of the Christmas 2016 event passed by the measurement site. **Should I include the DIANA analysis maps? But I dont know what the meteorologists are using to produce them? ECMWF?**

The comparison between the ECMWF analysis (Section 3.6) and the observations at the measurement site (Figure 4.3.1), that the ensemble member forecast system MEPS covers the prediction of large scale phenomena like occlusions and fronts, as well as liquid precipitation at the surface. Figure 4.3.3 presents the correlation between the observations

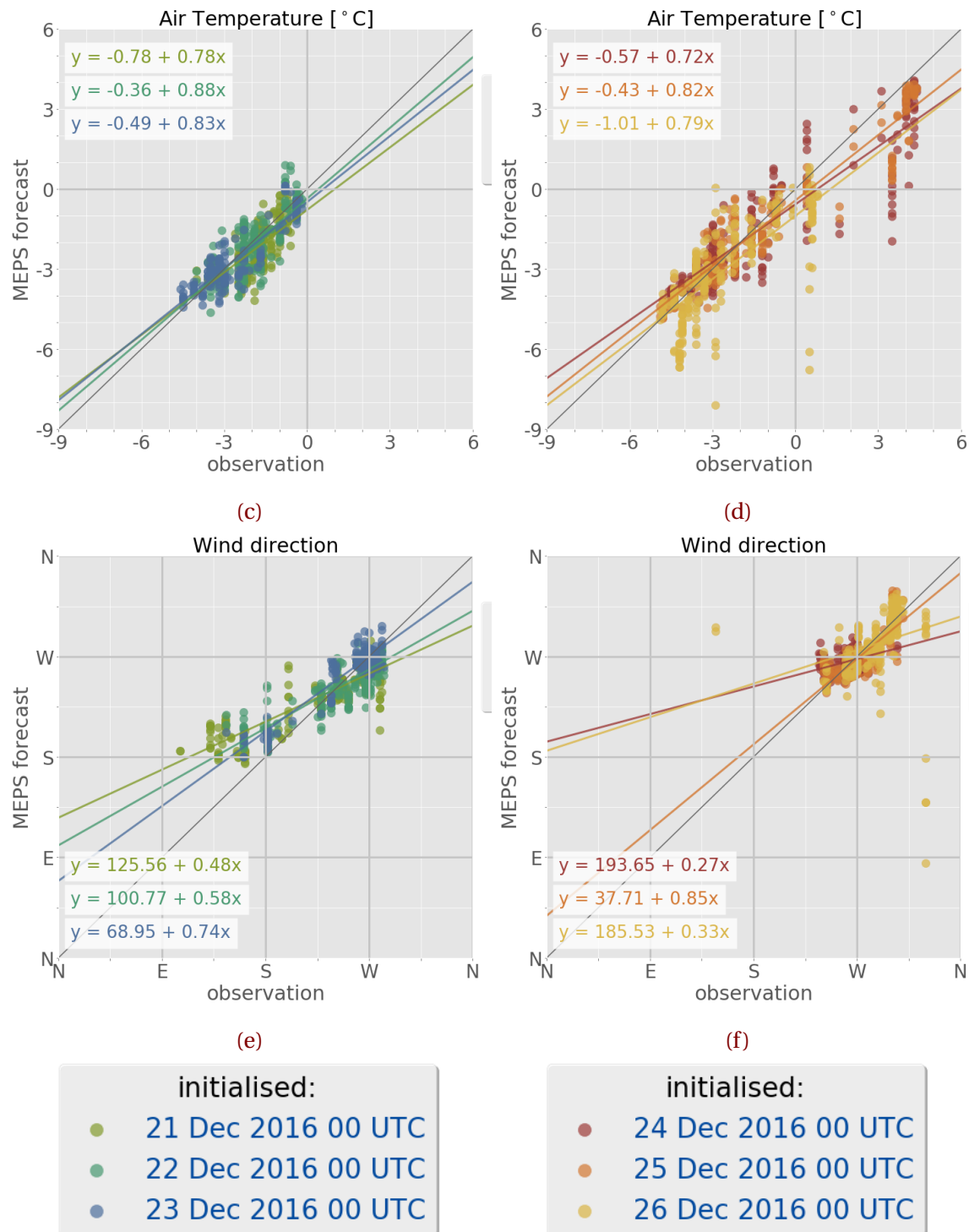
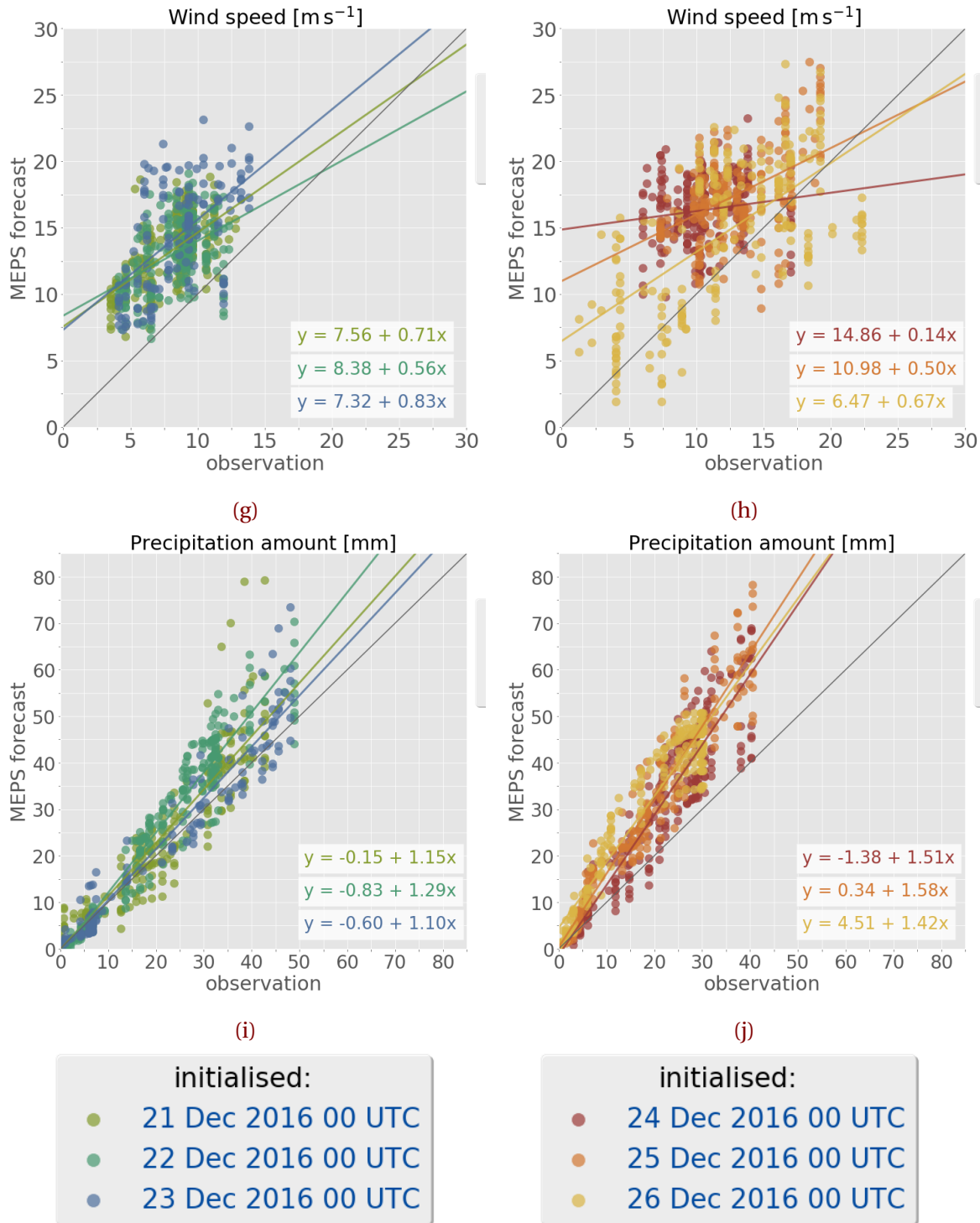


Figure 4.3.3: (Continued from previous page.) Upper panel 2 m air temperature, second panel 10 m wind direction.



**Figure 4.3.3:** (Continued from previous page.) Upper panel 10 m wind speed, lower panel surface precipitation amount.

and the 48 h MEPS ensemble forecast. The relation for Haukeliseter observations and the MEPS forecast members is indicated with the regression calculated for each day.

Sea level pressure has the best correlation under all variables. The best agreement is reached on 26 December 2016, when the Christmas storm hit land and dissipated after the evolution of the occlusion at 16 UTC. [Dahlgren \[2013\]](#) showed an improvement of sea level pressure forecast for AROME, by including large scale boundary conditions for ECMWF into the regional model. The observation-model comparison by [Dahlgren \[2013\]](#) showed an increase of forecast accuracy after 24 h with the use of pressure mixing. Since surface pressure is in good agreement with the observations, it is assumed that the warm front did not pass through Haukeliseter on 25 December 2016 and only the warm sector associated with the 2016 Christmas storm is observed. This shows a quite detailed forecast ability of MEPS, as from the ECMWF analysis, in Figure [3.6.5a](#), it is not quite clear if the warm front could have passed through. To be sure that the warm front did not pass through Haukeliseter, or whether it is a predictive error of MEPS, surface pressure, temperature and wind should be compared to the nearest grid point of the global forecast model ECMWF.

Figure [4.3.3d](#) displays a moderate correlation between observation and the 48 h MEPS ensemble member forecast system. In general, MEPS underestimates the observed 2 m air temperature, but MEPS estimated the surface temperature changes at the correct timing for 23, 25, and 26 December 2016. The previous operational deterministic forecast model AROME-MetCoOp showed a negative bias of 2 m temperature after winter 2013 with the introduction of AROME-Norway and later AROME-MetCoOp [[Müller et al., 2017](#)]. The mean error for the Norwegian model domain of AROME-MetCoOP estimated by [Müller et al. \[2017\]](#) is smaller than 1.8 K for the surface temperature in December 2014. In contrast, Figure [B.2.1c](#) shows warm and cold biases for 23 and 26 December 2016, respectively. On 25 December 2016, during the warm sector a negative bias was observed, underestimating the temperature when compared to the observation. The forecasts for 23, 25, and 26 December 2016 show calculated mean absolute error values ([??](#)) of up to 0.61 K, 0.77 K and 1.44 K in Figure [B.2.1](#). The new ensemble forecast system MEPS shows a reduction of mean errors for the Christmas 2016 extreme event.

During the Christmas storm 2016, high wind speeds were observed at the Haukeliseter site (Figure [4.3.3g](#) and [h](#)). According to [Müller et al. \[2017\]](#) large wind speeds are significantly better simulated for AROME-MetCoOp compared to ECMWF's forecast for the model

domain. The wind speed MEPS forecast in Figure 4.3.1g, h, and n displays still an overestimation of wind speeds. Furthermore, the correlation of observations and wind in Figure 4.3.3g and h show a high overestimation for stronger wind speeds on 24 to 26 December 2016 than for 21 to 23 December 2016. The inaccuracy for wind speeds is an already known difficulty in the deterministic version of MEPS [Müller et al., 2017]. Müller et al. [2017] presented, that AROME-MetCoOp wind speed prediction agreed better with observations for wind speeds between  $3 \text{ m s}^{-1}$  to  $13 \text{ m s}^{-1}$  than ECMWF forecasts did, showing the advantage of a high-resolution weather model. Furthermore, with increasing wind speed the forecast accuracy for the Norwegian mean decreases with a mean absolute error below  $2 \text{ m s}^{-1}$  for December 2014 in AROME-MetCoOp. The mean absolute error for wind speed during the Christmas storm is higher for all days ranging from  $3 \text{ m s}^{-1}$  to  $7 \text{ m s}^{-1}$ . During the three days with frontal transitions, the highest mean absolute error of  $6.5 \text{ m s}^{-1}$  occurs during 23 December 2016. More than three times as high as the monthly averaged value for the Norwegian forecast domain from Müller et al. [2017]. Their study case for February 2015 showed a slight overestimation of ECMWF 10 m wind compared to the Norwegian AROME-MetCoOp forecast, but still overestimates MEPS the wind. What could be still a weakness that the model overestimates the wind speed? In Müller et al. [2017]: change from ECOCLIMAP1 because the surface roughness was too low and followed high wind speeds? Is this still the case for MEPS? High wind speeds followed also from wrongly addressed 'permanent snow'. Do not use 'orographic drag' in AROME-MetCoOp, could that lead to the too high estimated wind? When 'canopy drag' was changed saw increase in SBL drag which followed a decrease in wind speed. But AROME-MetCoOp is able to forecast high wind speeds, while ECMWF is not.

Haukeliseter is a measurement site exposed to high wind speeds [Wolff et al., 2013, 2015]. The ensemble prediction system MEPS still seems to have issues forecasting the wind speed correctly in mountainous terrain. A detailed insight to the orographical wind influence will be assessed in Section 4.6.

Figure 4.3.1i, j, and o illustrates the surface precipitation amount observed and predicted by MEPS for Haukeliseter. MEPS overestimation is shown for precipitation when the cyclone intensifies and gets closer to Norway on 25 and 26 December 2016. The surface observations and MEPS predictions in Figure 4.3.3i and j also show an overestimate for 25 and 26 December 2016, whereas on 23 December 2016 the surface

accumulation is balanced for predictions up to 30 mm. Any reasons for the overestimation of precipitation accumulation on the ground will be further analysed and discussed in Section 4.4.

Overall, the forecast is best for all variables for initialisations on 23 December 2016 (Figure 4.3.3a, c, e, g). The large-scale weather pattern seems to be more predictable on 23 December 2016 than initialisations on 25 and 26 December 2016. Figure 4.3.3b, d, f, h suggest as if MEPS has difficulties predicting the intensification and associated pressure drop of the Christmas 2016 storm at Haukeliseter. The prediction of pressure fits well on all three days (Figure 4.3.3a, b) compared to temperature, wind direction, wind speed, and precipitation (Figures 4.3.3c to 4.3.3j). The greatest difficulty has MEPS with the prediction of wind speed during the entire extreme event. The rainfall, however, fit well for 23 December 2016 (Figure 4.3.1i and 4.3.3i), but MEPS has problems predicting the accumulation of surface precipitation amount correctly for the last days of the 2016 Christmas storm, 24 to 26 December 2016 (Figure 4.3.1j, o and Figure 4.3.3j).

What is the difference between MESP and MetCoOp? What do we want to assess with perturbed ensemble members?

Overall conclusion: Which day was presented worst/best and relate to large scale synoptics

## 4.4 SURFACE SNOWFALL ACCUMULATION

One approach of this study is to see if observed surface accumulation was correctly predicted by the regional weather model MEPS. Precipitation amount at the surface are shown in Figure 4.4.1. The figures are representing the observed and forecasted surface precipitation accumulation in mm over 48 h. Accumulation, measured by the double fence are presented as red hexagons. Minutely retrieved surface snowfall amount in dash-dotted green. The ten 48 h forecast ensemble members are lines in black and grey, the deterministic and its perturbed ensemble members, respectively. The blue dashed line shows the ensemble mean of all ten members. Since the deterministic and the first ensemble member are having values every hour and the other perturbed members only every three hours, shows the ensemble mean the precipitation amount at 0 h, 3 h, ...,

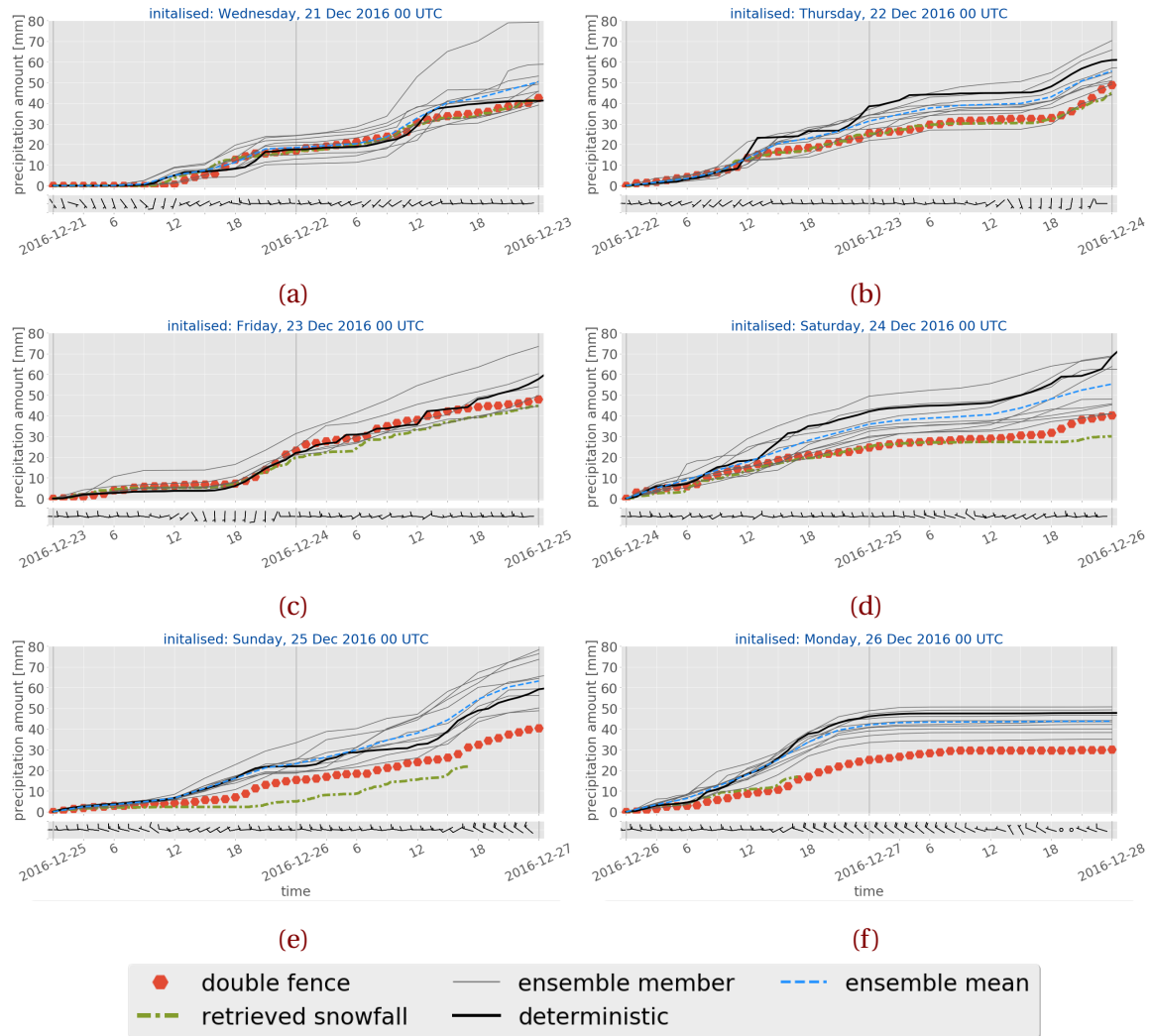


**Figure 4.4.1:** 48 h surface snowfall accumulation for 21 to 26 December 2016 (a-f). Representing the values from the double fence in red, hexagons; optimal estimation retrieval output at snow layer height 400 m in dash-dotted green; and ensemble member deterministic forecast, initialised at 0 UTC in black and its nine perturbed ensemble members in grey. The ensemble mean of all ten members is shown in dashed blue. Underneath are the associated last hour 10 min average wind from the weather mast at 10 m height.

21 h, 24 h, ..., 48 h forecast time. When too few ensemble members were present, like on 23 December 2016, no ensemble mean is calculated (Figure 4.4.1c). Underneath is the associated 10 min average wind of the last hour from the 10 m weather mast at

Haukeliseter, to see if surface accumulation observations may be influenced by wind. Figures 4.4.1a to 4.4.1c show in general a better agreement between observations and forecast for 48 h forecasts initialised on 21 to 23 December 2016 at 0 UTC. The spread of the ensemble members around the control run fit better to the observations as well than initialisations on 24 to 26 December 2016. During these days intensifies the low-pressure system and gets closer advected to the Norwegian coast and influencing the local weather in Norway (Chapter 3). Figures 4.4.1d to 4.4.1f indicates a larger estimated surface precipitation amount for all ten ensemble members than observed at the measurement site between 24 to 26 December 2016.

The correlation between double fence observation and ensemble forecast is presented in Figure 4.3.3a and b. Showing a better agreement between 21 to 23 December 2016 than initialisation on 24 to 26 December 2016. On 21 to 23 December 2016 is the slope of the regression relatively close to unity, indicating a good agreement between the ensemble forecast and the observations by the double fence. The largest disagreement between surface observations and forecasts is seen on 25 December 2016 with a positive bias up to 17 mm (Figure B.2.1i). The mean absolute error is not larger than 13 mm for the first three days and increases with intensification of the storm up to 19 mm on 24 December 2016. Initialisations on 24 December 2016 indicate an overestimation of the deterministic surface snowfall prediction already after 13 h forecast time. The deterministic forecast in solid black is much higher and increases faster than the observations. In Figure 4.4.1d at 16 UTC a higher value of approximately 15 mm can be seen when compared to the surface measurements. This difference remains almost constantly over the forecast time. Furthermore, all ensemble members seem to overestimate the surface accumulation after 24 h prediction time.

Since the MEPS performance was better on the previous days one might assume that the double fence measurement is influenced by surface winds. It shows in Figure 4.4.1d that the 10 min average wind at 13 UTC increases from  $5 \text{ ms}^{-1}$  to  $10 \text{ ms}^{-1}$  (see also Figure B.1.1n). Wolff [2018] states that the double fence gauge is influenced by wind, but accumulation measurement errors occur rather at higher wind speeds larger than  $20 \text{ ms}^{-1}$ . It is therefore assumed that the measurements from the double fence are correct and MEPS had rather a forecasting issue.

While the cyclone gets more advected to Norway increases the forecast inaccuracy of

the surface precipitation. On 25 December 2016 the miscalculation of the precipitation amount is associated with the warm sector evolution at Haukeliseter (Section 4.3). Afterwards follows the model the same path as the double fence observations, but higher. The 25 December 2016 indicates a good spread between the ensemble members and the deterministic forecast, while on 24 December 2016 the ensemble members were not spread symmetrically around the deterministic forecast.

An overestimation of the surface accumulation is also observed on 26 December 2016. While the large-scale analysis indicates the development of an occlusion after 15 UTC (Figure 3.6.6a, 3.6.6c) seems the overestimation to occur after 12 h forecast time in Figure 4.4.1f. Again, all ensemble members seem to follow the course of the double fence accumulation, but larger.

Whereas the spread between the ensemble members is large in the beginning of 24 December 2016 is the variability between the members narrow for 25 and 26 December 2016. The variability between the ensemble member can be compared with a box-whisker plot. A box-whisker-plot shows the time evolution of the distribution of the precipitation amount made of ten ensemble members up to 48 h. Since some ensemble member do not have forecast values every hour provides the box-whisker-plot in Figure 4.4.2 information every 3 h. The red line shows the ensemble mean of all ten members and shows if the distribution is skewed. The short light green horizontal line is showing the median, wide vertical box represents the 25th and 75th percentiles, and minimum and maximum values are indicated by the vertical lines, whiskers.

The box-whisker-plot in Figure 4.4.2 shows the distribution of the ten ensemble members for the respective days. All three days with overestimation seem to be different in their variability. As expected increases the forecast uncertainty with longer forecast time for precipitation amount.

Figure 4.4.2b shows for 25 December 2016 the least variability between the ten ensemble members of up to almost 24 h. The 25 December 2016 is also the forecast with the smallest positive bias of these three days. As Figure 4.3.3j suggests is the overestimation not as high as for 24 and 25 December 2016. On 24 and 25 December 2016 is the mean error for the surface accumulation largest with values up to 19 mm.

Larger variability is already present after 3 h prediction time in Figure 4.4.2a on 24 December 2016. The spread between the ensemble members (shown by the minimum

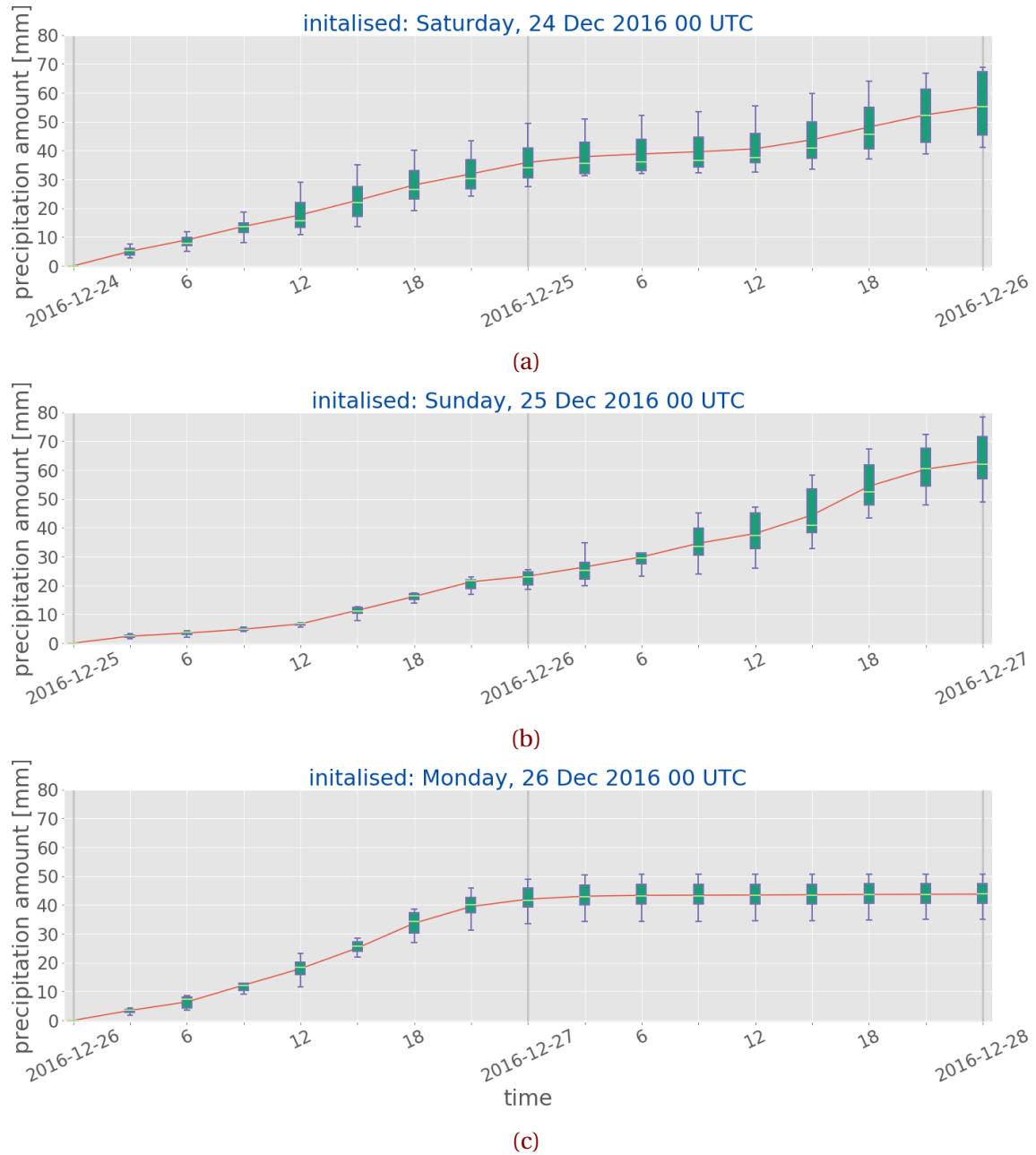


**Figure 4.4.2:** Box-whisker-plot of the ten ensemble members of MEPS. Red line indicating the ensemble mean, lower and upper whisker the 25th and 75th percentile, respectively. Light green shows the median of all members and the box represents the middle 50 % of scores of the precipitation.

and maximum whiskers) seems to be wide indicating a larger uncertainty about the amount of surface accumulation. The ensemble mean (red line) is always higher than the median and already after 12 h forecast time is the median closer to the lower 25th percentile. Also, all upper whiskers in Figure 4.4.2a are taller than the lower ones, which would follow that the ensemble members vary amongst the most positive quartile and that it is very similar for the least positive quartile group. Since the deterministic forecast, black line in Figure 4.4.1d, is in the upper percentile compared to its perturbed members it follows that for this forecast the deterministic forecast was not the best guess for the surface accumulation and by using the 'wrong' initial state it can have led to larger miscalculations.

I believe that the uncertainty appearing already after 3 h could be associated with a too long spin-up time of MEPS. MEPS usually has a spin-up time of about three hours, on 24 December 2016 this might have been longer as a result of poorer initial conditions [Need a reference here, not stated in Müller et al. \[2017\]](#). The regional model MEPS receives initial and boundary conditions from ECMWF before it can produce forecasts [[Müller et al., 2017](#)]. Since initial conditions such as observations have uncertainties as well as the model has mistrust, and the own climatology needs to be approached, a model has to stabilize before the simulations can be trusted. The spin-up time varies depending on the quality of the initial and boundary conditions. Apparently, it seems, that the initial and boundary conditions for MEPS were not perfect for initialisations on 24 December 2016 at 0 UTC. The deterministic and perturbed members seem not to have stabilised yet and show larger variability in ?? from early on.

The uncertainty might have also been related to the fact, that the large-scale situation got more complex. The precipitation amount associated with the transition of an occluded front on 23 December 2016 was higher than on the previous days (Figure 4.3.1i and Figure 3.5.1). On previous days was the hourly precipitation around 0 UTC less intense than on 23 December 2016. This led to a higher accumulation amount over shorter time and could have followed a larger variability in the forecast model. Another possibility is perhaps that MEPS might have accounted for additional precipitation around 12 UTC on 24 December 2016 and this showed a stronger increase in accretion in Figure 4.4.1d at 13 UTC. I believe it could be associated to a local resolution effect of MEPS. Figure 2.5.1 shows the MEPS resolution and its 2.5 km grid cells around the Haukeliseter site. The complex terrain represented in the model could have followed a local misplacement of a

precipitation cell by a few kilometres and followed an estimation of more accumulation at the site after noon.

Figure 4.4.2b and c show a smaller ensemble member variability on 25 December 2016 and 26 December 2016 than on 24 December 2016. The box-whiskers are narrower for the first 30 h in Figure 4.4.2b, but slightly larger after 6 h forecast time for initialisations on 26 December 2016. Section 4.3 presented a good agreement between observations and forecast of large scale features in terms of pressure, temperature and wind direction. While the occlusion on 26 December 2016 was more intuitive (Figures 4.3.1k to 4.3.1n) than the warm front development on 25 December 2016 (Figure 4.3.1b, d, f, h) shows the mean error for each variable to be best for 25 December 2016 (Figure B.2.1b,d,f, h, and j). On 25 December 2016 the overestimation started to occur around 13 UTC in Figure 4.4.1e, related to the delayed forecasted temperature increase in Figure 4.3.1d. As ?? shows, increases the variability in the forecast after 15 h prediction time. In general, agree median and mean well for the entire period of a 48 h forecast. After 39 h prediction time is the mean much higher than the median and closer to the lower 25th percentile in ???. It seems, that all ten ensemble members agree well on the prediction and nevertheless overestimates MEPS the surface accumulation. I consider that MEPS misinterpreted the amount of precipitation related to the transition of the warm sector.

During 26 December 2016 the core of the low-pressure system goes through between 15 UTC and 18 UTC at Haukeliseter. The box-whiskers in Figure 4.4.2c indicates a larger variability after 6 h prediction while the precipitation amount forecast is miscalculated at 12 UTC and following the structure of the double fence observation. Variability of all ensemble members show to increase at 6 h forecast time, but then decreases again in Figure 4.4.2c.

Since the box-whisker-plot in Figure 4.4.2b and c show less variability in the beginning it is assumed that spin-up time issues are less likely. It could be related to an error in the initialisation state, even though it does not show in the variability in the beginning. An error associated with the spin-up time of MEPS is not totally excluded for these days. In Figure 4.4.1e and f agrees the ensemble mean well with the deterministic forecast, which is an indication of a symmetrical spread around the deterministic run.

The overestimation during 24 and 26 December 2016 might be related to the high forecasted wind speeds, as well as to the complex development of the low-pressure system

north-west of Norway on 24 December 2016.

**Table 4.4.1:** make new as previous tables Surface snowfall accumulation measured by the double fence gauge. Presenting 12 h accumulation before noon and after noon, as well as the total 24 h surface accretion.

<b>Day</b>	<b>Accumulation</b>		
	[mm]		
	12 h (0 to 12 UTC)	12 h (12 to 23 UTC)	24 h
21 December 2016	0.7	16.4	17.1
22 December 2016	13.6	12.0	25.6
23 December 2016	6.3	17.0	23.3
24 December 2016	14.7	10.1	24.8
25 December 2016	4.3	11.1	15.4
26 December 2016	8.8	16.3	25.1

According to Müller et al. [2017] are strong precipitation events better predicted with AROME-MetCoOp than with ECMWF (European Centre for Medium-Range Weather Forecasts). In Section 2.2 it was described, that during 21 to 27 December 2016 56.9 % of the total December 2016 accumulation were observed. Müller et al. [2017] states also, that an overestimation appears, where the precipitation event (12 h accumulation) is less than 10 mm this seems not to be true for all days but could be possible for 25 and 26 December 2016 (observed accumulation in Table 4.4.1). In December 2014 was the 12 h precipitation mean absolute error in AROME-MetCoOp with 1.5 mm. For the Christmas storm is the mean absolute error not larger than 5 mm for the first 12 h accumulation on 24 and 26 December 2016 (Figure B.2.1l). Therefore, the assumption follows that on 26 December 2016 the overestimation might be correlated to the <10 mm problem described by Müller et al. [2017]. The 12 h accumulation is presented in Table 4.4.1 for Haukeliseter and shows that 12 h accretion was less than 10 mm for 25 and 26 December 2016. On 25 December 2016 the mean absolute error was 1.1 mm for the first 12 h accumulation and shows that this could be an influence but does not necessarily mean to be the case, since the overestimation started to occur after 11 h prediction time.

It will be interesting to re-run the ensemble prediction system again with all available observations to see, if this has an influence on the overestimation indicated in Figures 4.4.1d to 4.4.1f. ECMWF as boundary condition might not have reached its stabilised state itself when MEPS was initiated and could also have led to a misinterpretation of surface accumulation. A re-run with analysis data from ECMWF could possibly improve the original forecast [find reference for this](#). Another approach could be to perturb the initial state (deterministic forecast) in other way, to see if different perturbations might lead to a better correlation between observation and forecast at the ground than presented in [??](#). Also, the deterministic forecast (best guess) might have been chosen incorrectly and followed a miscalculation of surface accumulation, since the misinterpreted best guess was perturbed. It is very important to have correct measurements such as the double fence or MRR observations, to produce better initial condition for weather forecast models, so that initialisations can start at a realistic state.

Also, more study cases should be considered to get a better estimate about the performance of MEPS during extreme winter events. The mean absolute error for 12 h accumulation has shown a great variability, depending on the initialisation time and the intensification of the low-pressure system.

## 4.5 OBSERVATION OF LARGE SCALE WEATHER PHENOMENA IN THE VERTICAL

Frontal boundary passages were observed at the surface several times throughout the extreme storm in December 2016. MEPS is able to predict the large scale features and related surface changes for initialisation more than 24 h before (Section 4.3). In winter 2016 three additional instruments were installed to estimate the vertical snow water content at Haukeliseter. This unique approach gives the opportunity to compare the vertical forecasts of SWC to vertical solid precipitation observations. As far as the author knows is there no study on this particular topic about the verification of vertical ensemble member prediction models with observations.

Figure 4.5.1 shows the reflectivity from the MRR at Haukeliseter for 23 December 2016, 25 December 2016 and 26 December 2016. Passages of occluded fronts and a warm

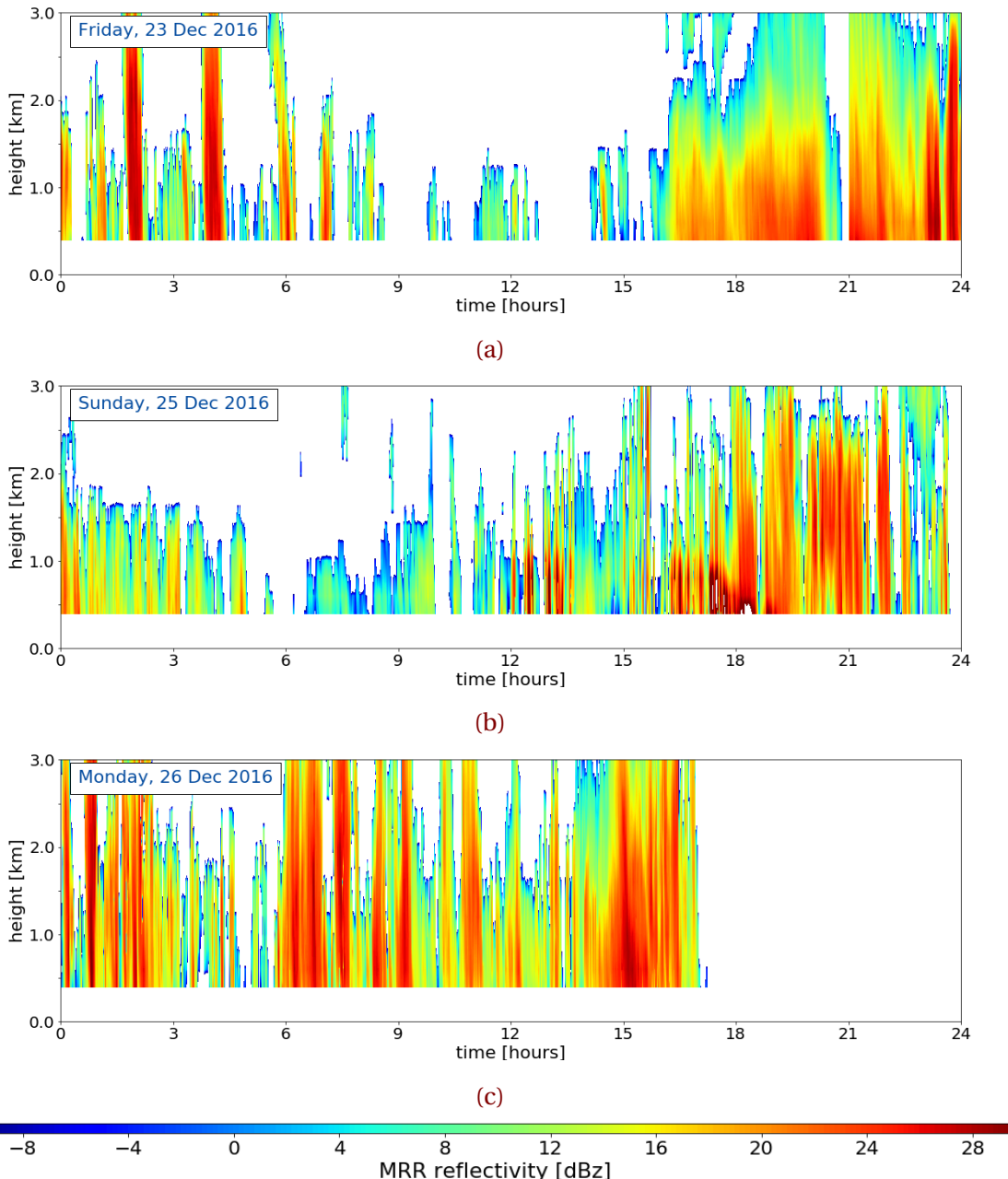


**Figure 4.5.1:** MRR reflectivity for the days when a front or an occlusion passed through at Haukeliseter. dBZ reflectivity according to the colour bar, with weaker precipitation in blue and more intense precipitation in red. **a:** Friday, 23 December 2016, **b:** Sunday, 25 December 2016, and **c:** Monday, 26 December 2016.

sector were observed on 23 December 2016, 26 December 2016 and 25 December 2016, respectively. Figure 4.5.1c presents only values until 17 UTC, because of the temperature change and hence a precipitation shift followed liquid drops freezing on the MRR dish and the signal got attenuated.

The transit of the boundary is shown in Figure 4.5.1 by the more consistent structure of a storm with higher reflectivity values. While on 23 December 2016 and 26 December 2016 the reflectivity did not pass values larger than 28 dBZ shows Figure 4.5.1b high reflectivity values larger than 30 dBZ (compare for approximation Table 2.3.1). These high values indicate the observation of possible liquid precipitation. Images from the MASC were able to verify observed liquid drops during 12 UTC to 21 UTC (Figure 4.3.2).

On 23 December 2016 allow the surface observations to assume that the occluded front passed through between 12 UTC to 21 UTC (Figure 4.3.1a, c, e). The vertical observations at Haukeliseter show intense reflectivity and therefore more intense precipitation after 16 UTC (Figure 4.5.1a). Another occlusion passed through on 26 December 2016 shortly before 15 UTC which lasted until 21 UTC indicated by a more consistent storm structure in Figure 4.5.1c around 15 UTC. The high reflectivity on both days shows the passage of the occlusion and the associated precipitation. The wind on 23 December 2016 was from the south, upslope (Figure 4.3.1e, Figure 2.1.1c) which led to a more consistent storm structure. On 25 December 2016 indicate Figure 4.3.1f and h strong wind observations from the west which led to a consistent, but shorter storm structure in Figure 4.5.1b at 15 UTC. The orographic influenced wind and therefore a possible relation to the precipitation will be further assessed in Section 4.6.

?? presents the reflectivity from the MRR and the snow water content retrieved from the reflectivity as well as the 48 h forecast values. Minutely MRR reflectivity and retrieved snow water content can be seen in Figure 4.5.2a, d, g, and j. Figure 4.5.2b, e, h, k show in the upper panel the hourly averaged values from the retrieved SWC and in the lower panel the ensemble mean of the instantaneous forecast values every hour over all ensemble member. Three hourly averaged retrieved values are then presented in the upper panel of Figure 4.5.2c, f, i, and l, the lower panel are the ensemble mean forecast values every three hours.

Figure 4.5.2e (lower panel) shows the one hourly averaged forecast values over all ensemble members, neglecting not existing values. Initialisations less than 24 h before the

event predict the consistent retrieved snowfall after 16 UTC (Figure 4.5.2d, lower panel and Figure 4.5.2e, upper panel). Even the three hourly averaged forecast values show a response on the occurrence of the storm (Figure 4.5.2f, lower panel). The duration of the passage is between 16 UTC to 23 UTC because of the longer time span is the prediction system able to estimate the snow water content. Forecasts initialised 48 h prior predict also the consistent storm structure and therefore the passage of the front (Figure 4.5.2b, c). In general, is the forecasted instantaneous snow water content amount weaker than the retrieved values for predictions on 23 December 2016. Hourly averages, only using the deterministic forecast and the first ensemble member show no occurrence of the occlusion passage on either day (Figure B.3.1a, b, c, d). The variation of each ensemble member initialised on the respective day are given in Figure B.4.1. In Figure B.4.1b is the prediction for the occlusion passage quite weak.

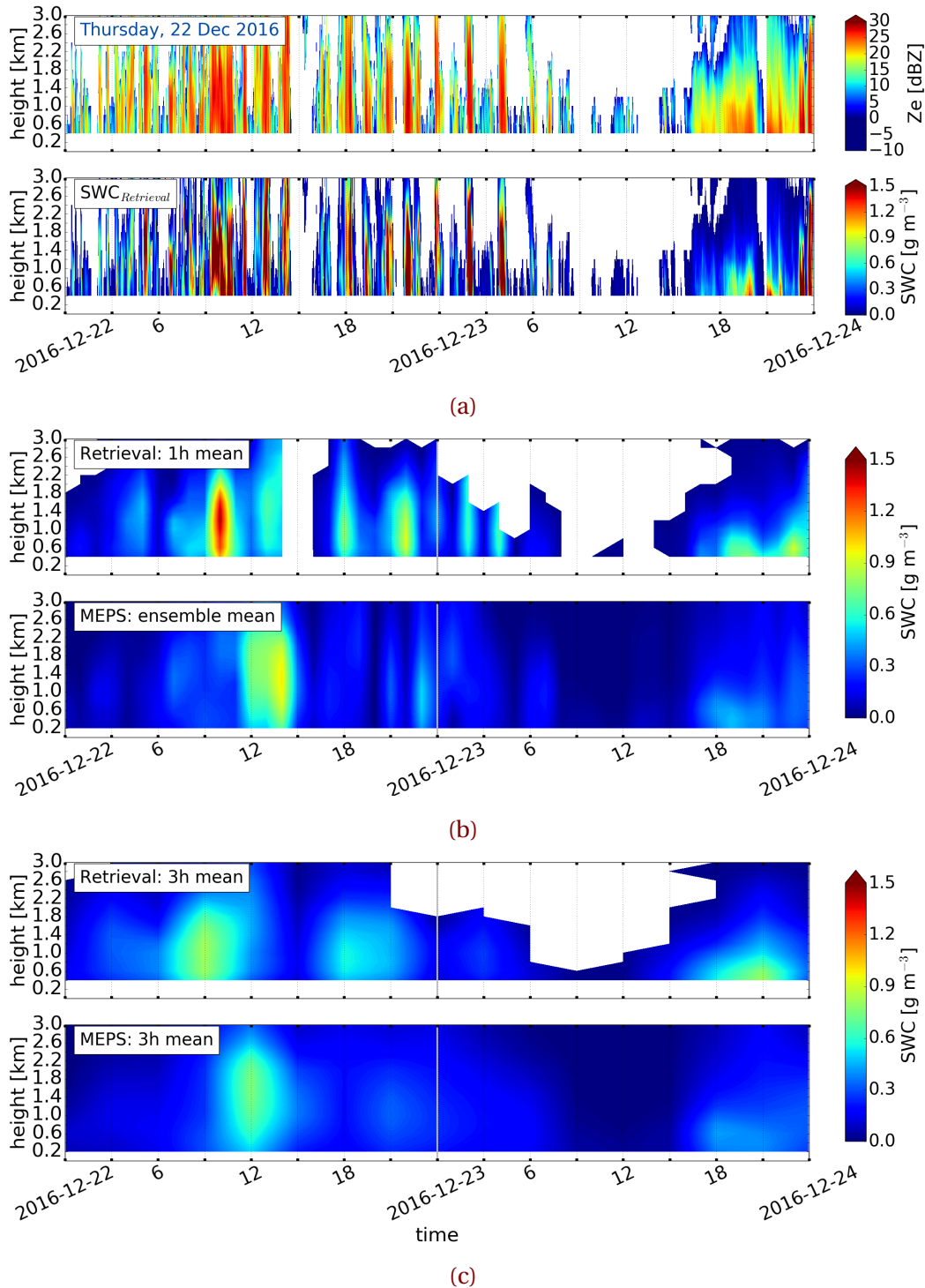


**Figure 4.5.2:** Initialisation 22 December 2016, 23 December 2016, 25 December 2016 and 26 December 2016 0 UTC. (a, d, g, j) Upper panel: MRR reflectivity for 48 h, lower panel minutely retrieved SWC. (b, e, h, k) Upper panel: hourly averaged retrieved SWC, lower panel instantaneous hourly averaged forecast of all ensemble member SWC, neglecting missing values. (c, f, i, l) Upper panel three hourly averaged retrieved SWC, lower panel instantaneous three hourly averaged forecast of all ensemble member SWC.

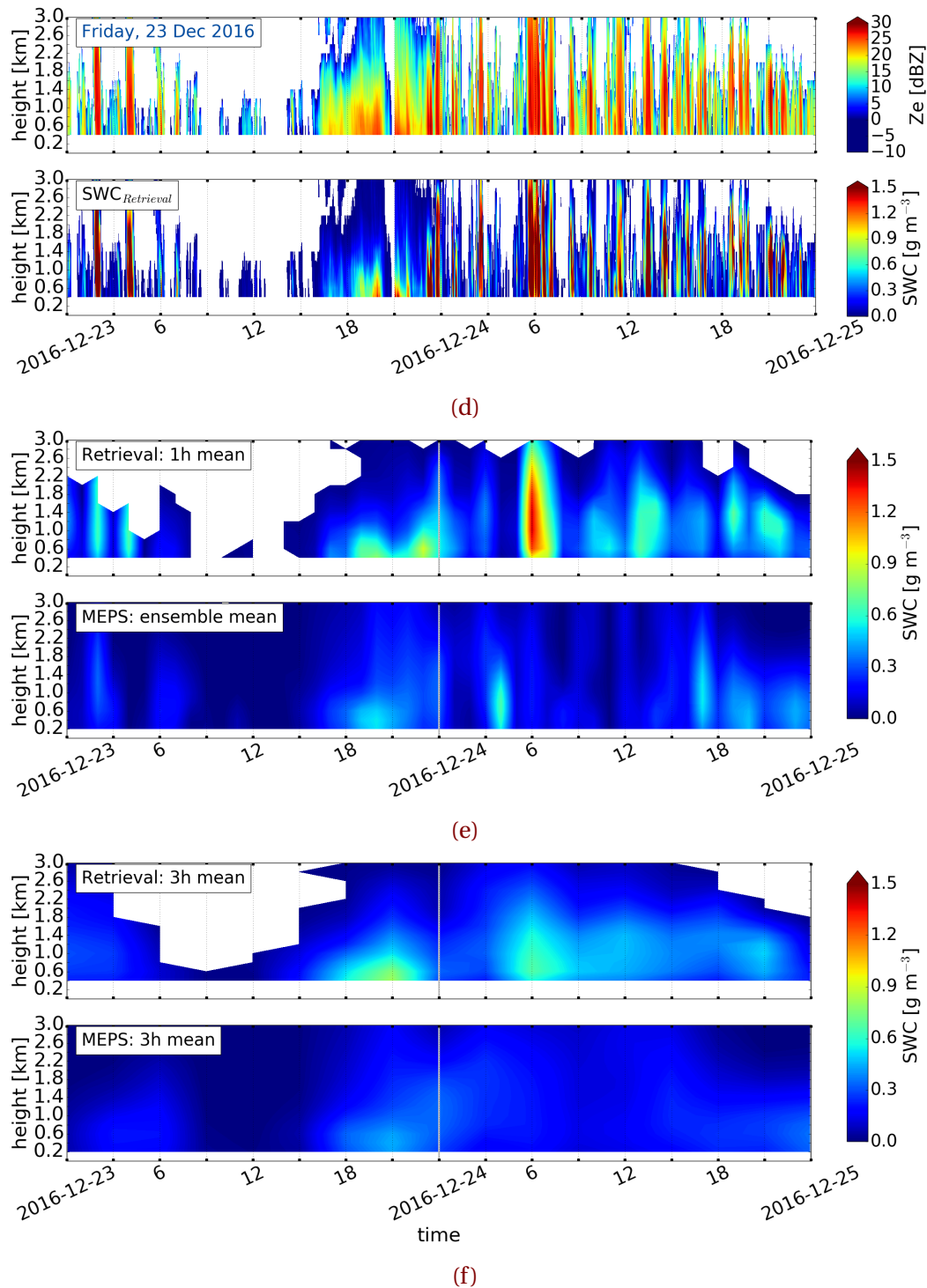


Figure 4.5.2: (Continued from previous page.) Initialisation 23 December 2016.

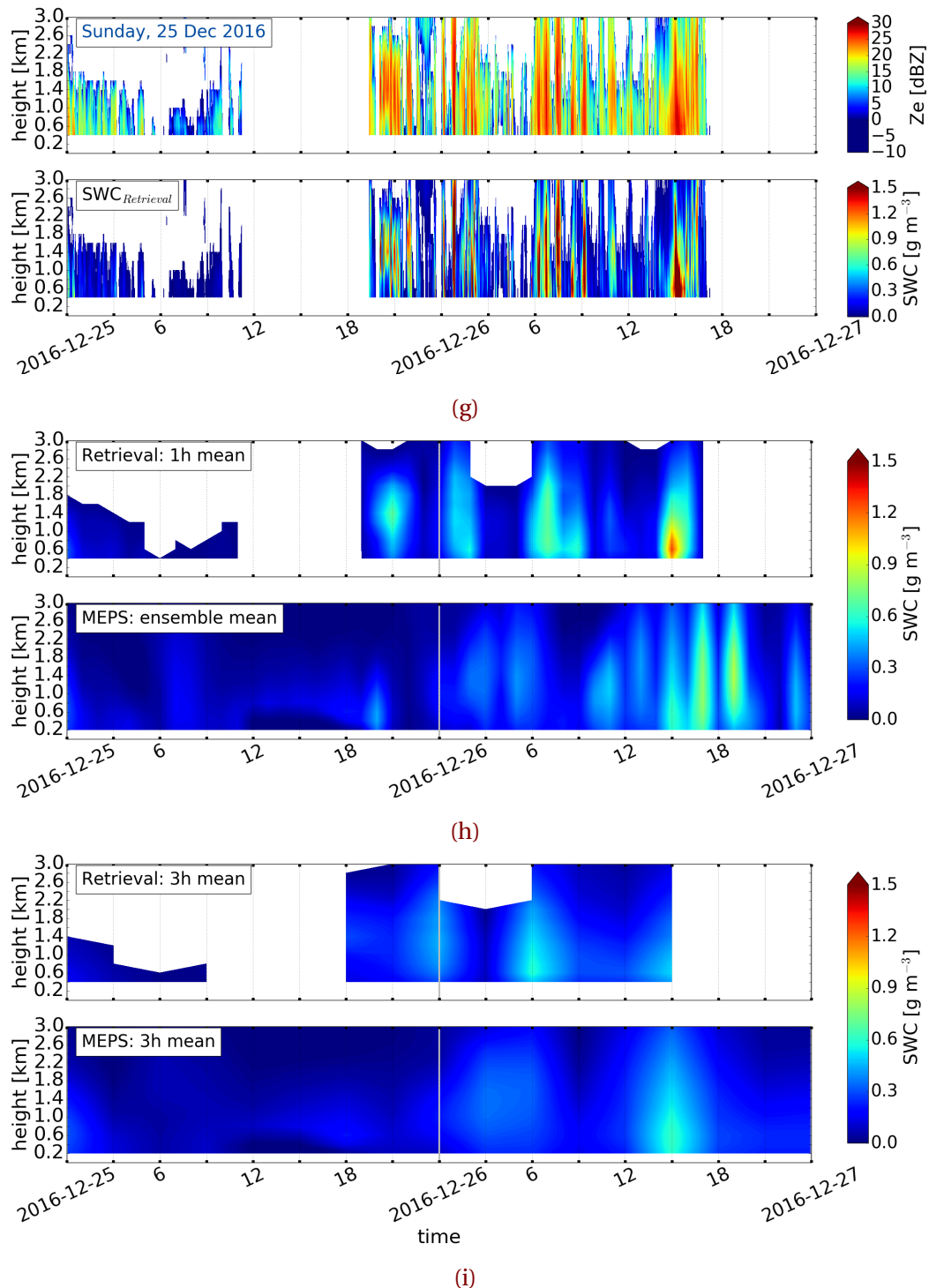
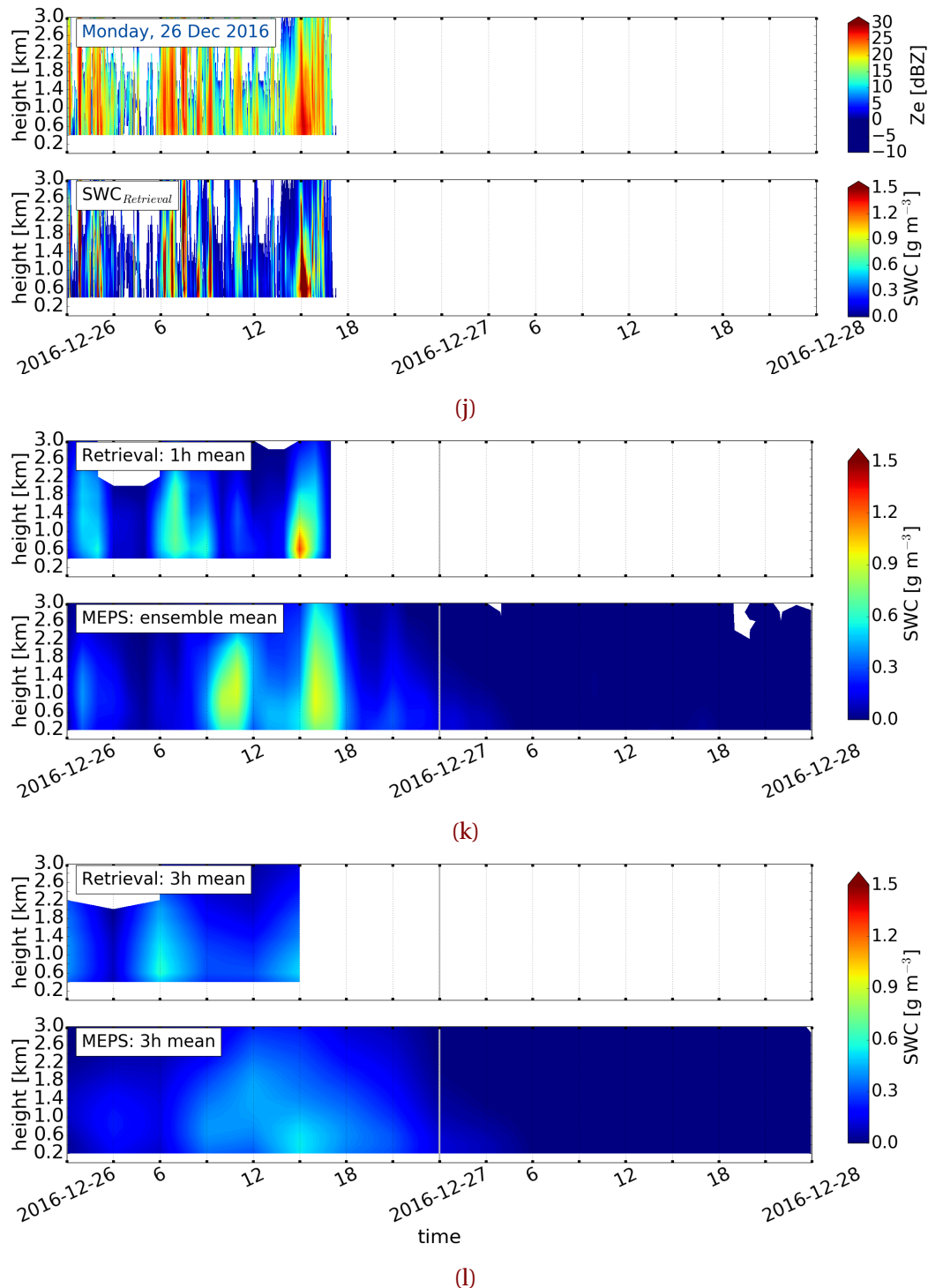


Figure 4.5.2: (Continued from previous page.) Initialisation 25 December 2016.



**Figure 4.5.2:** (Continued from previous page.) Initialisation 26 December 2016.

It shows also on 23 December 2016 the first perturbed ensemble member does not exist and hence little snow water content is predicted for the ensemble means. A comparison with 25 December 2016 and 26 December 2016 shows the same result. Not much more snow water content is predicted when using the instantaneous values from the deterministic and first perturbed forecast (Figure B.3.1c, d).

On 26 December 2016 when the passage of the occlusion is predicted, the three-hourly instantaneous SWC (Figure 4.5.2l) as well as the average of all ensemble members (Figure 4.5.2k) predict the frontal passage. Already initialisations 39 h prior let assume that intense precipitation over a short time will occur (Figure 4.5.2h, i). The variation of all members in Figure B.4.1d and e indicate that almost all perturbed members would have predicted the precipitation around 16 UTC, but the ensemble mean weakens the result. Higher predicted values appear for deterministic forecasts than for any other ensemble member for initialisations on 25 December 2016 and 26 December 2016. This bias might have led to an overestimation at the surface on 26 December 2016, where the deterministic forecast indicates higher values than the perturbed members (Figure 4.4.1f). But in Figure B.3.1c and d is the amount of snow water content very weak. It shows better estimations for predicted snowfall amount when using either hourly or three hourly time resolution and all ten ensemble members to create the mean than forecasts for hourly averages with only the deterministic and first perturbed member. Still the instantaneous average values of all ensemble members are much weaker than the retrieved SWC.

The 25 December 2016 showed patterns of liquid precipitation (Figure 4.3.2) with warm temperatures (Figure 4.3.1d) and high reflectivity (Figure 4.5.1b) between 12 UTC to 21 UTC. High reflectivity values in Figure 4.5.1b are present around 18 UTC with layer thickness up to 1.2 km. To see if liquid precipitation was predicted, the atmospheric cloud condensed water content and rainfall amount in model levels is summed. Figure 4.5.3a and b show liquid water content for initialisations at either 24 December 2016 or 25 December 2016. Positive surface temperatures were forecasted between 12 UTC to 21 UTC (Figure 4.3.1d). Initialisations more than 24 h prior show already the occurrence of the liquid layer. Figure 4.5.3a or b show also a narrow thickness up to 800 m. In Norwegian mountainous terrain is this an important feature since precipitation change can lead to a high risk for people. The avalanche danger increases with the precipitation change especially during high wind speeds. Since MEPS forecasts the liquid layer correctly in depth and length it seems to be a good interaction between the surface model and

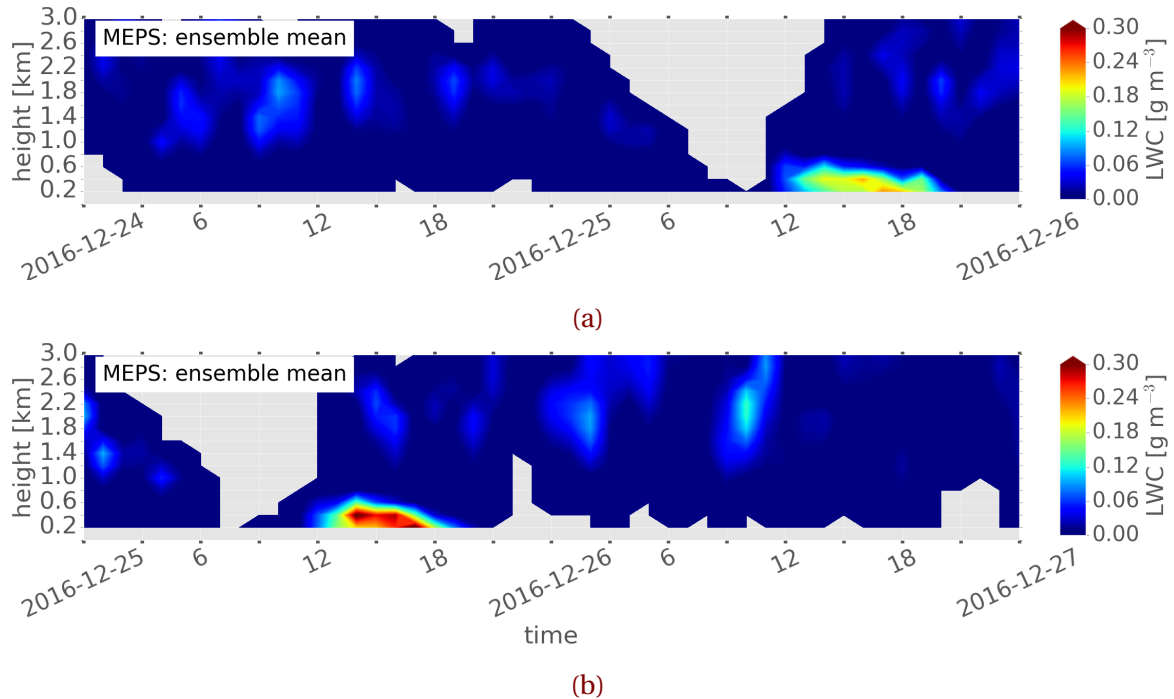


**Figure 4.5.3:** 200m hourly averaged LWC forecast from MEPS with all ensemble members, neglecting missing values. Initialised on 24 December 2016 and 25 December 2016 at 0 UTC. Liquid water content according to the colorbar.

the vertical prediction. This follows a high accuracy of the forecasting system and the advantage of using a high resolution convective scheme model.

For the first glance operates the forecast well when compared to vertical observations. One possibility is to assess the variability of all ensemble member with the coefficient of variation described in Section 2.6.4. Figures 4.5.4a to 4.5.4c show the coefficient of variation for SWC, which is the standard deviation of the ten ensemble members divided by the mean of all ensemble members. This coefficient gives the possibility to compare the SWC results for different days with different values. It follows for even a low ensemble spread of SWC (standard deviation of all ensemble members) then the different members do not need to be less variable.

The grey line in Figure 4.5.4 shows the ensemble mean of the hourly predicted SWC values. The darker the colour in Figure 4.5.4 the smaller is the variation of the SWC

**Table 4.5.1:** Interpretation of the coefficient of variation for SWC.

<b>Size of CV</b> [%]	<b>Interpretation</b> variability
0 to <25	negligible
25 to <50	low
50 to <75	moderate
75 to <100	high
100 to $\infty$	very high

relative to the mean. Initialisations on 23 December 2016 does not exist, because it had too few ensemble members (only six) to create a reasonable verification. Therefore, the initialisation on 22 December 2016 is used. The interpretation of the coefficient of variation for SWC is presented in Table 4.5.1. The CV agrees well with the prediction of the occlusion on 23 December 2016 after 15 UTC. The variability between the members is small and show a good agreement on the occurrence of snow precipitation. Figure B.4.1b and ?? show the same variability, where all ensemble member agree on the passage after 16 UTC. While comparing only six ensemble members in Figure B.4.1c, one could assume that the uncertainty of all ensemble members during the up-slope storm is low, but not as certain as for an initialisation on 22 December 2016 at 0 UTC.

A larger difference between the ensemble members is shown for the passage of the occlusion on 26 December 2016. Initialisations on 25 December 2016 present a lower variability for the passage after 15 UTC on 26 December 2016 than initialisations less than 24 h prior. Therefore, an increase of variability after shorter time and an increase in uncertainty. Again, this is not a fair comparison since hourly instantaneous values are used and there might be a time delay of half an hour about the passage which would follow it is not seen in the model forecast.

Another way to see how the MEPS forecast performed compared to the vertical observations can be done by correlating the observed SWP with the ensemble member snow water content.

One question to answer in this work is if the operational model MEPS gets large

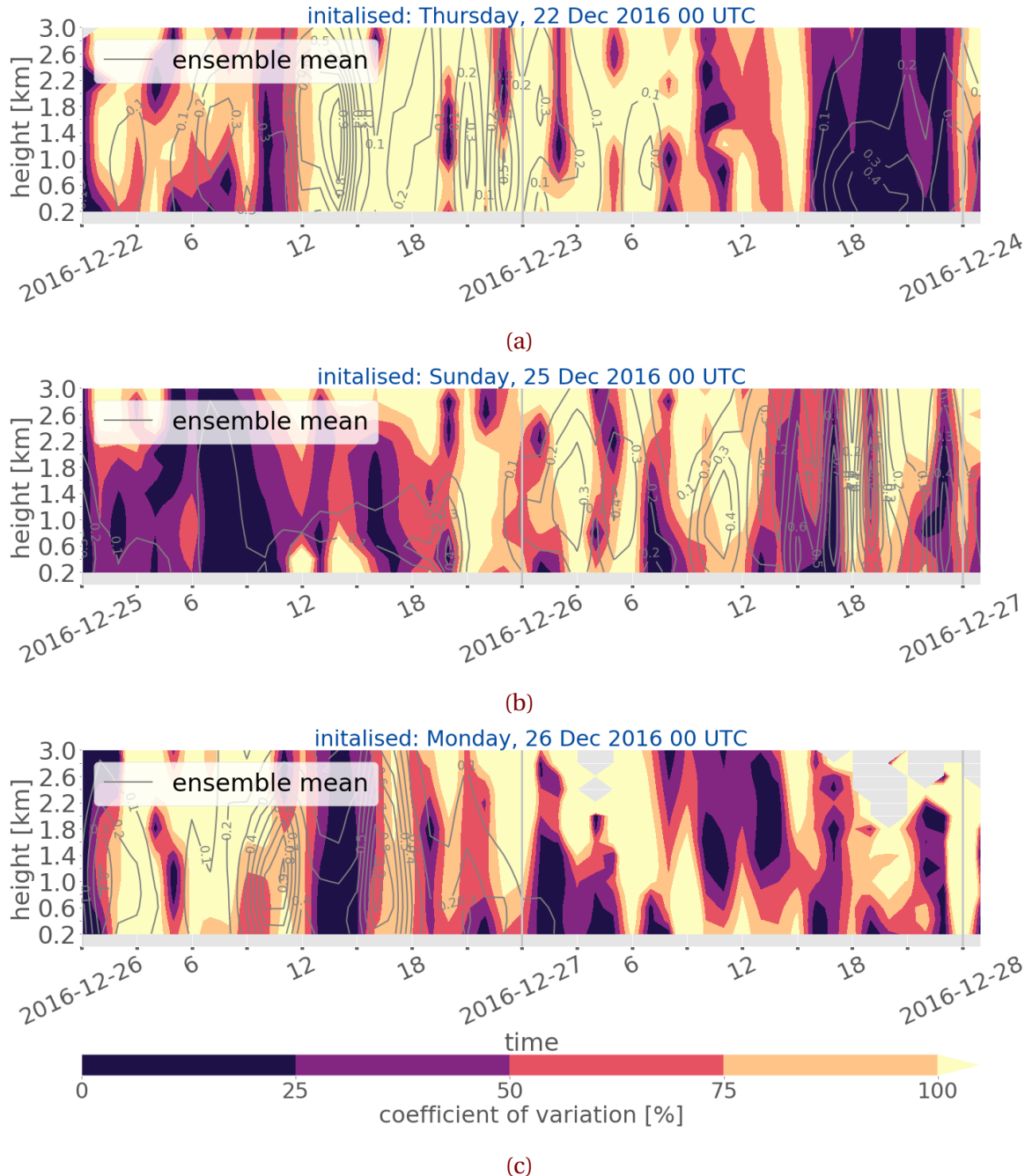


**Figure 4.5.4:** SWC variation of the ten ensemble members of MEPS. The lighter the colour according to the colourbar the higher the variation between the perturbed ensemble members. In grey the ensemble mean of all ten members.

scale features correctly. As discussed here and in Section 4.3 it seems that the model is able to cover the development of large scale features and its associated precipitation. Even with the intensification of the storm seems MEPS to be able to predict extreme events such as the Christmas event, but might have some issues predicting fast transitions of frontal boundaries.

MEPS is also able to distinguish between liquid and solid precipitation in layer thickness and duration for time resolution of one hour. This can be a major advantage since a change in temperature and associated precipitation transformation can lead to high safety issues in the Norwegian mountains, especially during winter. With the knowledge more than 24 h prior can risk notice be send out to the population and rescue teams can prepare in advance. Furthermore, roads and train tracks can be closed to increase the safety of people. *I'm not sure if the above mentioned should be here?!*

## 4.6 OROGRAPHIC INFLUENCE ON PRECIPITATION

The Haukeliseter is suspended to high wind speeds during the winter. The previous results have shown, that wind plays an important role on the precipitation. The mountain plateau is surrounded by higher mountains to the west and more open to the south east [Wolff et al., 2013, 2015], this orography seems to influence the vertical precipitation pattern. The correlation between wind speed observations and forecast have shown an overestimation of predicted wind speed throughout the event (Figure 4.3.3g and h). Müller et al. [2017] already mentioned the weakness of too strong wind prediction in AROME-MetCoOp.

On 21 December 2016 and 23 December 2016 wind directions from the south-east and south were observed, respectively. As earlier discussed in Section 4.3 and ?? was the wind change associated with the occlusion passage on 23 December 2016. The wind direction on 21 December 2016 change was also related to the large scale synoptic flow but was not associated with a frontal passage. A comparison with the large scale weather analysis from ECMWF shows, that the large scale surface wind is from the south-west at 6 UTC on 21 December 2016 (??) and has changed to west at 12 UTC (??). The observations at the Haukeliseter site show between 6 UTC to 12 UTC wind from south-east, while the predicted wind direction is from south in Figure B.1.1e. The local wind direction

influenced the precipitation pattern in the vertical in the matter that a more consistent storm structure was observed and predicted between 9 UTC to 12 UTC (Figures 4.6.1a to 4.6.1c). Both days show a more consistent storm structure with not as intense snow water content than for storm patterns from the west. Figure 2.1.1c presents the local topography around Haukeliseter and Figure 2.5.1 shows the topography resolved by MEPS. It shows that MEPS is able to cover some of the complex structure around the site, with the higher mountain to the west and the valley to the south-east. The prediction model seems to forecast the wind direction overall well, only on 21 December 2016 before 10 UTC is a south instead of a south-east wind predicted. It displays that even if the large scale wind is from the south-west is the local wind rather from the south or south-east. The orography in Figure 2.1.1c lets assume that large scale south-west wind is forced along the valley laying in south-east direction. As Figure 4.6.1b indicates is the model obviously able to cover almost the exact timing of the up-slope storm pattern. The variability of each ensemble member is again presented in Figure B.4.1a. It shows that almost all ensemble member agree on the occurrence of the storm pattern during 9 UTC to 12 UTC.

Wind from the west and therefore over mountains followed always a pulsing with more intense precipitation in the vertical (Figure 4.5.2 and ??). This effect might be related to wave breaking at the mountain and result into a pulsing precipitation pattern. More precipitation events need to be studied to understand this effect around the Haukeliseter site. MEPS seems not to cover all pulses during the course of a day, which is related to the time resolution of the forecast values. Since the prediction values exist only every hour the model might miss some of the high pulses 30 min before or after the occurrence.

One outcome of the presented study is that MEPS is able to resolve the local topography and predicts the wind direction in almost all the cases correctly. It did not cover the south-east wind direction on 21 December 2016, which must be related to the local topography. It seems more intuitive for the model to force large scale south-westerly flow into south direction. As seen in Figure 2.5.1 must the wind go along the 7.2° longitude, since a higher elevation is to the west and a 1350 m high mountain to the east. This true prediction of wind direction leads then to the correct estimation of vertical precipitation patterns. Section 4.4 describes the overestimation of surface snow accumulation during the intensification of the extreme storm. MEPS forecasted more ground accumulation than it was observed. One approach was to see, if the wind might have had an influence on the surface measurement of the double fence, which did not show to be true. A

comparison of the hourly values of MEPS, shows that neither on 24 December 2016 nor on 25 December 2016 or 26 December 2016 the vertical snow amount was higher than the observations (Figure 4.6.1e, 4.5.2h, and k). Figure B.4.1 shows very intense individual ensemble members, but no prominent sign of overestimation when the surface miscalculation was present.

During 24 December 2016 to 26 December 2016 was the wind constantly from the west with higher wind speeds observed than during 21 December 2016 to 23 December 2016 (Figure 4.3.1e, f, m; Figure B.1.1e, f, m; Figure 4.3.1g, h, n, and Figure B.1.1g, h, n). Figure 4.3.3e and f indicate a better agreement between the forecasted and observed wind directions when precipitation overestimation occurred. During 24 December 2016 to 26 December 2016 were the observed wind speeds higher than on the previous days, and as Figure 4.3.3g and h present is the correlation between observation and forecasts lower during high wind speeds. The high wind speeds from the west followed a pulsing storm pattern with intense and less intense precipitation. The pulsing pattern is forecasted by MEPS for initialisations longer than 24 h prior. Since the model gets the wind direction correctly and the affect of local mountains it follows that there seems to be some kind of interaction issue between the vertical snow amount and the surface accumulation. Vertical instantaneous values every hour can lead to a misinterpretation of the here presented results. The ensemble variability in Figure 4.6.2a, Figure 4.5.4b, and c show that the ensemble members are divided about the existence of the exact pulsing.

While the wind direction of MEPS has a good agreement shows the wind speed larger values over all days. Although MEPS includes ten perturbed ensemble members the insufficiency of AROME-MetCoOp too high wind prediction in extreme situations is not resolved. The regional model wind prediction is still dependent on the intensity of the storm. As Müller et al. [2017] also mentioned are higher wind speeds in general better forecasted in AROME-MetCoOp than in ECMWF.

## 4.7 FUTURE WORK

**Just collecting up-coming discussion points** Of course, more storms should be investigated to find the exact correlation between the surface observations and the estimated

accumulation to see if the deviation keeps as small for different snow patterns at Haukeliseter.

Figure 4.3.1 indicates that MEPS is able to simulate larger scale phenomena which is probably related to the outer boundary conditions of ECMWF as described by Dahlgren [2013]. In general, surface parameters are predicted well, only wind speed and precipitation accumulation showed overestimation in MEPS. Wind speed forecasts are higher than observations, which is probably related to the presentation of the orography in MEPS.

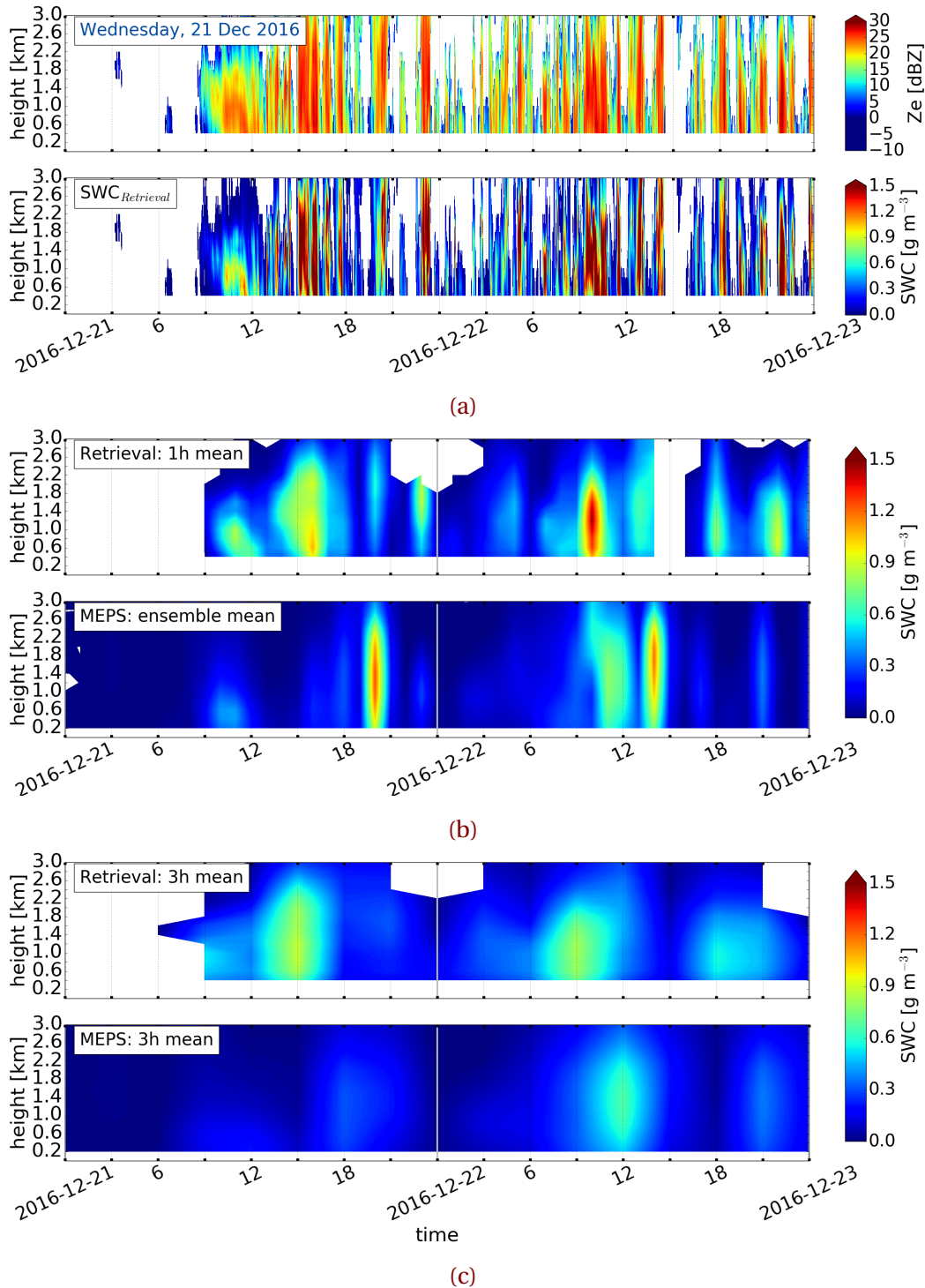


**Figure 4.6.1:** Initialisation 21 December 2016 0 UTC. (a,d) Upper panel: MRR reflectivity for 48 h, lower panel minutely retrieved SWC. (b, e) Upper panel: hourly averaged retrieved SWC, lower panel instantaneous hourly averaged forecast of all ensemble member SWC, neglecting missing values. (c, f) Upper panel three hourly averaged retrieved SWC, lower panel instantaneous three hourly averaged forecast of all ensemble member SWC.

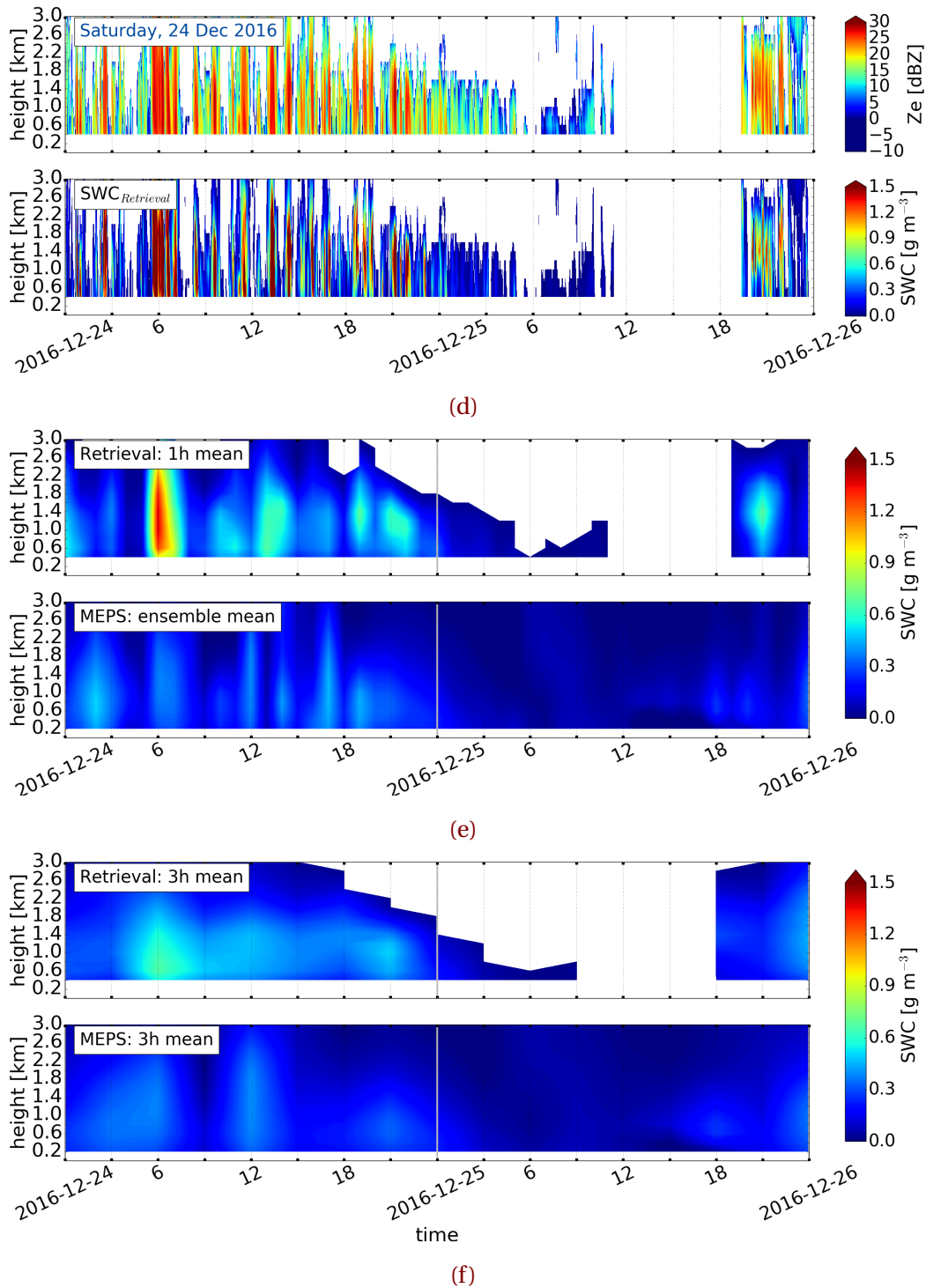
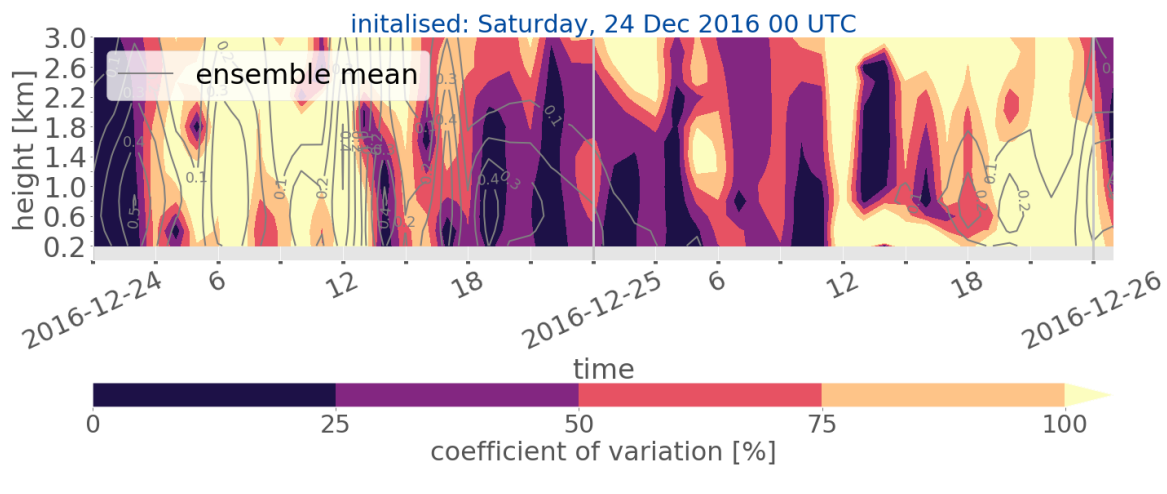


Figure 4.6.1: (Continued from previous page.) Initialisation 26 December 2016.



(a)

**Figure 4.6.2:** SWC variation of the ten ensemble members of MEPS. The lighter the colour according to the colourbar the higher the variation between the perturbed ensemble members. In grey the ensemble mean of all ten members.

## CHAPTER 5: SUMMARY AND CONCLUSION

SUMMARIZE! What did you do? Why did you do it? What did you use? What were your findings? What could be done in the future?

## REFERENCES

- Barnett, T. P., Adam, J. C., and Lettenmaier, D. P. Potential impacts of a warming climate on water availability in snow-dominated regions. *Nature*, 438(7066):303–309, November 2005. ISSN 1476-4687. doi: [10.1038/nature04141](https://doi.org/10.1038/nature04141). URL <https://www.nature.com/articles/nature04141>.
- Caniaux, G., Redelsperger, J.-L., and Lafore, J.-P. A Numerical Study of the Stratiform Region of a Fast-Moving Squall Line. Part I: General Description and Water and Heat Budgets. *J. Atmos. Sci.*, 51(14):2046–2074, July 1994. ISSN 0022-4928. doi: [10.1175/1520-0469\(1994\)051<2046:ANSOTS>2.0.CO;2](https://doi.org/10.1175/1520-0469(1994)051<2046:ANSOTS>2.0.CO;2). URL [https://journals.ametsoc.org/doi/abs/10.1175/1520-0469\(1994\)051%3C2046:ANSOTS%3E2.0.CO;2](https://journals.ametsoc.org/doi/abs/10.1175/1520-0469(1994)051%3C2046:ANSOTS%3E2.0.CO;2).
- Christensen, M. W., Behrangi, A., L'ecuyer, T. S., Wood, N. B., Lebsack, M. D., and Stephens, G. L. Arctic Observation and Reanalysis Integrated System: A New Data Product for Validation and Climate Study. *Bull. Amer. Meteor. Soc.*, 97(6):907–916, January 2016. ISSN 0003-0007. doi: [10.1175/BAMS-D-14-00273.1](https://doi.org/10.1175/BAMS-D-14-00273.1). URL <https://journals.ametsoc.org/doi/10.1175/BAMS-D-14-00273.1>.
- Colle, B. A., Garvert, M. F., Wolfe, J. B., Mass, C. F., and Woods, C. P. The 13–14 December 2001 IMPROVE-2 Event. Part III: Simulated Microphysical Budgets and Sensitivity Studies. *J. Atmos. Sci.*, 62(10):3535–3558, October 2005. ISSN 0022-4928. doi: [10.1175/JAS3552.1](https://doi.org/10.1175/JAS3552.1). URL <https://journals.ametsoc.org/doi/abs/10.1175/JAS3552.1>.
- Cooper, S. J., Wood, N. B., and L'Ecuyer, T. S. A variational technique to estimate snowfall rate from coincident radar, snowflake, and fall-speed observations. *Atmos. Meas. Tech.*, 10(7):2557–2571, July 2017. ISSN 1867-8548. doi: [10.5194/amt-10-2557-2017](https://doi.org/10.5194/amt-10-2557-2017). URL <https://www.atmos-meas-tech.net/10/2557/2017/>.

- Dahlgren, P. A Comparison Of Two Large Scale Blending Methods. page 16, 2013. URL <http://metcoop.org/memo/2013/02-2013-METCOOP-MEMO.PDF>.
- Dando, P. Introducing the octahedral reduced Gaussian grid, June 2016. URL <https://software.ecmwf.int/wiki/display/FCST/Gaussian+grids>.
- Doviak, R. J. and Zrnic, D. S. *Doppler Radar and Weather Observations*. Courier Corporation, 1993. ISBN 978-0-486-45060-5. Google-Books-ID: ispLkPX9n2UC.
- eklma. Norwegian Meteorological Institute, 2016. URL [http://sharki.oslo.dnmi.no/portal/page?\\_pageid=73,39035,73\\_39049&\\_dad=portal&\\_schema=PORTAL](http://sharki.oslo.dnmi.no/portal/page?_pageid=73,39035,73_39049&_dad=portal&_schema=PORTAL).
- Farestveit, E. 80.000 mista radioen under ekstremvêret, December 2016. URL <https://www.nrk.no/hordaland/80.000-mista-radioen-under-ekstremveret-1.13294980>.
- Field, C. B., Barros, V. R., Dokken, D. J., Mach, K. J., Mastrandrea, M. D., Bilir, T. E., Chatterjee, M., Ebi, K. L., Estrada, Y. O., Genova, R. C., Girma, B., Kissel, E. S., Levy, A. N., MacCracken, S., Mastrandrea, P. R., and White, L. L. Summary for policymakers. In: Climate Change 2014: Impacts, Adaptation, and Vulnerability. Part A: Global and Sectoral Aspects. Contribution of Working Group II to the Fifth Assessment Report of the Intergovernmental Panel on Climate Change. Cambridge: Cambridge University Press, page 34, 2014.
- Færaas, A., Rommetveit, A., Duesund, J., and Senel, E. «Urd» har nådd orkan styrke – flytter seg mot Østlandet, December 2016. URL [http://www.yr.no/artikkkel/\\_urd\\_-har-nadd-orkan-styrke--flytter-seg-mot-ostlandet-1.13292245](http://www.yr.no/artikkkel/_urd_-har-nadd-orkan-styrke--flytter-seg-mot-ostlandet-1.13292245).
- Garrett, T. J., Fallgatter, C., Shkurko, K., and Howlett, D. Fall speed measurement and high-resolution multi-angle photography of hydrometeors in free fall. *Atmos. Meas. Tech.*, 5(11):2625–2633, November 2012. ISSN 1867-8548. doi: [10.5194/amt-5-2625-2012](https://doi.org/10.5194/amt-5-2625-2012). URL <https://www.atmos-meas-tech.net/5/2625/2012/>.
- Garvert, M. F., Woods, C. P., Colle, B. A., Mass, C. F., Hobbs, P. V., Stoelinga, M. T., and Wolfe, J. B. The 13–14 December 2001 IMPROVE-2 Event. Part II: Comparisons of MM5 Model Simulations of Clouds and Precipitation with Observations. *J. Atmos.*

- Sci.*, 62(10):3520–3534, October 2005. ISSN 0022-4928. doi: 10.1175/JAS3551.1. URL <https://journals.ametsoc.org/doi/10.1175/JAS3551.1>.
- Geonor Inc. T-200b All Weather Precipitation – Rain Gauge, 2015. URL <http://geonor.com/live/products/weather-instruments/t-200b-weather-precipitation-rain-gauge/>.
- Geonorge. DTM 10 Terrengmodell (UTM33) - Kartverket - Kartkatalogen, May 2018. URL <https://kartkatalog.geonorge.no/metadata/uuid/dddbb667-1303-4ac5-8640-7ec04c0e3918>.
- Goodison, B. E., Louie, P. Y. T., and Yang, D. WMO Solid Precipitation Measurement Intercomparison: Final Report. Instruments and Observing Methods Rep. 67, WMO/TD-No. 872,. *World Meteorological Organization, Geneva, Switzerland*, page 318, 1998.
- Gowan, T. M., Steenburgh, W. J., and Schwartz, C. S. Validation of Mountain Precipitation Forecasts from the Convection-Permitting NCAR Ensemble and Operational Forecast Systems over the Western United States. *Wea. Forecasting*, 33(3):739–765, June 2018. ISSN 0882-8156, 1520-0434. doi: 10.1175/WAF-D-17-0144.1. URL <http://journals.ametsoc.org/doi/10.1175/WAF-D-17-0144.1>.
- Gunn, K. L. S. and East, T. W. R. The microwave properties of precipitation particles. *Q.J. Royal Meteorol. Soc.*, 80(346):522–545, 1954.
- Hansen, B. B., Isaksen, K., Benestad, R. E., Kohler, J., Pedersen, Ø. Ø., Loe, L. E., Coulson, S. J., Larsen, J. O., and Varpe, Ø. Warmer and wetter winters: characteristics and implications of an extreme weather event in the High Arctic. *Environ. Res. Lett.*, 9(11):114021, 2014. ISSN 1748-9326. doi: 10.1088/1748-9326/9/11/114021. URL <http://stacks.iop.org/1748-9326/9/i=11/a=114021>.
- Hansen, B. B., Aanes, R., Herfindal, I., Kohler, J., and Sæther, B.-E. Climate, icing, and wild arctic reindeer: past relationships and future prospects. *Ecology*, 92(10):1917–1923, October 2011. ISSN 1939-9170. doi: 10.1890/11-0095.1. URL <https://esajournals.onlinelibrary.wiley.com/doi/abs/10.1890/11-0095.1>.
- Homleid, M. and Tveter, F. T. Verification of operational weather prediction models september to november 2015. *METInfo Rep*, 16:2016, 2016. URL <https://www.met.no/>

- [publikasjoner/met-info/met-info-2016/\\_/attachment/download/b0463915-cba0-42ac-8539-4233ae2bf01c:3d71565a27f88085373199a33ab8569151c144e9/MET-info-22-2016.pdf](https://publikasjoner/met-info/met-info-2016/_/attachment/download/b0463915-cba0-42ac-8539-4233ae2bf01c:3d71565a27f88085373199a33ab8569151c144e9/MET-info-22-2016.pdf).
- Hudak, D., Barker, H., Rodriguez, P., and Donovan, D. The Canadian CloudSat Validation Project. *4th ERAD*, September 2006. URL <http://www.crahi.upc.edu/ERAD2006/proceedingsMask/00165.pdf>. Barcelona, Spain.
- Joos, H. and Wernli, H. Influence of microphysical processes on the potential vorticity development in a warm conveyor belt: a case-study with the limited-area model COSMO. *Q. J. Royal Meteorol. Soc.*, 138(663):407–418, January 2012. ISSN 00359009. doi: [10.1002/qj.934](https://doi.org/10.1002/qj.934). URL <http://doi.wiley.com/10.1002/qj.934>.
- Kochendorfer, J., Nitu, R., Wolff, M., Mekis, E., Rasmussen, R., Baker, B., Earle, M. E., Reverdin, A., Wong, K., Smith, C. D., Yang, D., Roulet, Y.-A., Buisan, S., Laine, T., Lee, G., Aceituno, J. L. C., Alastraú, J., Isaksen, K., Meyers, T., Braekkan, R., Landolt, S., Jachcik, A., and Poikonen, A. Analysis of single-Alter-shielded and unshielded measurements of mixed and solid precipitation from WMO-SPICE. *Hydrol. Earth Syst. Sci.*, 21(7): 3525–3542, July 2017. ISSN 1607-7938. doi: [10.5194/hess-21-3525-2017](https://doi.org/10.5194/hess-21-3525-2017). URL <https://www.hydrol-earth-syst-sci.net/21/3525/2017/>.
- Kulie, M. S. and Bennartz, R. Utilizing Spaceborne Radars to Retrieve Dry Snowfall. *J. Appl. Meteor. Climatol.*, 48(12):2564–2580, January 2009. ISSN 1558-8424. doi: [10.1175/2009JAMC2193.1](https://doi.org/10.1175/2009JAMC2193.1). URL <http://journals.ametsoc.org/doi/abs/10.1175/2009JAMC2193.1>.
- Kulie, M. S., Milani, L., Wood, N. B., Tushaus, S. A., Bennartz, R., and L’Ecuyer, T. S. A Shallow Cumuliform Snowfall Census Using Spaceborne Radar. *J. Hydrometeor.*, 17(4):1261–1279, February 2016. ISSN 1525-755X. doi: [10.1175/JHM-D-15-0123.1](https://doi.org/10.1175/JHM-D-15-0123.1). URL <https://journals.ametsoc.org/doi/abs/10.1175/JHM-D-15-0123.1>.
- Køltzow, M. A. MetCoOp EPS - A convection permitting ensemble prediction system, October 2017.
- L’Ecuyer, T. S. AOS 441 - Satellite and Radar Meteorology. January 2017. URL <https://lecuyer.aos.wisc.edu/aos441>.

- L'Ecuyer, T. S. and Stephens, G. L. An Estimation-Based Precipitation Retrieval Algorithm for Attenuating Radars. *J. Appl. Meteor.*, 41(3):272–285, January 2002. ISSN 0894-8763. doi: 10.1175/1520-0450(2002)041<0272:AEBPRA>2.0.CO;2. URL [http://journals.ametsoc.org/doi/abs/10.1175/1520-0450\(2002\)041%3C0272:AEBPRA%3E2.0.CO%3B2](http://journals.ametsoc.org/doi/abs/10.1175/1520-0450(2002)041%3C0272:AEBPRA%3E2.0.CO%3B2).
- Liu G. Deriving snow cloud characteristics from CloudSat observations. *J. Geophys. Res. Atmos.*, 113(D8), September 2008. ISSN 0148-0227. doi: 10.1029/2007JD009766. URL <https://agupubs.onlinelibrary.wiley.com/doi/abs/10.1029/2007JD009766>.
- Lorenz, E. N. Atmospheric Predictability as Revealed by Naturally Occurring Analogues. *J. Atmos. Sci.*, 26(4):636–646, July 1969. ISSN 0022-4928. doi: 10.1175/1520-0469(1969)26<636:APARBN>2.0.CO;2. URL <https://journals.ametsoc.org/doi/abs/10.1175/1520-0469%281969%2926%3C636%3AAPARBN%3E2.0.CO%3B2>.
- Markowski, P. and Richardson, Y. *Mesoscale Meteorology in Midlatitudes*. John Wiley & Sons, September 2011. ISBN 978-1-119-96667-8. Google-Books-ID: MDeYosfLLEYC.
- Martin, J. E. *Mid-Latitude Atmospheric Dynamics: A First Course*. Wiley, May 2006. ISBN 978-0-470-86466-1.
- Matrosov, S. Y. Modeling Backscatter Properties of Snowfall at Millimeter Wavelengths. *J. Atmos. Sci.*, 64(5):1727–1736, May 2007. ISSN 0022-4928. doi: 10.1175/JAS3904.1. URL <https://journals.ametsoc.org/doi/abs/10.1175/JAS3904.1>.
- McCumber, M., Tao, W.-K., Simpson, J., Penc, R., and Soong, S.-T. Comparison of Ice-Phase Microphysical Parameterization Schemes Using Numerical Simulations of Tropical Convection. *J. Appl. Meteor.*, 30(7):985–1004, July 1991. ISSN 0894-8763. doi: 10.1175/1520-0450-30.7.985. URL <https://journals.ametsoc.org/doi/abs/10.1175/1520-0450-30.7.985>.
- Meehl, G. A., Karl, T., Easterling, D. R., Changnon, S., Pielke, R., Changnon, D., Evans, J., Groisman, P. Y., Knutson, T. R., Kunkel, K. E., Mearns, L. O., Parmesan, C., Pulwarty, R., Root, T., Sylves, R. T., Whetton, P., and Zwiers, F. An Introduction to Trends in Extreme Weather and Climate Events: Observations, Socioeconomic Impacts, Terrestrial Ecological Impacts, and Model Projections. *Bull. Amer.*

- Meteor. Soc.*, 81(3):413–416, March 2000. ISSN 0003-0007. doi: 10.1175/1520-0477(2000)081<0413:AITTIE>2.3.CO;2. URL [https://journals.ametsoc.org/doi/abs/10.1175/1520-0477\(2000\)081%3C0413:AITTIE%3E2.3.CO;2](https://journals.ametsoc.org/doi/abs/10.1175/1520-0477(2000)081%3C0413:AITTIE%3E2.3.CO;2).
- MetCoOp Wiki. Description of MEPS, December 2017. URL <https://metcoop.smhi.se/dokuwiki/nwp/metcoop/>.
- METEK, M. M. G. Micro Rain Radar MRR-2, October 2010. URL <http://metek.de/wp-content/uploads/2014/05/Metek-Micro-Rain-Radar-MRR-2-Datasheet.pdf>.
- Meteo France. The Meso-NH Atmospheric Simulation System: Scientific Documentation, Part III: Physics, January 2009.
- Meteorologene. "Her kommer #Urd! Selve Lavtrykksenteret treffer Møre og Romsdal, men den sterkeste vinden kommer sør for Stad. #SørNorge" 26 December 2016, 9:34am, 2016. URL <https://twitter.com/Meteorologene>.
- Müller, M., Homleid, M., Ivarsson, K.-I., Køltzow, M. A. Ø., Lindskog, M., Midtbø, K. H., Andrae, U., Aspelien, T., Berggren, L., Bjørge, D., Dahlgren, P., Kristiansen, J., Randriamampianina, R., Ridal, M., and Vignes, O. AROME-MetCoOp: A Nordic Convective-Scale Operational Weather Prediction Model. *Wea. Forecasting*, 32 (2):609–627, January 2017. ISSN 0882-8156. doi: 10.1175/WAF-D-16-0099.1. URL <http://journals.ametsoc.org/doi/abs/10.1175/WAF-D-16-0099.1>.
- Newman, A. J., Kucera, P. A., and Bliven, L. F. Presenting the Snowflake Video Imager (SVI). *J. Atmos. Oceanic Technol.*, 26(2):167–179, February 2009. ISSN 0739-0572. doi: 10.1175/2008JTECHA1148.1. URL <https://journals.ametsoc.org/doi/abs/10.1175/2008JTECHA1148.1>.
- Noh, Y.-J., Liu, G., Seo, E.-K., Wang, J. R., and Aonashi, K. Development of a snowfall retrieval algorithm at high microwave frequencies. *J. Geophys. Res.*, 111(D22), November 2006. ISSN 2156-2202. doi: 10.1029/2005JD006826. URL <https://agupubs.onlinelibrary.wiley.com/doi/abs/10.1029/2005JD006826>.
- Norin, L., Devasthale, A., L'Ecuyer, T. S., Wood, N. B., and Smalley, M. Intercomparison of snowfall estimates derived from the CloudSat Cloud Profiling Radar and

- the ground-based weather radar network over Sweden. *Atmos. Meas. Tech.*, 8(12):5009–5021, December 2015. ISSN 1867-8548. doi: 10.5194/amt-8-5009-2015. URL <https://www.atmos-meas-tech.net/8/5009/2015/>.
- Norwegian Meteorological Institute. MET Norway Thredds Service, 2016. URL <http://thredds.met.no/thredds/catalog/meps25epsarchive/catalog.html>.
- Olsen, A.-M. and Granerød, M. Ekstremværrapport. Hendelse: Urd 26. desember met. info. no. 18/2017 ISSN X METEOROLOGI Bergen, - PDF, September 2017. URL <http://docplayer.me/48734203-Ekstremvaerrapport-hendelse-urd-26-desember-met-info-no-18-2017-issn-x-meteorologi-bergen.html>.
- Palerme, C., Kay, J. E., Genthon, C., L'Ecuyer, T., Wood, N. B., and Claud, C. How much snow falls on the Antarctic ice sheet? *The Cryosphere*, 8(4):1577–1587, August 2014. ISSN 1994-0424. doi: 10.5194/tc-8-1577-2014. URL <https://www.the-cryosphere.net/8/1577/2014/>.
- Palerme, C., Genthon, C., Claud, C., Kay, J. E., Wood, N. B., and L'Ecuyer, T. Evaluation of current and projected Antarctic precipitation in CMIP5 models. *Clim. Dyn.*, 48(1-2):225–239, January 2017. ISSN 0930-7575, 1432-0894. doi: 10.1007/s00382-016-3071-1. URL <https://link.springer.com/article/10.1007/s00382-016-3071-1>.
- Pedersen, K. and Rommetveit, A. Hva er et «ekstremvær»?, November 2013. URL [http://www.yr.no/artikkkel/hva-er-et-\\_ekstremvaer\\_\\_-1.7890946](http://www.yr.no/artikkkel/hva-er-et-_ekstremvaer__-1.7890946).
- Peel, M. C., Finlayson, B. L., and McMahon, T. A. Updated world map of the Köppen-Geiger climate classification. *Hydrology and Earth System Sciences Discussions*, 4(2):439–473, March 2007. URL <https://hal.archives-ouvertes.fr/hal-00298818>.
- Pinty, J.-P. and Jabouille, P. A mixed-phased cloud parameterization for use in a mesoscale non-hydrostatic model: Simulations of a squall line and of orographic precipitation. pages 217–220. Amer. Meteor. Soc., 1998.
- Putkonen, J. and Roe, G. Rain-on-snow events impact soil temperatures and affect ungulate survival: RAIN-ON-SNOW EVENTS IMPACT SOIL TEMPERATURES. *Geophysical Research Letters*, 30(4), February 2003. ISSN 00948276. doi: 10.1029/2002GL016326. URL <http://doi.wiley.com/10.1029/2002GL016326>.

- Rinehart, R. E. *Radar for Meteorologists: Or You, Too, Can be a Radar Meteorologist*. Rinehart Publications, 2010. ISBN 978-0-9658002-3-5. Google-Books-ID: VqatcQAACAAJ.
- Rodgers, C. D. *Inverse Methods for Atmospheric Sounding: Theory and Practice*. World Scientific, 2000. ISBN 978-981-02-2740-1. Google-Books-ID: FjxqDQAAQBAJ.
- Rutz, J. J., Steenburgh, W. J., and Ralph, F. M. Climatological Characteristics of Atmospheric Rivers and Their Inland Penetration over the Western United States. *Mon. Wea. Rev.*, 142(2):905–921, January 2014. ISSN 0027-0644. doi: 10.1175/MWR-D-13-00168.1. URL <http://journals.ametsoc.org/doi/abs/10.1175/MWR-D-13-00168.1>.
- Ruud, S., Carr Ekroll, H., Bakke Foss, A., Torgersen, H. O., and Annar Holm, P. To tonn tungt skilt blåste ned da ekstremværet traff Oslo og Østlandet i natt, December 2016. URL <https://www.aftenposten.no/article/ap-2z6wy.html>.
- Schwartz, C. S. Reproducing the September 2013 Record-Breaking Rainfall over the Colorado Front Range with High-Resolution WRF Forecasts. *Wea. Forecasting*, 29(2): 393–402, January 2014. ISSN 0882-8156. doi: 10.1175/WAF-D-13-00136.1. URL <https://journals.ametsoc.org/doi/abs/10.1175/WAF-D-13-00136.1>.
- Seneviratne, S. I., Nicholls, N., Easterling, D., Goodess, C. M., Kanae, S., Kossin, J., Luo, Y., Marengo, J., McInnes, K., Rahimi, M., Reichstein, M., Sorteberg, A., Vera, C., Zhang, X., Rusticucci, M., Semenov, V., Alexander, L. V., Allen, S., Benito, G., Cavazos, T., Clague, J., Conway, D., Della-Marta, P. M., Gerber, M., Gong, S., Goswami, B. N., Hemer, M., Huggel, C., van den Hurk, B., Kharin, V. V., Kitoh, A., Tank, A. M. K., Li, G., Mason, S., McGuire, W., van Oldenborgh, G. J., Orlowsky, B., Smith, S., Thiaw, W., Velegrakis, A., Yiou, P., Zhang, T., Zhou, T., and Zwiers, F. W. Changes in Climate Extremes and their Impacts on the Natural Physical Environment. In Field, C. B., Barros, V., Stocker, T. F., and Dahe, Q., editors, *Managing the Risks of Extreme Events and Disasters to Advance Climate Change Adaptation*, pages 109–230. Cambridge University Press, Cambridge, 2012. ISBN 978-1-139-17724-5. doi: 10.1017/CBO9781139177245.006. URL [https://www.cambridge.org/core/product/identifier/CB09781139177245A030/type/book\\_part](https://www.cambridge.org/core/product/identifier/CB09781139177245A030/type/book_part).
- Skofronick-Jackson, G. M., Kim, M.-J., Weinman, J. A., and Chang, D.-E. A physical model to determine snowfall over land by microwave radiometry. *IEEE Geosci. Remote Sens. Lett.*, 42(5):1047–1058, May 2004. ISSN 0196-2892. doi: 10.1109/TGRS.2004.825585.

- Stephens, G. L. *Remote Sensing of the Lower Atmosphere: An Introduction*. Oxford University Press, 1994. ISBN 978-0-19-508188-6. Google-Books-ID: 2FcRAQAAIAAJ.
- Stephens, G. L. and Wood, N. B. Properties of Tropical Convection Observed by Millimeter-Wave Radar Systems. *Monthly Weather Review*, 135(3):821–842, March 2007. ISSN 0027-0644, 1520-0493. doi: 10.1175/MWR3321.1. URL <http://journals.ametsoc.org/doi/abs/10.1175/MWR3321.1>.
- Stimberis, J. and Rubin, C. M. Glide avalanche response to an extreme rain-on-snow event, Snoqualmie Pass, Washington, USA. *Journal of Glaciology*, 57(203):468–474, 2011. ISSN 0022-1430, 1727-5652. doi: 10.3189/002214311796905686. URL <https://www.cambridge.org/core/journals/journal-of-glaciology/article/glide-avalanche-response-to-an-extreme-rainonsnow-event-snoqualmie-pass-washington-usa/2B6E48BD92F0700B7BEA02EF156E203F>.
- Stocker, T. F., Qin, D., Plattner, G.-K., Tignor, M. M. B., Allen, S. K., Boschung, J., Nauels, A., Xia, Y., Bex, V., and Midgley, P. M. Working Group I Contribution to the Fifth Assessment Report of the Intergovernmental Panel on Climate Change. *Cambridge: Cambridge University Press*, page 14, 2013.
- Sun, J. Convective-scale assimilation of radar data: progress and challenges. *Quarterly Journal of the Royal Meteorological Society*, 131(613):3439–3463, 2005. ISSN 1477-870X. doi: 10.1256/qj.05.149. URL <https://rmets.onlinelibrary.wiley.com/doi/abs/10.1256/qj.05.149>.
- Wolff, M. A. WMO Solid Precipitation Intercomparison Experiment (WMO-SPICE), Ch. 4.2.4 Precipitation measurements in areas with high winds and/or complex terrain. unpublished, 2018.
- Wolff, M. A., Brækkan, R., Isaksen, K., and Ruud, E. A new testsite for wind correction of precipitation measurements at a mountain plateau in southern Norway. In *Proceedings of WMO Technical Conference on Meteorological and Environmental Instruments and Methods of Observation (TECO–2010). Instruments and Observing Methods Report*, 2010.
- Wolff, M. A., Isaksen, K., Brækkan, R., Alfnes, E., Petersen-Øverleir, A., and Ruud, E. Measurements of wind-induced loss of solid precipitation: description of a Norwegian field

- study. *Hydrol. Res.*, 44(1):35–43, February 2013. ISSN 0029-1277, 2224-7955. doi: 10.2166/nh.2012.166. URL <http://hr.iwaponline.com/content/44/1/35>.
- Wolff, M. A., Isaksen, K., Petersen-Øverleir, A., Ødemark, K., Reitan, T., and Brækkan, R. Derivation of a new continuous adjustment function for correcting wind-induced loss of solid precipitation: results of a Norwegian field study. *Hydrol. Earth Syst. Sci.*, 19 (2):951–967, February 2015. ISSN 1607-7938. doi: 10.5194/hess-19-951-2015. URL <https://www.hydrol-earth-syst-sci.net/19/951/2015/>.
- Wood, N. B. *Estimation of snow microphysical properties with application to millimeter-wavelength radar retrievals for snowfall rate*. Ph.D., Colorado State University, 2011. URL [https://dspace.library.colostate.edu/bitstream/handle/10217/48170/Wood\\_colostate\\_0053A\\_10476.pdf?sequence=1&isAllowed=y](https://dspace.library.colostate.edu/bitstream/handle/10217/48170/Wood_colostate_0053A_10476.pdf?sequence=1&isAllowed=y).
- Wood, N. B., L'Ecuyer, T. S., Vane, D. G., Stephens, G. L., and Partain, P. Level 2c snow profile process description and interface control document. Technical Report, 2013. URL [http://www.cloudsat.cira.colostate.edu/sites/default/files/products/files/2C-SNOW-PROFILE\\_PDICD.P\\_R04.20130210.pdf](http://www.cloudsat.cira.colostate.edu/sites/default/files/products/files/2C-SNOW-PROFILE_PDICD.P_R04.20130210.pdf).
- Wood, N. B., L'Ecuyer, T. S., Heymsfield, A. J., Stephens, G. L., Hudak, D. R., and Rodriguez, P. Estimating snow microphysical properties using collocated multisensor observations. *J. Geophys. Res. Atmos.*, 119(14):8941–8961, July 2014. ISSN 2169-8996. doi: 10.1002/2013JD021303. URL <http://onlinelibrary.wiley.com/doi/10.1002/2013JD021303/abstract>.
- Wood, N. B., L'Ecuyer, T. S., Heymsfield, A. J., and Stephens, G. L. Microphysical Constraints on Millimeter-Wavelength Scattering Properties of Snow Particles. *J. Appl. Meteor. Climatol.*, 54(4):909–931, January 2015. ISSN 1558-8424. doi: 10.1175/JAMC-D-14-0137.1. URL <http://journals.ametsoc.org/doi/10.1175/JAMC-D-14-0137.1>.



# APPENDIX A: FORWARD MODEL

## A.1 SCATTERING MODEL

**Table A.1.1:** Branched 6-arm spatial particle with porosities, 2D, mass oriented scattering scheme at 24.0GHz.  $\mathbf{r}$ , particle size of the snow particle;  $\mathbf{m}(\mathbf{r})$ , particle mass;  $\sigma_{\text{bk}}(\mathbf{r})$  and  $\sigma_{\text{ext}}(\mathbf{r})$ , backscattering and extinction cross-section, respectively.

$\mathbf{r}$ [ $\mu\text{m}$ ]	$\mathbf{m}(\mathbf{r})$ [kg]	$\sigma_{\text{bk}}(\mathbf{r})$ [ $\text{m}^{-2}$ ]	$\sigma_{\text{ext}}(\mathbf{r})$ [ $\text{m}^{-2}$ ]
35.27	$1.68529 \times 10^{-10}$	$8.85111 \times 10^{-17}$	$4.85381 \times 10^{-17}$
41.73	$2.79128 \times 10^{-10}$	$2.00612 \times 10^{-16}$	$1.28776 \times 10^{-16}$
47.87	$4.21355 \times 10^{-10}$	$4.792 \times 10^{-16}$	$2.9959 \times 10^{-16}$
53.76	$5.96809 \times 10^{-10}$	$1.02733 \times 10^{-15}$	$6.08871 \times 10^{-16}$
59.45	$8.07074 \times 10^{-10}$	$1.68272 \times 10^{-15}$	$1.09633 \times 10^{-15}$
70.34	$1.3368 \times 10^{-9}$	$5.7444 \times 10^{-15}$	$3.61096 \times 10^{-15}$
80.69	$2.01798 \times 10^{-9}$	$1.0899 \times 10^{-14}$	$6.93961 \times 10^{-15}$
90.63	$2.85939 \times 10^{-9}$	$2.244 \times 10^{-14}$	$1.42249 \times 10^{-14}$
100.20	$3.86421 \times 10^{-9}$	$3.7814 \times 10^{-14}$	$2.73019 \times 10^{-14}$
109.50	$5.04313 \times 10^{-9}$	$7.05869 \times 10^{-14}$	$5.36211 \times 10^{-14}$
118.60	$6.40785 \times 10^{-9}$	$1.16874 \times 10^{-13}$	$9.74644 \times 10^{-14}$
127.40	$7.94266 \times 10^{-9}$	$1.67227 \times 10^{-13}$	$1.56602 \times 10^{-13}$
144.50	$1.15894 \times 10^{-8}$	$3.41952 \times 10^{-13}$	$4.19048 \times 10^{-13}$
160.90	$1.60002 \times 10^{-8}$	$7.30397 \times 10^{-13}$	$1.05187 \times 10^{-12}$

*Continued on next page*

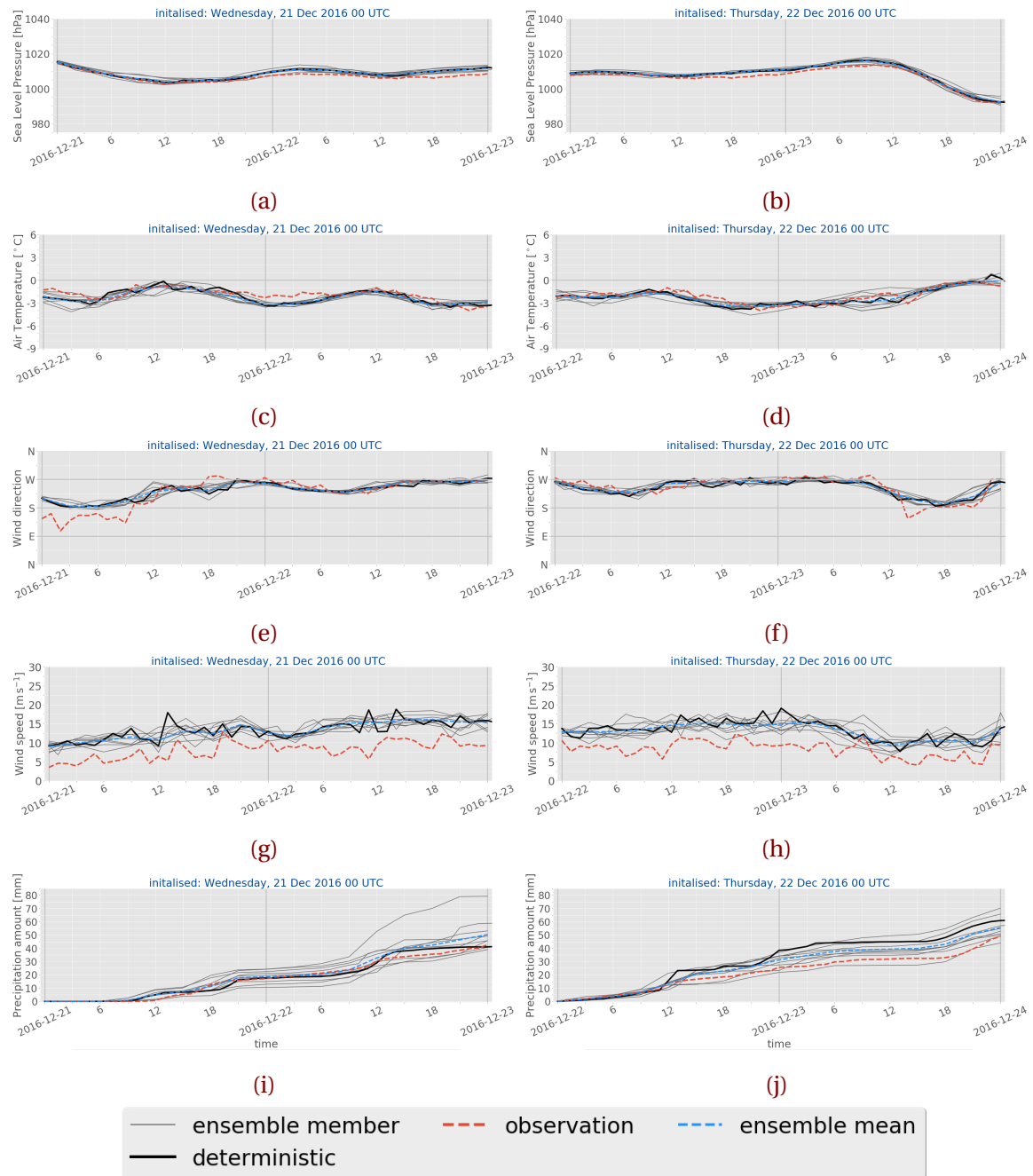
Table A.1.1 *Continued from previous page*

<b>r</b> [μm]	<b>m(r)</b> [kg]	<b>σ<sub>bk</sub>(r)</b> [m <sup>-2</sup> ]	<b>σ<sub>ext</sub>(r)</b> [m <sup>-2</sup> ]
176.80	$2.122\,78 \times 10^{-8}$	$1.136\,38 \times 10^{-12}$	$2.003\,59 \times 10^{-12}$
192.30	$2.731\,47 \times 10^{-8}$	$2.053\,33 \times 10^{-12}$	$3.635\,31 \times 10^{-12}$
236.50	$5.081\,03 \times 10^{-8}$	$5.941\,38 \times 10^{-12}$	$1.5256 \times 10^{-11}$
278.10	$8.261\,54 \times 10^{-8}$	$1.577\,15 \times 10^{-11}$	$4.319\,27 \times 10^{-11}$
317.70	$1.231\,71 \times 10^{-7}$	$3.687\,19 \times 10^{-11}$	$9.719\,16 \times 10^{-11}$
355.80	$1.730\,12 \times 10^{-7}$	$6.460\,05 \times 10^{-11}$	$1.890\,57 \times 10^{-10}$
392.60	$2.324\,39 \times 10^{-7}$	$1.291\,91 \times 10^{-10}$	$3.5246 \times 10^{-10}$
428.20	$3.015\,77 \times 10^{-7}$	$1.7526 \times 10^{-10}$	$5.673\,93 \times 10^{-10}$
463.00	$3.812\,42 \times 10^{-7}$	$3.581\,77 \times 10^{-10}$	$8.763\,74 \times 10^{-10}$
496.90	$4.712\,65 \times 10^{-7}$	$5.862\,79 \times 10^{-10}$	$1.304\,17 \times 10^{-9}$
530.10	$5.721\,78 \times 10^{-7}$	$8.501\,41 \times 10^{-10}$	$1.8862 \times 10^{-9}$
562.60	$6.840\,02 \times 10^{-7}$	$1.045\,66 \times 10^{-9}$	$2.608\,54 \times 10^{-9}$
594.50	$8.070\,74 \times 10^{-7}$	$1.545\,14 \times 10^{-9}$	$3.681\,76 \times 10^{-9}$
625.80	$9.413\,79 \times 10^{-7}$	$1.617\,04 \times 10^{-9}$	$4.485\,78 \times 10^{-9}$
656.60	$1.087\,33 \times 10^{-6}$	$2.107\,09 \times 10^{-9}$	$5.711\,84 \times 10^{-9}$
687.00	$1.245\,46 \times 10^{-6}$	$3.315\,67 \times 10^{-9}$	$7.859\,38 \times 10^{-9}$
717.00	$1.415\,84 \times 10^{-6}$	$3.735\,98 \times 10^{-9}$	$9.508\,17 \times 10^{-9}$
746.50	$1.597\,89 \times 10^{-6}$	$4.405\,91 \times 10^{-9}$	$1.148\,24 \times 10^{-8}$
775.60	$1.792\,14 \times 10^{-6}$	$5.1432 \times 10^{-9}$	$1.373\,71 \times 10^{-8}$
804.40	$1.999\,28 \times 10^{-6}$	$4.212\,61 \times 10^{-9}$	$1.596\,03 \times 10^{-8}$
832.90	$2.2194 \times 10^{-6}$	$7.0875 \times 10^{-9}$	$1.904\,38 \times 10^{-8}$
861.10	$2.452\,55 \times 10^{-6}$	$7.606 \times 10^{-9}$	$2.170\,23 \times 10^{-8}$
888.90	$2.697\,84 \times 10^{-6}$	$9.616\,05 \times 10^{-9}$	$2.524\,76 \times 10^{-8}$
916.50	$2.957\,03 \times 10^{-6}$	$1.201\,08 \times 10^{-8}$	$2.913\,29 \times 10^{-8}$
943.80	$3.229\,22 \times 10^{-6}$	$1.293\,26 \times 10^{-8}$	$3.309\,11 \times 10^{-8}$
970.80	$3.514\,37 \times 10^{-6}$	$1.532\,46 \times 10^{-8}$	$3.825\,95 \times 10^{-8}$
997.60	$3.813\,53 \times 10^{-6}$	$1.326\,87 \times 10^{-8}$	$4.344 \times 10^{-8}$



# APPENDIX B: RESULTS

## B.1 48 h SURFACE OBSERVATIONS AND MEPS FORECASTS



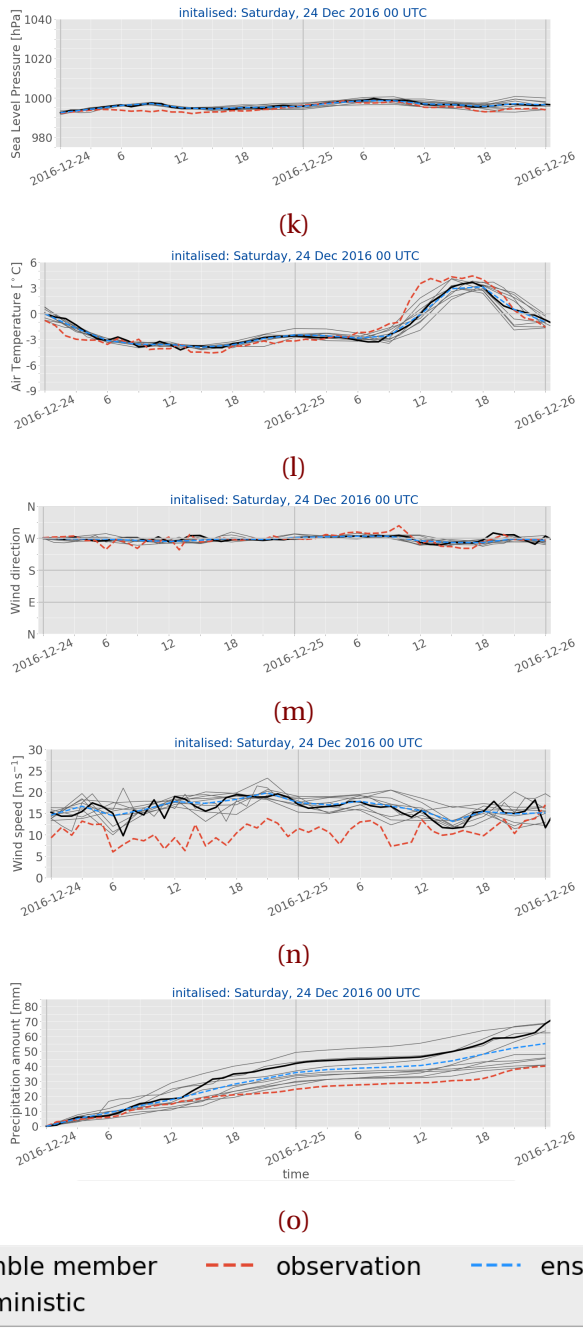


**Figure B.1.1:** (Continued from previous page.) Initialisations for 22 December 2016 (k, l, m, n, o)

## B.2 MEAN ERROR AND MEAN ABSOLUTE ERROR

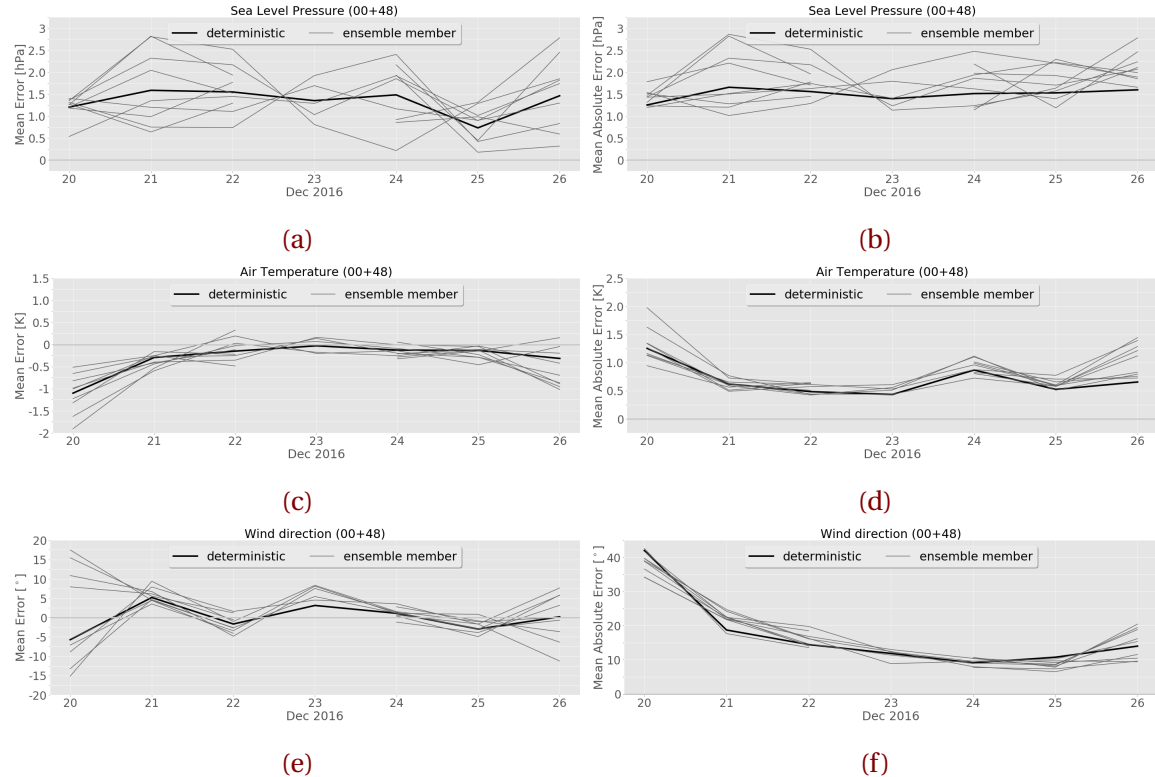


**Figure B.2.1:** Mean error (a, c, e, g, i) and mean absolute error (b, d, f, h, j) of surface variables for all ten ensemble members at Haukeliseter, initialisations at 0 UTC, valid for 48 h. From top to bottom, sea level pressure (a, b), 2 m air temperature (c, d), 10 m wind direction (e, f).

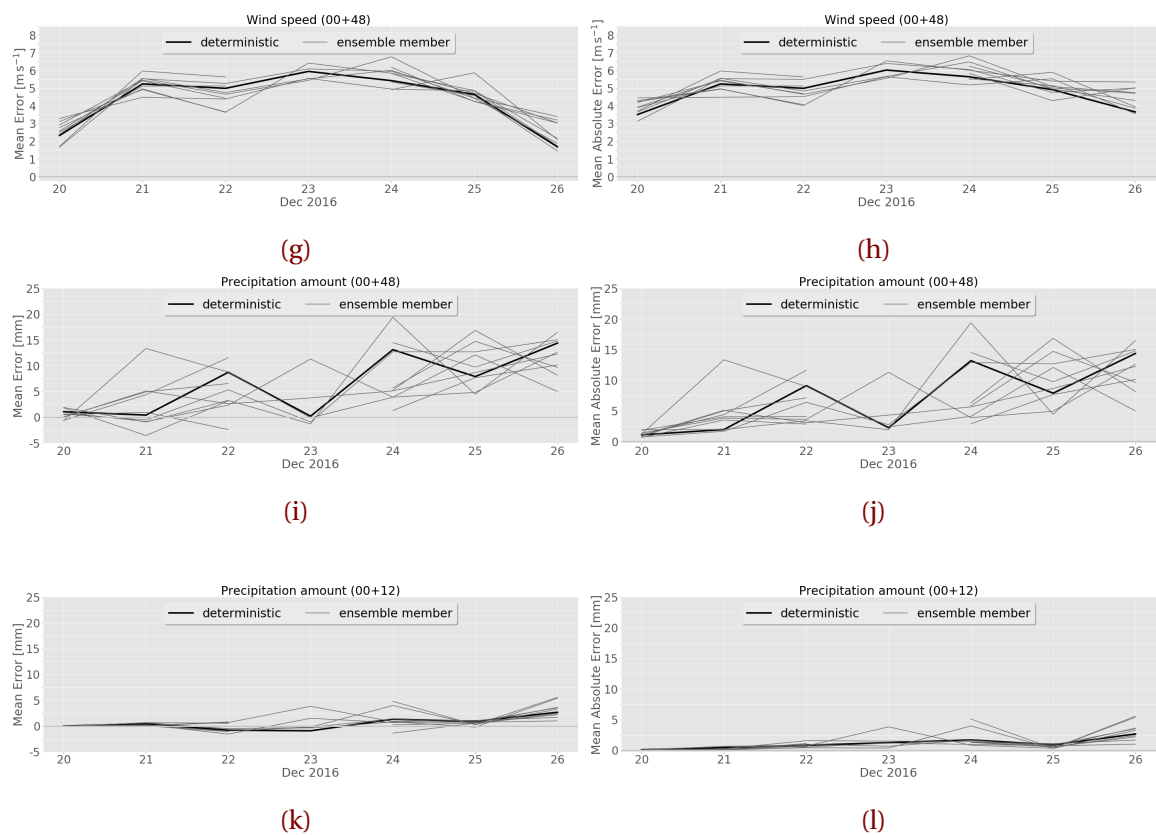


**Figure B.2.1:** (Continued from previous page.) , 10 m wind speed (g, h), precipitation accumulation for 48 h (i, j) and 12 h surface accumulation (k, l).

### B.3 HOURLY AVERAGES ENSEMBLE MEMBER ZERO AND ONE

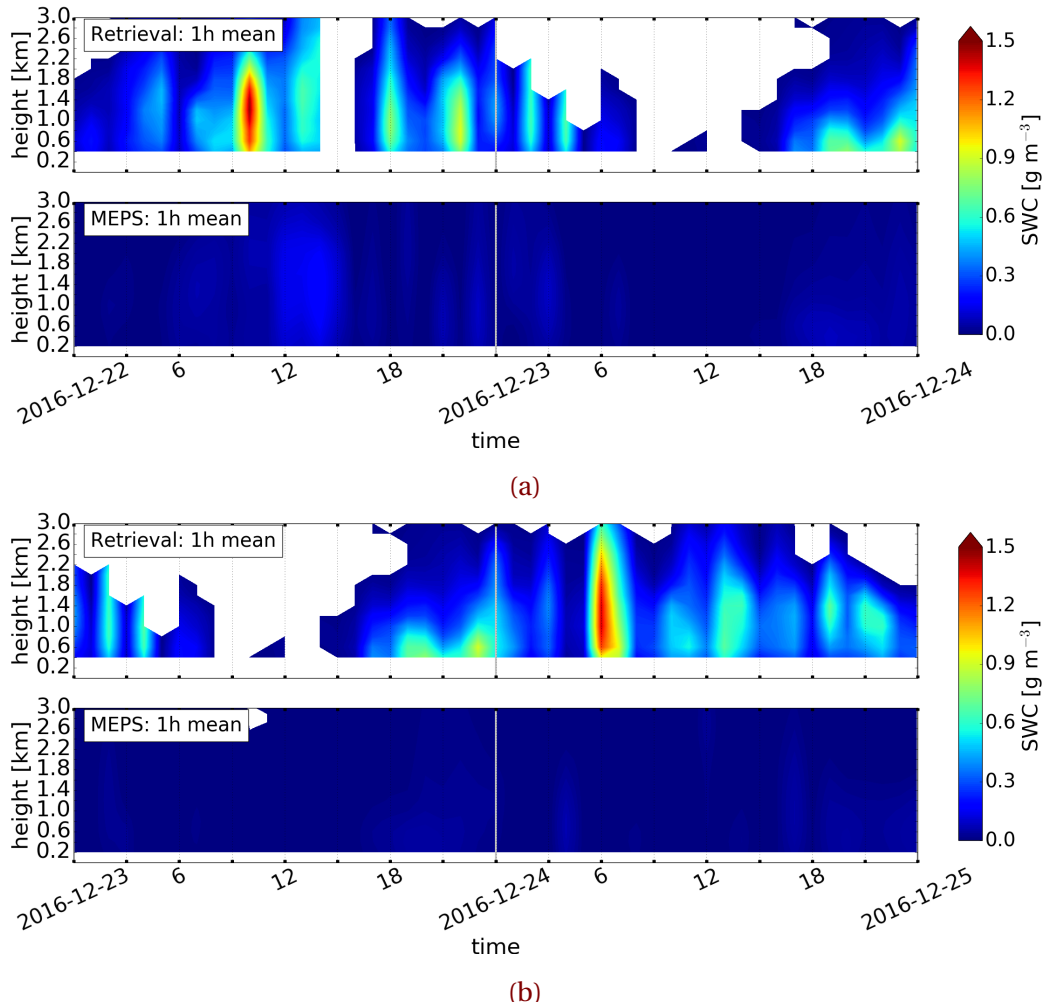
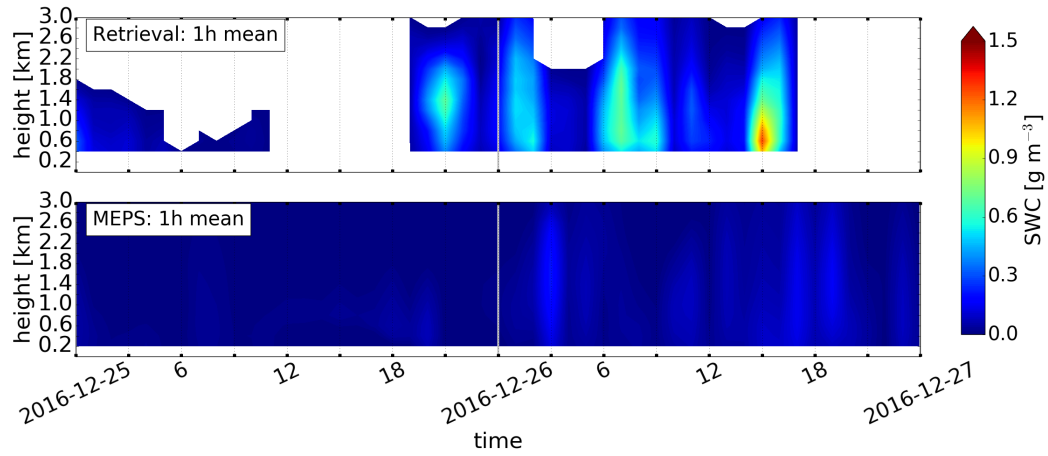
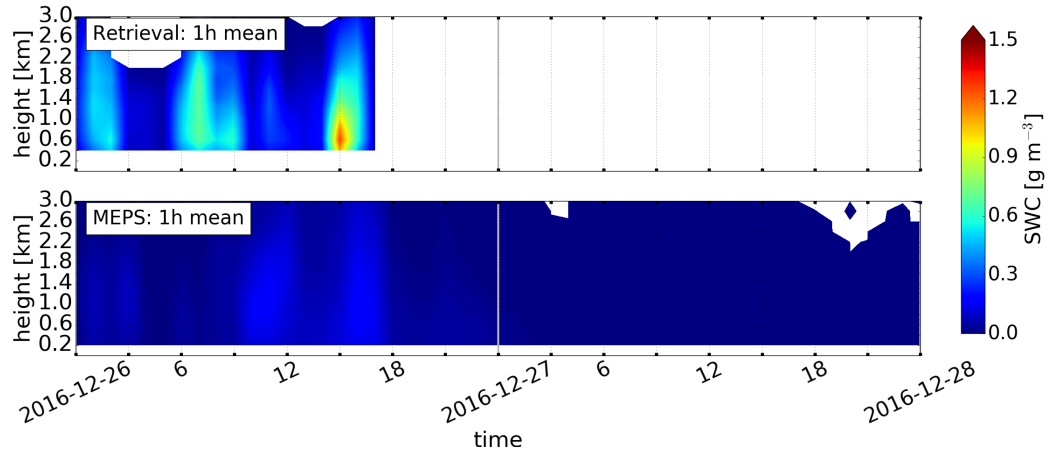


**Figure B.3.1:** Upper panel: hourly averaged retrieved SWC, lower panel instantaneous hourly averaged SWC forecast of deterministic and first ensemble member. Initialised 22 December 2016 and 23 December 2016 at 0 UTC.



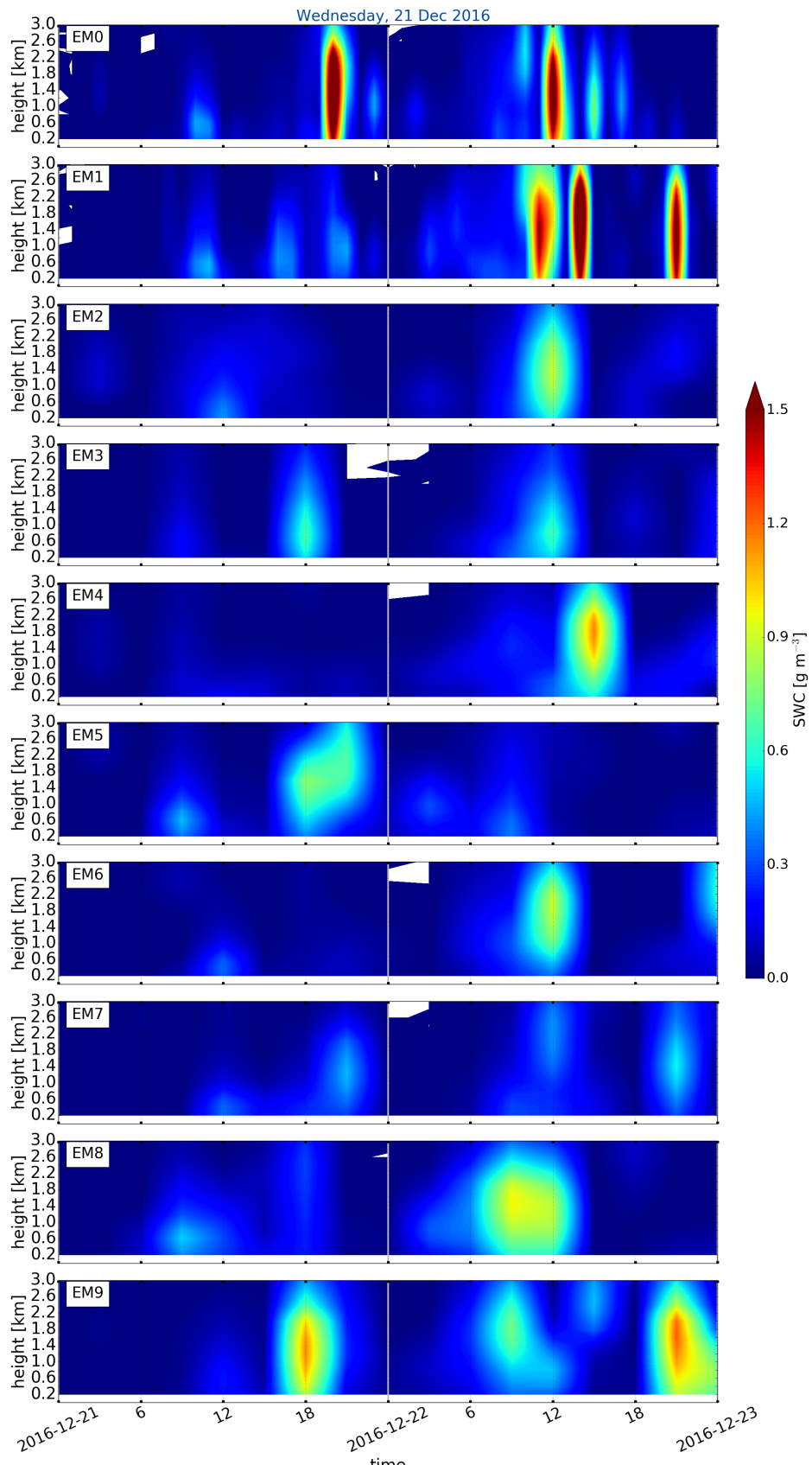
(c)



(d)

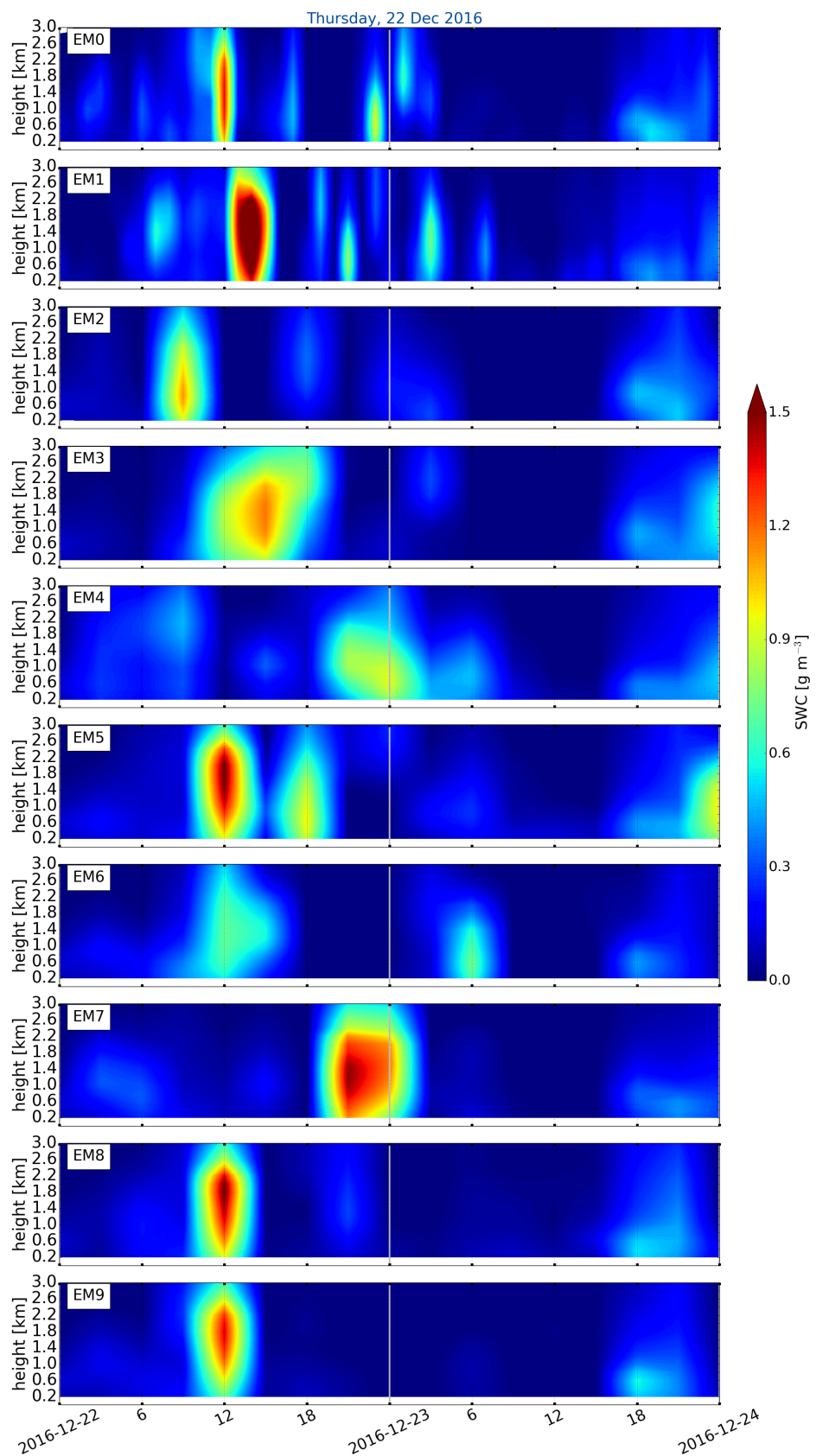
**Figure B.3.1:** (Continued from previous page.) Initialised 25 December 2016 and 26 December 2016 at 0 UTC.

#### **B.4 VERTICAL SWC - ALL ENSEMBLE MEMBER**



(a)

**Figure B.4.1:** Vertical SWC of each individual ensemble member from 0 to 9 forecast for 48 h. Initialised 21 December 2016 at 0 UTC.



(b)

**Figure B.4.1:** (Continued from previous page.) Initialised 22 December 2016 at 0 UTC.

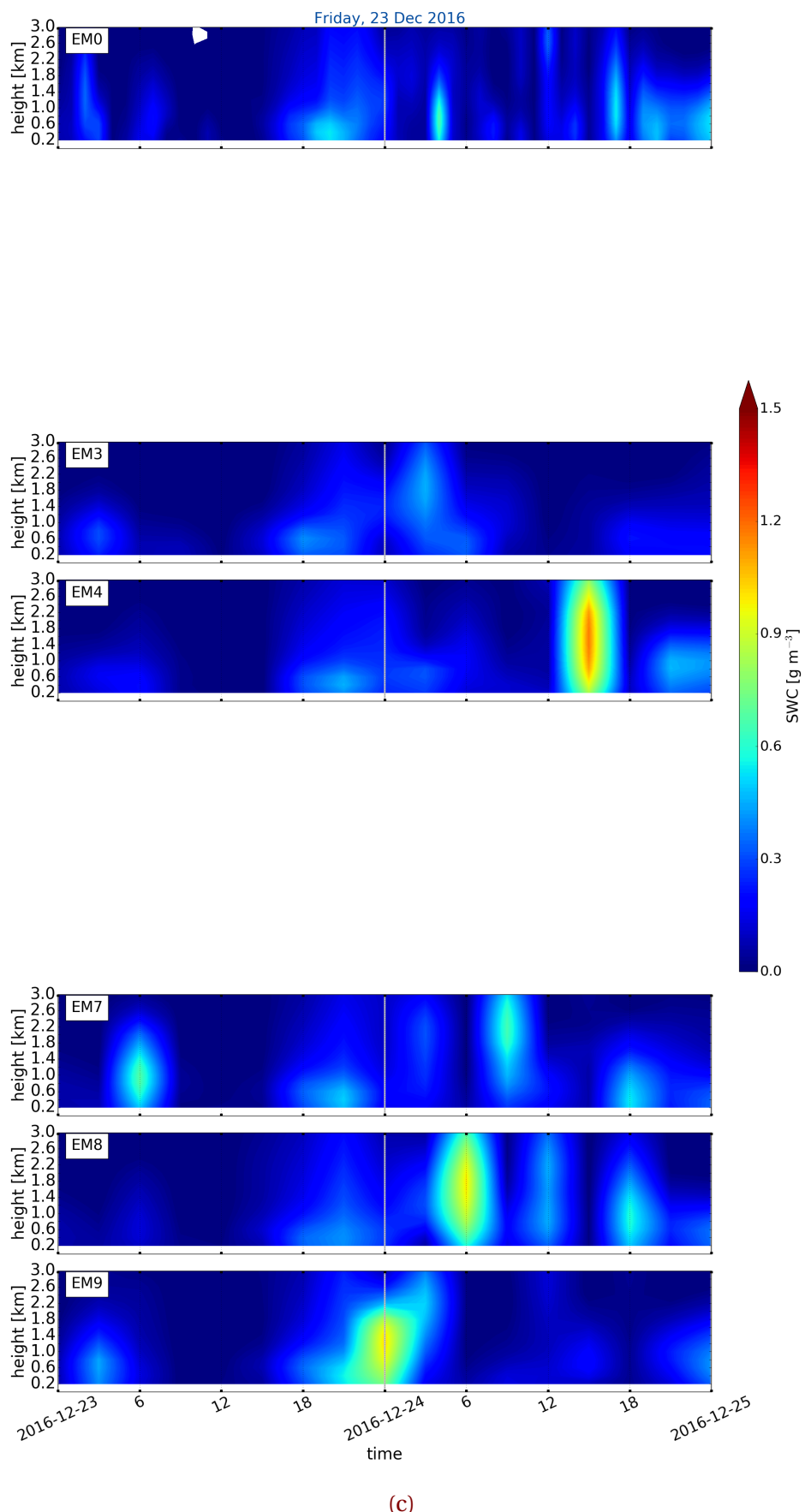
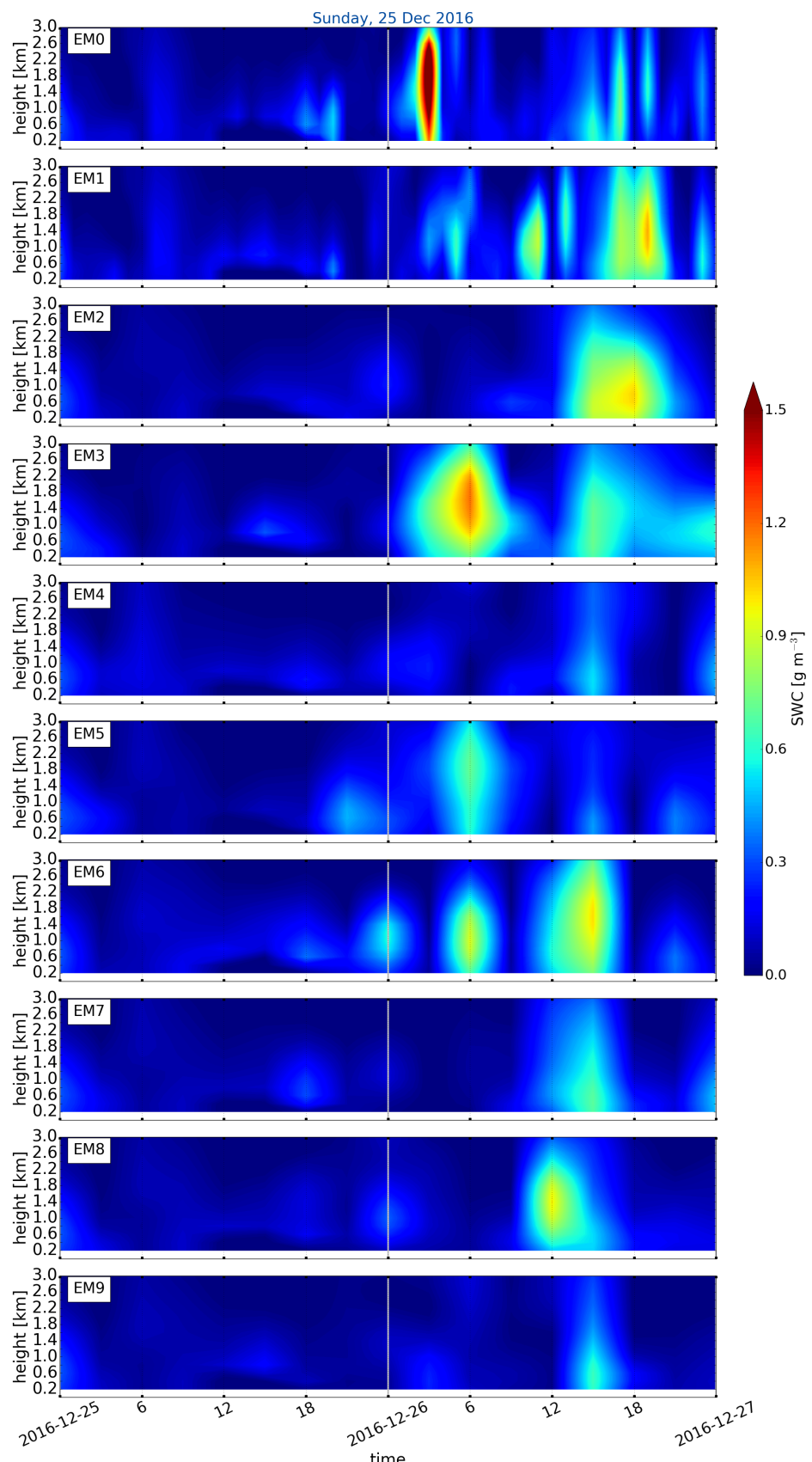
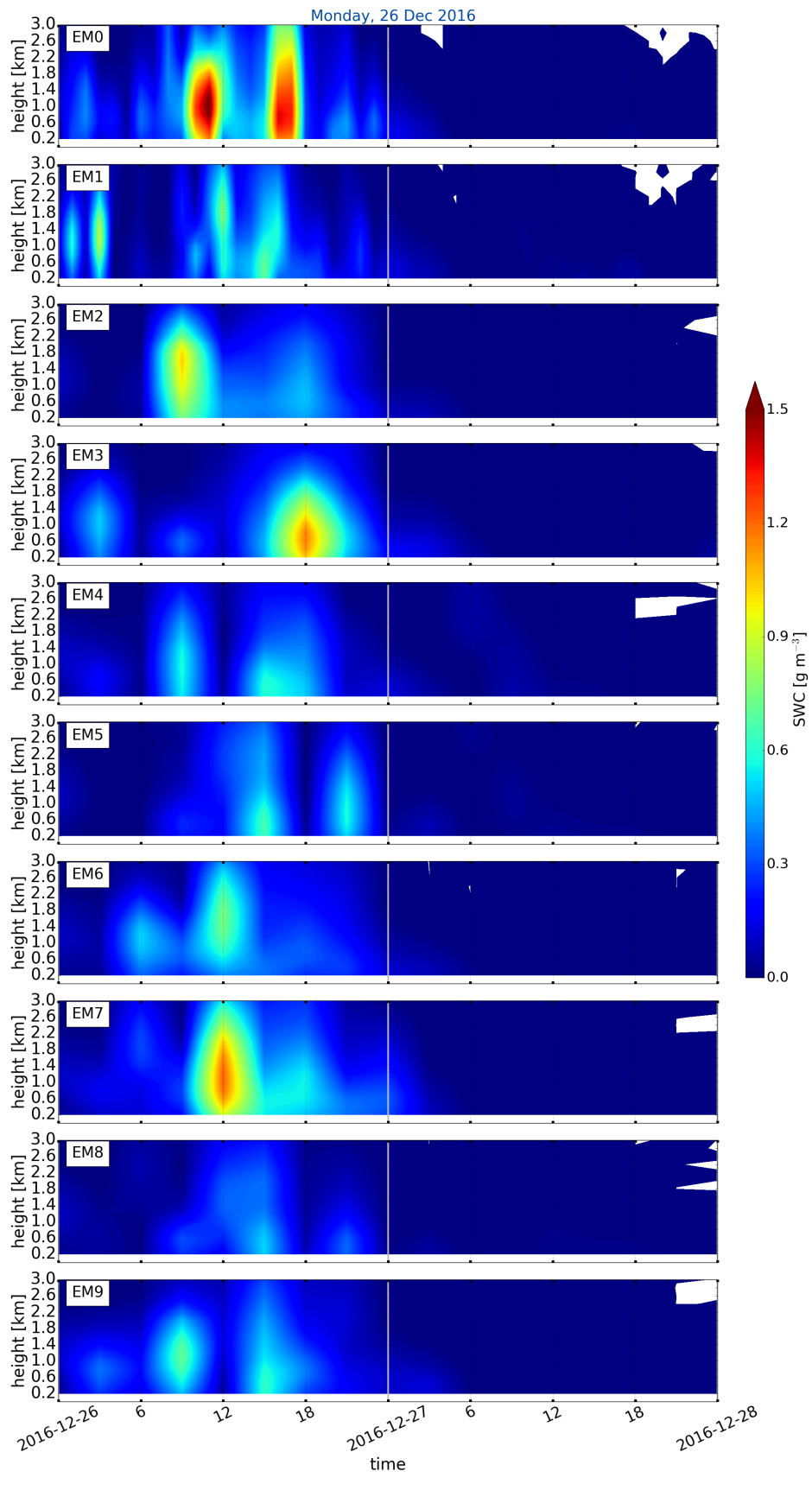


**Figure B.4.1:** (Continued from previous page.) Initialised 23 December 2016 at 0 UTC.



(d)

**Figure B.4.1:** (Continued from previous page.) Initialised 25 December 2016 at 0 UTC.



(e)

**Figure B.4.1:** (Continued from previous page.) Initialised 26 December 2016 at 0 UTC.



## DECLARATION

I hereby declare that except where specific reference is made to the work of others, the contents of this thesis is made independently. I have explicitly marked all material which has been quoted either literally or by content from the used sources.

Furthermore, I certify that this research thesis or any part of it has not been previously submitted for a degree or any other qualification at the University of Oslo or any other institution in Norway or abroad.

Franziska Hellmuth

Oslo, June 2018